Serial no.: 2008:130
ISBN: 978-82-471-8642-8 (Electronic)
ISBN: 978-82-471-8639-8 (Printed)
ISSN: 1503-8181

Davi de Miranda Fonseca

Phase separation and orientational ordering of synthetic Na-fluorohectorite clay particles in saline aqueous suspensions

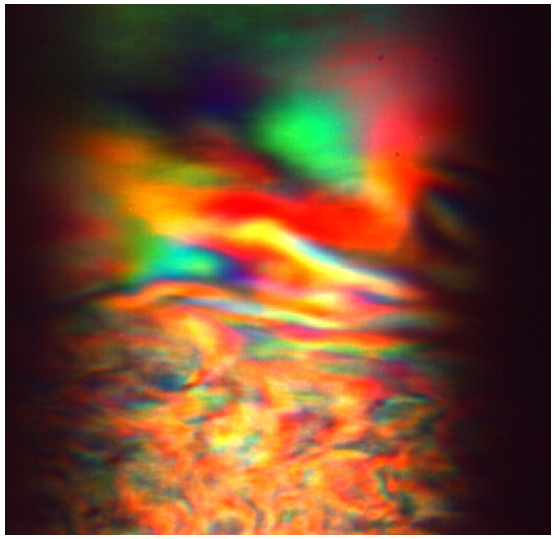

Thesis for the degree of philosophiae doctor, PhD
Trondheim, June 2008
Norwegian University of Science and Technology
Faculty of Natural Sciences and Technology
Department of Physics

NTNU
Norwegian University of Science and Technology

complex

Acknowledgements

I would like to thank my PhD supervisor Professor Jon Otto Fossum for the opportunity to work under his guidance and his many suggestions and support during this research project. I am also thankful to Dr. Yves Méheust for his help throughout the present thesis work both during his postdoctoral period at NTNU and more recently after moving to Université de Rennes 1 as an Assistant Professor.

I acknowledge the Complex research group as whole. And, in particular, Professor Arnljot Elgsæter, Professor Frode Mo, Dr. Kenneth Dahl Knudsen and Professor Knut Jørgen Måløy for the time they took to share their valuable knowledge, equipment, and laboratories.

Both PhD Ahmed Gmira and PhD Jon Are Beukes are thanked for their experimental assistance. The former regarding gathering of AFM and TEM data and the latter for collecting powder diffraction data.

I am also thankful to a number of MSc and PhD students which have been a good company during these years. In special, I must thank PhD Kanak Parmar for all the coffee and discussions and more recently MSc Zbigniew Rozynek for the same reasons. Also, it was a pleasure to meet and work with MSc students Yunus Naqvi, Lars Ramstad Alme, Nils Ivar Ringdal and Henrik Hemmen.

I am also in debt towards the technical and administrative ranks at NTNU. The secretaries of the Department of Physics are kindly acknowledged for always being in a good mood and for being extremely helpful. The Mechanical Workshop of the department cannot be forgotten, since they were always ready to help me with my designs and to professionally execute them – even with short deadlines.

I cannot forget my beloved wife for all the support and understanding. This thesis certainly consumed a lot of time that we would have spent together. I am also grateful to my parents for their patience and love.

Also, the scientific, technical and administrative staff of ESRF and LNLS and are acknowledged for their support during the synchrotron experiments.

Lastly but not least important, I am grateful for the financial grant provided jointly by the Research Council of Norway and Department of Physics of the Norwegian University of Science and Technology.

Abstract

The main goal of the present thesis is to determine and understand better the phase diagram for the nano-layered synthetic clay sodium fluorohectorite dispersed in saline aqueous solutions. This system displays up to four distinct gravity-driven phases coexisting in different strata in a single sample tube.

Visual observations were carried out at NTNU, including observations of birefringent textures when samples are placed between crossed-polarizers, and Small Angle X-ray Scattering (SAXS) experiments were performed mainly at ESRF in Grenoble, France.

The visual observations confirmed the existence of a birefringent phase and more recently the study of this phase through polarized light microscopy showed textures in the samples arising from defects in the nematic phase. These observations allow insight into the organization of the particles in the birefringent nematic phase.

The small angle x-ray scattering experiment examined tubes at different saline concentrations after settling under gravity, the results display SAXS patterns both with and without anisotropy. A method was developed to treat the data and analyze them in terms of eccentricity of the patterns that, together with the orientation of the anisotropies and the transmission data, permits the creation of the phase diagram for the system as function of electrolyte concentration and clay volume fraction.

Beyond the scope of the present work, there are still several open questions connected to these systems, to be addressed in the future.

Contents

Acknowledgements 2
Abstract 3
Contents 4
Chapter 1: Articles included in the thesis 5
Chapter 2: Scientific background 6
2.1 Ordering 6
2.2 Clays and clay minerals 8
2.3 Sample preparation 10
2.4 Visual observations 11
2.5 X-rays 12
2.5.1 SAXS 13
2.6 Phase separation and segregation in colloidal systems 16
2.6.1 Phase separation in aqueous dispersions 17
2.6.2 Isotropic–nematic transition 17
2.6.3 Glasses and/or gels 17
2.7 Introduction to the articles 18
2.7.1 Visual observations: Papers 1 and 2 18
2.7.2 Structural investigations: Papers 1, 3 and 4 19
2.7.3 Transitions by water intercalation: Papers 5 and 6 20
2.7.4 Oil dispersions under a DC electric field: Paper 7 20
Bibliography 21

Chapter 1: Articles included in the thesis

The following articles regard experimental observations of phase separation and orientational ordering of Na-fluorohectorite and are part of the present thesis. A summary of the contents of the articles as well as a description of actual contributions by the present author (DMF) in each case, is given in Section 2.7.

Paper 1
J. O. FOSSUM, E. GUDDING, D. D. M. FONSECA, Y. MEHEUST, E. DIMASI, T. GOG AND C. VENKATARAMAN
Observations of orientational ordering in aqueous suspensions of a nano-layered silicate
Energy **30**, 873–883 (2005)

Paper 2
N. I. RINGDAL, J. O. FOSSUM, D. M. FONSECA AND A. GMIRA
Birefringent Textures in the Nematic Phase of Na-Fluorohectorite Synthetic Clay
to be submitted to Langmuir beginning of May 2008

Paper 3
D. M. FONSECA, Y. MÉHEUST, J. O. FOSSUM, K. D. KNUDSEN, K. J. MÅLØY AND K. P. S. PARMAR
Phase behavior of platelet-shaped nanosilicate colloids in saline solutions — a small-angle X-ray scattering study
Journal of Applied Crystallography **40**, s292–s296 (2007)

Paper 4
D. M. FONSECA, Y. MÉHEUST, J. O. FOSSUM, K. D. KNUDSEN AND K. P. S. PARMAR
The phase diagram of polydisperse Na-Fluorohectorite–water suspensions: A synchrotron SAXS study
to be submitted to Physical Review E beginning of May 2008

Appendix: Also, I took part in experiments which investigated other aspects of Na-fluorohectorite, they are not part of my thesis but are complementary to it. Hence, they are presented as appendices:

Paper 5
Y. MÉHEUST, B. SANDNES, G. LØVOLL, K. J. MÅLØY, J. O. FOSSUM, G. J. DA SILVA, M. S. P. MUNDIM, R. DROPPA AND D. D. MIRANDA FONSECA
Using Synchrotron X-ray Scattering to Study the Diffusion of Water in a Weakly-hydrated Clay Sample
Clay Science **12**, 66–70 (2006)

Paper 6
G. LØVOLL, B. SANDNES, Y. MÉHEUST, K. J. MÅLØY, J. O. FOSSUM, G. J. DA SILVA, M. S. P. MUNDIM, R. DROPPA JR. AND D. M. FONSECA
Dynamics of water intercalation fronts in a nano-layered synthetic silicate: A synchrotron X-ray scattering study
Physica B: Condensed Matter **370**, 90–98 (2005)

Paper 7
J. O. FOSSUM, Y. MÉHEUST, K. P. S. PARMAR, K. D. KNUDSEN, K. J. MÅLØY AND D. M. FONSECA
Intercalation-enhanced electric polarization and chain formation of nano-layered particles
Europhysics Letters **74**, 438–444 (2006)

Chapter 2: Scientific background

In the present work I studied colloidal dispersions of solid nanocrystallite aggregates in saline solutions. These are created by dispersing a synthetic clay to saline aqueous solutions. These systems present a rich phase behavior, including ordered phases seen in liquid crystals. The main goal of this work is to determine the phase diagram for this system through visual and x-ray scattering experiments and also to try to understand its idiosyncrasies. In this chapter, I briefly provide the scientific background to the work in papers belonging to the thesis.

In Section 1, a basic introduction to the nematic phase is provided, including information on the director field and the order parameter. It is followed by Section 2 which regards clay minerals and provides details on the clay studied here, the synthetic fluorohectorite clay. Section 3, describes the sample preparation including the corresponding protocols to produce sodium fluorohectorite. In Section 4, the defects and textures seen in the nematic phase are introduced. Section 5 briefly discusses x-rays and describes technique of small angle x-ray scattering used in the experiments. After that Section 6 presents the basics of phase separation in colloidal systems, including the responsible mechanisms and the isotropic to nematic transition; it ends with a brief introduction to the current discussion regarding the nature of the arrested states found in colloidal systems. Finally, Section 7 summarizes the papers included in the thesis and also its appendices and describes my contribution to each paper.

In the sequence, I present summaries to the articles included in the thesis and also to those that are appendices of the thesis. Section 4 deals with the visual observations made of the system (papers 1 and 2). The papers dealing with structural investigations are described in Section 5 (papers 1, 3 and 4). Section 6 considers swelling of clays owing to water intercalation and its influence in the transport of water in dry powder clays (papers 5 and 6). Finally, Section 7 looks at the effects of an applied electric field to clay dispersed in oil from microscopy and wide angle x-ray diffraction point-of-views.

2.1 Ordering

Orientational ordering is a central theme of the present thesis, hence a very basic introduction to the subject is presented here. Liquids do not present long-range order and hence their properties are invariant with respect to direction, whereas, crystals present long-range order displaying both translational (also known as positional) and orientational order. The former means that the structure is regularly ordered, repeating pattern extending in all three spatial dimensions; whereas the latter means that the structure has a preferred direction of alignment.

In the present work we are mainly interested in two types of ordering, namely isotropic and nematic systems. Isotropic systems present no ordering, while nematic systems are characterized by orientational ordering, see Figure 1. The nematic phase is usually described by a unit vector field $\mathbf{n}(\mathbf{r})$, called the nematic director field, representing the direction of preferred orientation in the system. Another parameter is the scalar nematic order parameter field $\zeta(\mathbf{r})$ [1]

$$\zeta(\mathbf{r}) = \left\langle \frac{1}{2}\left\{3\left[\mathbf{a}(\mathbf{r})\cdot\mathbf{n}(\mathbf{r})\right]^2 - 1\right\}\right\rangle, \tag{1}$$

where $\langle\ \rangle$ denotes temporal average over thermal fluctuations and $\mathbf{a}(\mathbf{r})$ is the unit vector representing the average orientation for the elements inside a volume element at position $\mathbf{r}$. $\zeta(\mathbf{r})$ quantifies the amount of ordering in the system.

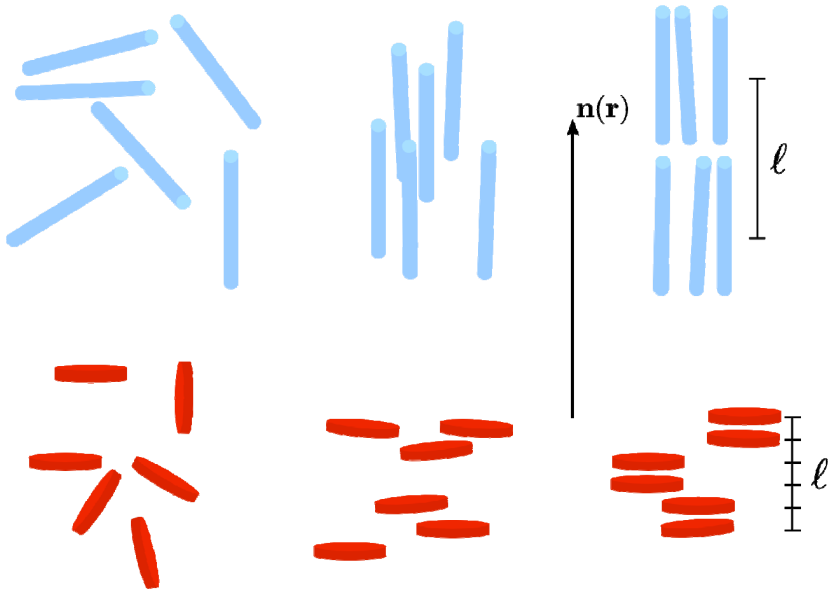

Figure 1. Left: rods and disks without order (isotropic). Center: both present orientational ordering and are aligned according to the indicated director (nematic). Right: rods and disks present both orientational order and positional in one dimension (smectic).

The $\mathbf{n}(\mathbf{r})$ vector described above represents so called uniaxial nematics [2]. In addition a biaxial nematic phase was predicted a long time ago [3] but was only confirmed to exist recently [2, 4]. This phase presents two optical axis, and hence two axis of symmetry, see Figure 2. For biaxial nematic, the local order is no longer represented by vector $\mathbf{n}(\mathbf{r})$, but is defined by a tensor order parameter $Z(\mathbf{r})$ [1, 5].

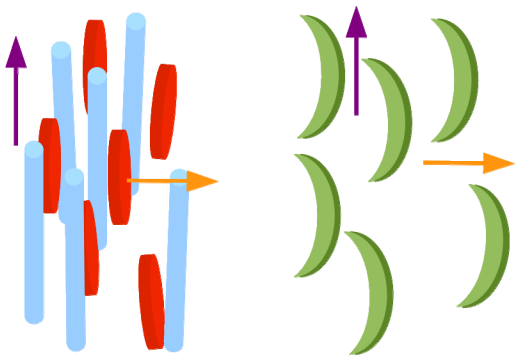

Figure 2. Biaxial nematics exemplified for two systems: set of rods and disks (left) and boomerang or banana particles (right). The two optical axes are represented by the magenta and orange arrows. In the first example, the rods are aligned along the magenta arrow whereas the disks have their normals pointing towards the orange arrow.

2.2 Clays and clay minerals

Clays are very interesting systems owing to two attributes: they are commonly available; and they possess extraordinary albeit universal properties [6]. As a result they have been used for millennia by mankind, and are extremely important in the modern world. Clays can be found [7] in ceramics, plastics, paints, paper, rubber, cosmetics, and are relevant in the oil industy [8, 9]. Not to mention its importance in geology [10, 11] and soil science [12, 13]. More recently they have been used in clay/polymer nanocomposites. In this new class of materials, nanosized inorganic filler (at least one nano-dimension) are dispersed in a polymer matrix offering tremendous improvement in thermo-mechanical properties [14, 15].

In the present thesis, the term clay is employed to denote what is usually refered as clay mineral. Hence, clay here refers to "phyllosilicate minerals and to minerals which impart plasticity to clay and which harden upon drying or firing" [16]. From this definition, clays can be synthetic, as the clay studied here. The clay studied here have observed particles of up to 20 microns hence would fail to meet some usual clay definitions in the strict sense, although most of its constituents are under 2 microns, which is important since the small particle size and high surface area of clays are partly responsible for their unique properties.

Phyllosilicates are based on tetrahedral and octahedral sheets [9, 17]. A 1:1 layer structure is formed by a tetrahedral and an octahedral sheet, for example kaolinite clay. On the other hand, a 2:1 layer is made of an octahedral sheet between two tetrahedral sheets, some examples include the smectite and vermiculite groups. Also, clays can be dioctahedral or trioctahedral, for which two thirds of the octahedral sites are occupied by cations in its unit cell or all the octahedral sites are filled with cations, respectively [18].

The isomorphic substitution by low charge cations species, primary in the octahedral sheet and to a lesser extent into the tetrahedral sheet, creates a permanent negative surface or layer charge on a clay platelet structure which is why clay particles form stacks with charge balancing cations in their interlayer space. Thus clay particles are often called nanolayered silicates. The longitudinal distance between two adjacent clay platelets in a crystalline grain is known as the basal spacing (d_{001}), a characteristic property of each type of clay mineral [9]. Also, a clay platelet always carries a small positive charge on their edges due to unsatisfied broken bonds due to finite growth of the clay platelet crystal structure. The edge charge of platelets is pH dependent in the solvent in which they are dispersed.

Clays in general are characterized by the following attributes [6]:

1) the anisotropy of the layers or particles
2) a layer structure with one dimension in the nanometer range;
3) hardening on drying or firing;
4) plasticity;
5) the ability of the surface to adsorb and ion exchange.

In the present thesis work, the focus is on the synthetic smectite fluorohectorite, which thus belongs to the smectite group, it also possesses the following properties [6]:

1) variable interlayer spacing (ambient-humidity dependant);
2) high degree of layer stacking order;
3) high specific surface area;
4) large cation exchange capacity that is little dependent on ambient pH;
5) some exchanged forms show extensive interlayer swelling in water.

As mentioned, this thesis regards the synthetic clay fluorohectorite (NaFHT). Since its interlayer material is composed of hydrated exchangeable cations and owing to the value of its net layer charge per formula unit (–0.6 e per Si_4O_{10}), it is classified as a 2:1 smectite [6], its layers stack together and these stackings can swell in the presence of water, i.e. water molecules may enter the interlayer space increasing the distance between layers [19], Figure 3 depicts this structure. The basic particle that we will be discussing in the present paper, are these stacked layers including sharing counter-ions, which we will call particle or platelet.

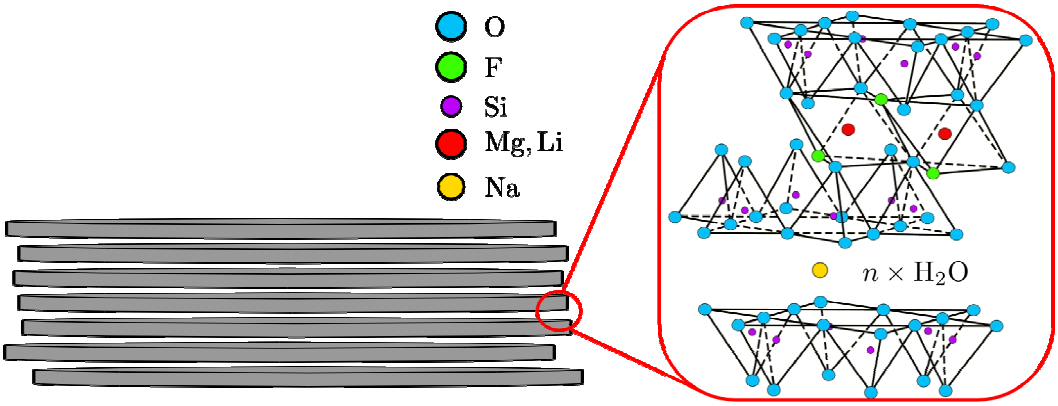

Figure 3. Stacked clay platelets, the detail shows part of the 2:1 structure of NaFHT and the interlayer spacing before the tetrahedral sheet of the next layer.

NaFHT has the composition $Na_{0.6}Mg_{2.4}Li_{0.6}Si_4O_{10}F_2$ [6], where Na^+ is the counter-ion in the interlayer space and can be hydrated and the layer charge originates from the substitution of octahedral Mg^{2+} by Li^+. It presents a high polydispersity in particle size and aspect ratio [18], the platelets of NaFHT display lengths varying from around 100 nm to 20 microns, and the observed thickness is in the 20–100 nm range [20]. Figure 4 shows an electron micrograph of a NaFHT particle.

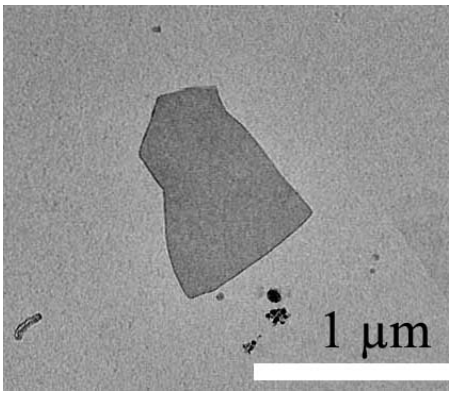

Figure 4. Transmission electron micrograph of a NaFHT platelet.

NaFHT-NaCl-H_2O systems exhibit several coexisting phases (or strata) which have been studied by x-ray diffraction [20] identifying three different phases characterized by differences in orientational order and/or size of the domains. Visual observations including the use of crossed-polarizers [21] corroborated this since a birefringent region was found coinciding with the oriented one and the textures present in the nematic phase brought insight on the organization of the particles there.

2.3 Sample preparation

Before actual sample preparation the NaFHT powder must be made, one can purchase NaFHT directly from Corning , Inc. (New York – USA); however our recent experience is that they cannot prepare base material with the same properties independent of batch (for instance, swelling in the presence of water may vary from batch to batch). However it turns out that Lithium Fluorohectorite (LiFHT) from Corning Inc. is "better behaved." Thus we cation-exchanged LiFHT to obtain NaFHT. The LiFHT has a composition by weight of 60.3% SiO, 20.2% MgO, and 19.5% LiF. In order to produce NaFHT powder, the following protocol was employed:

- Pour 1000 ml of destilled/deionized water into a 2 liters polypropylene Erlenmeyer;
- Add 70 g of LiFHT;
- Shake it at 300 rpm for two days in a New Brunswick Scientific Series 25 Incubator Shaker;
- Add 60 g of NaCl;
- Shake at 300 rpm for 2 weeks;
- Dialysis to remove the extra Cl^- and Na^+ using Spectrum Laboratories Ø20.4 mm Spectra/Pro 4 membrane tubing at ambient temperature with moderate stirring employing floating magnetic stirrers;
- Check the solution for the Cl^- contents using the silver nitrate test (add AgNO3 and check for white precipitates). Before testing the pH must be reduced to a value below 7 using sulfuric acid in order to avoid formation of silver hydroxide (brown color), and centrifuge the tube at 4000 rpm using the Jouan B4i centrifuge before trying to observe the AgCl precipitates;
- Dry at 105 degrees Celsius protecting the contents with a glass cover in the Memmert Model 700 oven. It takes around 3 days;
- Use a mortar and pestle to prepare it to be milled;
- Pulverize it using a milling machine (IKA A11), fill no more than 2/3 of the cup. Use it for 15 seconds, and then allow it to rest for 5 minutes, after that mill for more 15 seconds, and finally wait 15 minutes before opening it in order to transfer the powder to a container.

The preparation of the NaFHT-NaCl-H_2O samples also follows a protocol:

- Two liters of 1 M NaCl saline solution is prepared;
- One liter of the saline solutions at intended concentrations are prepared by successive dilution;
- 50 ml from each NaCl solution are poured into different capped-tubes and their weight is measured;
- From the weight of the solution and the target clay mass percentage, the weight of clay is calculated;
- The intended clay amounts are measured and are exact up to the first mg decimal place;
- The clay is added to the capped-tubes and they are further sealed with Parafilm;
- They are left shaking overnight (at least twelve hours) at 1100 rpm in a Heidolph Instruments Vibramax 100;
- The desired volumes are transferred into the containers to be used in the experiment. Before pouring them into the container, the tubes are always vigorously manually shaken to avoid differences owing to sedimentation;
- The container is sealed and left to settle under gravity for at least thirty days.

Owing to the reported effects of pH in the clay dispersions [22], samples were prepared using aqueous solution of sodium hydroxide at pH 11 and compared against samples that were prepared in distilled water. The results showed no difference, hence all samples used in the present thesis were created using distilled water.

Tests during the preparation of the clay dispersions showed that the order in which the components (NaFHT, H_2O and NaCl) were added does not matter.

2.4 Visual observations

Birefringence in clay suspensions were observed as early as 1938 by Langmuir [23]. Birefringence is a distinguished optical property of phases presenting nematic ordering. It happens when there is at least one optical axis, i.e. more than one refractive index [24]. Hence, a birefringent sample will appear bright when placed between crossed-polarizers, whereas, an isotropic sample under the same conditions will appear dark. Since, the NaFHT-NaCl-H_2O systems studied here can present isotropic and nematic phases coexisting in the same sample tube at different strata, placing them between crossed-polarizers is a straightforward way to discriminate strata.

Furthermore, nematic systems can present defects and textures [1]. Among observed textures are Schlieren patterns and disclinations. They may appear as singular dark points connected by black stripes, related to regions with optical axis aligned with one of the polarizers. These defects are classified using a topological theory [25-27].

Disclinations happen when the orientation of the optic axis varies from point to point [1], hence it occurs when there are points of discontinuity in the orientation, i.e. in the director field $\mathbf{n}(\mathbf{r})$. The discontinuity may be located at a single point or along a line, and is referred to as a point or line disclination, respectively. Another type is the sheet disclination, which happens for discontinuities located on a surface. The study of these defects through polarized light microscopy can provide valuable information regarding the liquid-crystalline character of the nematic phase [28].

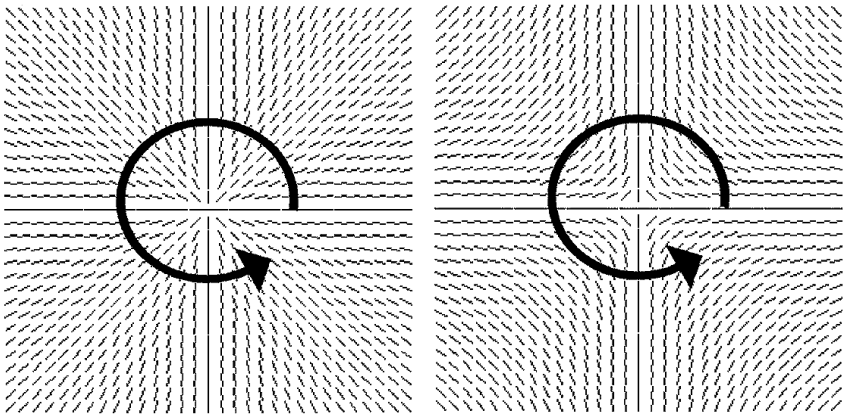

Figure 5. Examples of defects, at its center there is a singularity and in order to quantify it it is necessary to analyze the directors around it. This is done by counting how many turns the director makes around the counter-clockwise direction. Left: winding number +1; Right: winding number –1.

The analysis of the defects is done through introduction of the winding number m [26]. Since the defect represents a singularity, in order to define it one counts how many times the director field completes a full rotation around the defect along a counter-clockwise direction, this value is defined as *m*; Figure 5 exemplifies defects with winding number +1 and –1, the interaction of these two defects would lead to a cancelation of the defect. It is important to

note that point defects are characterized by integer winding numbers and that for line defects half-integer values are also allowed owing to the head-to-tail invariance.

The visual observation experiments consisted in preparing a number of samples at different clay and sodium chloride concentrations, and then taking pictures of them between cross-polarizers and under non-polarized white illumination. Lastly, polarized light microscopy was used to study the nematic phase. Two kinds of rectangular sample tubes were mainly used in these experiments of the suspensions: Vitrotube 4410-100 from VitroCom, a 10×1×0.1 cm glass sample tube; and a 5×1×0.1 cm cell made of polyoxymethylene plastic with glass walls glued to it. Also, thin-walled capillary tubes with diameters of 1 and 2 mm were used in some of the studies. The acquisition of the pictures was controlled by a computer which was also used as storage for the images.

2.5 X-rays

X-rays are part of the electromagnetic spectrum, like visible light, and are characterized by their short wavelength, situated between ultraviolet and gamma-rays. Since their discovery by Röntgen in 1895 they have become an invaluable probe to the structure of matter [29].

X-ray display properties of both waves and particles. For instance, the energy of an x-ray beam interacting with matter is partially transmitted, partly scattered, and part of it is absorbed. The periodic structures in a crystal structure could serve as a diffraction grating. In that case the relationship among wavelength λ, the angle between the incident beam and parallel planes of atoms causing diffraction, and the spacing between these planes is given by Bragg's law [30]

$$2d_{\mathrm{hkl}} \sin\theta = n\lambda, \tag{2}$$

where d_{hkl} is the spacing between any two [hkl] planes of the crystal, the scattering angle is 2θ and n is an integer determined by the order given (see Figure 6). Bragg's law states that the interference of the waves is constructive when the phase shift is a multiple of 2π.

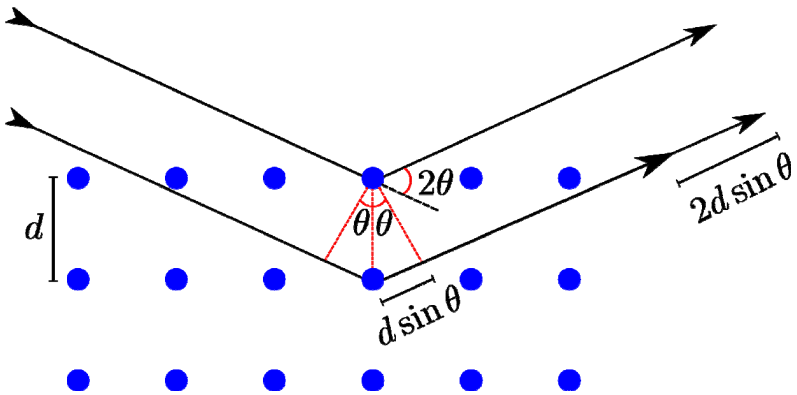

Figure 6. Bragg's law: constructive interference occurs when the difference in travelled paths equals an integer number of the wavelength.

Therefore Bragg's law of x-ray diffraction [17, 31, 32] provides information about the crystalline nature (periodic arrangement of atoms or ions) and amorphous or disordered nature (non-periodic arrangement of atoms or ions) of materials.

X-ray diffraction is the most important tool for qualitative (individual clay minerals) and quantitative (mixed clay minerals) analysis of clays, due to the unique chemical composition of phyllosilicates the qualitative analysis can be quickly done by checking the position of the Bragg peaks, i.e. [hkl] reflections [9, 17, 31]. Also, the mixture of several clay minerals can easily have a qualitative identification done since the reflections of mixed-layer clay minerals are usually found between those of the pure clays. A quantitative analysis, on the other hand, would check the location and intensity of the reflections, since these can reveal the ratio of the components [17, 31], requiring good sample preparation [17, 33].

Another important application of x-ray diffraction regards expanding clay minerals like smectites, through measurements in the shift in the Bragg peaks under dry/humid environment one can identify the presence of integer number of water layers in the interlayer [19, 34, 35] and also the random intercalation of water layers [36]. Further applications of x-rays include the use of the position of Bragg peaks 030 and 060 to distinguish di-octahedral from tri-octahedral structures [17].

2.5.1 SAXS

In the present work we are mainly interested in structures larger than the spacings of a crystal and for that purpose we employ small angle x-ray scattering (SAXS). The quantities that we will be discussing are the scattered intensity and the scattering vector. The scattering vector is defined as $\mathbf{q} = \mathbf{k} - \mathbf{k_0}$, where $\mathbf{k_0}$ is the incoming wave and $\mathbf{k}$ the outgoing one, and is given by [37, 38]

$$q = |\mathbf{q}| = \frac{4\pi}{\lambda} \sin\theta, \tag{3}$$

where the scattering angle is 2θ and λ is the wavelength of the radiation ($\lambda = 2\pi / k$). The total amplitude at $\mathbf{q}$ is the sum of all waves scattered by the atoms in the illuminated sample, denoted here as scattered intensity, I(q).

In general, the scattered intensity in SAXS experiments is controlled by the size and shape of nanoscale structures, their tendency to aggregate, the porosity of correlated aggregated nanoscale structures, the magnitude of their specific surface area, and more generally by the inhomogeneities characterizing the nanoscale structures of the systems [37-46] Hence, SAXS probes structural information about inhomogeneities in materials [47], with a characteristic length on the order of nanometers to micrometers. From equation 2.2 we note that this is possible at low scattered angle, or long wavelengths (visible light), hence the name of the technique. SAXS is among the analytical techniques most widely employed to study mesoscopic materials [40, 43, 45] (along with optical and electron microscopy, other x-ray and neutron methods, NMR and IR spectroscopy).

Because the probed distances are large when compared to interatomic distances, the medium is treated as a continuum characterized by its average density. Assuming that we have particles embedded in this continuum, the scattering intensity, I(q), contains information on the organization (interaction) between the particles and on the size and shape of the particles, Figure 7 exemplifies this.

The total scattered amplitude at $\mathbf{q}$ is the sum of the waves scattered by all atoms in the irradiated sample. Since the distances are large compared to interatomic distances, it is not possible to discriminate the contributions from the individual atoms to the scattering and instead of a sum over discrete atoms we deal with an integral involving the an average

electron density, $\rho(\mathbf{r})$, of the sample. Then, the scattered amplitude is recognized as the Fourier transform of this density

$$A(\mathbf{q}) = \iiint \rho(\mathbf{r}) e^{-i\mathbf{q}\cdot\mathbf{r}} d\mathbf{r}, \tag{4}$$

and the scattered intensity is given by

$$I(\mathbf{q}) = |A(\mathbf{q})|^2 = V \iiint p(\mathbf{r}) e^{-i\mathbf{q}\cdot\mathbf{r}} d\mathbf{r}, \tag{5}$$

where

$$p(\mathbf{r}) = \frac{1}{V} \iiint \rho(\mathbf{r}_0)\rho(\mathbf{r}_0 + \mathbf{r}) d\mathbf{r}_0 = \langle \rho(\mathbf{r}_0)\rho(\mathbf{r}_0 + \mathbf{r}) \rangle \tag{6}$$

is the autocorrelation function. It expresses the correlation between the densities measured at any two points separated by a distance r averaged over V, the irradiated volume.

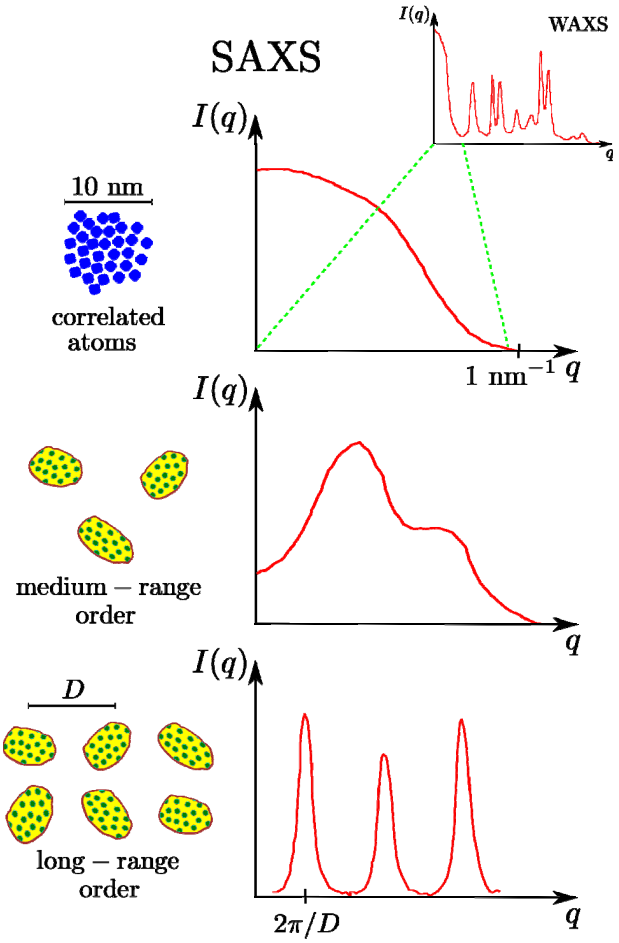

Figure 7. SAXS probes structures much larger than the atoms, it studies the inhomogeneities of a continuous medium. The two bottom diagrams present the differences in scattering profiles arising from the geometry of the particles and from the interactions between them.

In this framework there are some particularly interesting limits. The first is Porod's limit, it happens for correlations over distances r that are much smaller than some typical characteristic lengths in the sample (ξ), hence $r << \xi$. In this case only information about the characteristics of the interface is present since that is the only term with correlation. In that case the scattered intensity will be proportional to q^{-4} [48, 49] assuming smooth interfaces. This result is valid as long as the interface is seen as sharp which breaks down for distances

on the order of the interfacial thickness (ξ_i). As a consequence Porod's law deviates from this particular power-law behavior at some $q \cong 1/\xi_i$. Hence, it is possible to obtain information about the interfacial thickness.

Another interesting limit is the Guinier range. Guinier demonstrated [50] that when $qR \ll 1$ for a particle of radius R , the scattering at low angle is related to the radius of gyration of the particle, R_g , given by

$$I(q) = I_0 \exp\left(-\frac{q^2 R_g^2}{3}\right) \tag{7}$$

in the case of isolated particles. Hence a plot of ln I(q) versus q^2 is linear in this limit and the radius of gyration can be extracted from its slope. Note that the very small angle ($qR \ll 1$) and non-interacting (diluted) particles conditions must be met in order to for it to be valid.

One last limit of interest is the asymptotic range. For isolated particles having a well defined shape (sphere, disk, rod) the intensity at wider angles provides useful information about shape [47]. For example, a homogenous sphere of radius *R* displays a scattered intensity as [38]

$$I(q) \propto \left[3\frac{\sin qR - qR\cos qR}{(qR)^2}\right]^2 . \tag{8}$$

Any polydispersity or deviation from that shape will smear out the features of this asymptotic behavior. Biological macromolecules in solution usually meet these requirements to observe [51].

In case the sample is made of interacting particles (as those in the present work could), the scattered intensity depends on both the geometry of the particles and their spatial correlations. For identical, centrosymmetric and randomly oriented samples [38], the scattered intensity can be factorized in two terms as

$$I(q) = S(q)P(q), \tag{9}$$

where $S(q)$ is the structure factor describing the spatial ordering of the particles and $P(q)$ is the form factor of the particles which depends on the dimensions and the internal structure of the individual particles. Hence, the separation of these two contributions is a problem that one has to deal with, Figure 8 illustrates that it is neither possible to directly extract the characteristic lengths associated to the particles nor their organization.

Hence, the analysis of SAXS data usually relies on modeling the system and also on data from other experiments in a self-consistent way. Current developments allow the determination of 3D structures from the scattering intensity through use of ab initio methods [52-54].

The SAXS experiment was performed using samples prepared containing 3% NaFHT by mass and using ten different sodium chloride concentrations in the range 0.1 – 25 mM. They were poured into thin-walled quartz capillaries of 2 mm diameter which were sealed with melted wax.

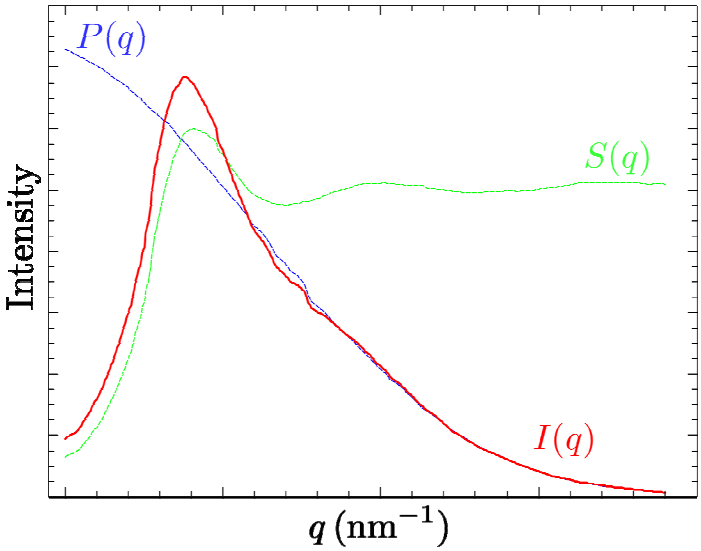

Figure 8. Structure and form factors for a system of centrosymmetric particles. The scattered intensity does not show attributes of the individual particles (Guinier range is gone) and the peak characterizing the organization of the particles is displaced.

2.6 Phase separation and segregation in colloidal systems

Colloids are an intermediate state between a suspension and a true solution, they are characterized by particles with at least one dimension in the nanometer to micrometer range – bigger than the molecules of the medium but too small do be observed with a normal microscope – evenly dispersed in a medium. Hence, they do not belong to the three states of matter but represent a state of its own with properties unlike those of the medium or of the particles [55]. These systems are of fundamental importance, examples of colloidal systems include aerogel, air particulates, cells, cheese, fog, gelatin, hand cream, jelly, latex paint, mayonnaise, milk, mist, opal, pigmented ink, pumice, ruby glass, smoke, Styrofoam, toothpaste and whipped cream.

The study of colloids started in 1861 by Thomas Graham and is currently a very popular subject as demonstrated by the number of publications and journals addresing the subject. Colloids are separated in different categories according to the states of matter of its medium and dispersed phase, as shown in Table I [56].

Table I. Colloid classification.

	Dispersed medium			
Continuous Medium		Gas	Liquid	Solid
	Gas	–	Liquid aerosol	Solid aerosol
	Liquid	Foam	Emulsion	Sol, paste, colloidal suspension
	Solid	Solid foam	Solid emulsion	Solid suspension

As seen above, clays meet the colloidal size requirements and therefore can form colloids. They are often distinguished from other colloidal materials by the highly anisotropic shape [57-59].

Colloidal dispersions are metastable rather than equilibrium systems [60]. Their particles undergo Brownian motion and are constantly interacting with each other, hence the balance of attractive and repulsive forces determines the stability of the dispersion [61]. Attractive interactions among the particles arising – for example – from van der Waals forces, can separate the dispersed phase from the liquid medium. These forces must be counterbalanced by repulsive forces such as Coulombic and steric interactions. In case there is no potential barrier between the interacting colloid particles [62], they can attract each other and aggregate. In case this aggregation is reversible, it is denoted flocculation and is characterized by loose arrangements of aggregates known as flocs. On the other hand, if this aggregation is irreversible it is termed coagulation. Often the distinction between reversible and irreversible aggregation is ill-defined [61].

2.6.1 Phase separation in aqueous dispersions

The variety of attractive and repulsive forces between colloidal particles [63] leads to a very interesting phase behavior. For instance, one can observe a transition from a liquid-like phase to a solid-like phase. An example is aggregated polymer latex particles in water [64-66], in this case the particles are spherical and almost monodisperse; as the particle concentration is increased, by evaporation of the liquid, there is a transition from a disordered state (liquid-like) to a crystalline packing of the particles.

For colloidal dispersions, the particle interaction and therefore the phase transitions can be controlled in a number of ways [67]. In the case of the electrostatically stabilized clay sols studied here [68] two methods were employed: 1) changes in electrolyte concentration, this affects the Debye screening length and reduces the magnitude of the electrostatic repulsion relative to the van der Walls attraction; 2) modification of concentration of the dispersed material, causing a decrease in the excluded volume of the studied anisotropic particles [58].

The balance between electrostactic repulsions and van der Waals attractions is described by the DLVO theory [62]; named after Deryaguin, Landau, Verwey, and Overbeek [69, 70].

2.6.2 Isotropic–nematic transition

Reports on the isotropic to nematic phase transition exist for a number of anisotropic-shaped colloids. Interesting examples include the rod-like tobacco mosaic virus [71] and platelet clay particles [23], Lars Onsager proposed an explanation for the transition purely on entropic grounds [58]. According to Onsager, as the particles align, their excluded volume decrease, and they are free to explore a larger fraction of the volume without interference from other particles. Hence translational entropy increases with alignment of the particles (decrease in orientational entropy). In this framework, for systems of clays, both particle concentration and electrolyte concentration determine particle ordering.

2.6.3 Glasses and/or gels

A current debate in colloidal systems regards the nature of the arrested state. Different groups have been using the terms gel and glass with different meanings and a number of recent publications show this lively debate [72-78]. This can be exemplified by the fact that the formation of a bonding gel is identified by some as gel while for another part of the scientific community that classifies it as a glass [77].

Also, the recent discovery of attractive glasses for spherical colloids [79] suggests that gels and glasses are no necessarily distinct states of matter but rather metastable minima in an otherwise complicate free-energy landscape [72]. This has also been suggested by simulations [80].

An interesting proposition [78] is that in a gel the attraction between colloidal particles is the guiding mechanism for gelation, whereas a glass can be formed by either repulsion (hard-sphere or Wigner glass [81]) or by attraction (attractive glass [73]).

2.7 Introduction to the articles

2.7.1 Visual observations: Papers 1 and 2

In these two papers, we have studied colloidal suspensions of synthetic Na-fluorohectorite clay particles in aqueous salt solutions. These suspensions make excellent model systems for the study of interactions between plate-shaped particles, due to the inherent possibility of tuning their electrostatic repulsion with the concentration of the salt. Various gel and sol structures are possible, including nematic liquid crystalline order, although only qualitative identification of the latter in clay colloids has been available so far.

We present visual observations of birefringence in these systems; these new observations support the interpretation of our earlier x-ray experiments [20], and thus our new results provide further evidence for nematic order. We have studied stable strata of gravity define phase separation in ionic NaCl suspensions of synthetic Na-Fluorohectorite clay. We have observed how the strata depend on clay concentration as well as on salt NaCl contents of the suspension. The mass distribution in the isotropic and in the nematic phase, as well as the density variation at the isotropic – nematic interface, indicate that existing models [82, 83], and assumptions in existing simulations [84, 85] do not account for the present system behavior. We suggest that this could be due to the polydispersity and/or due to the irregular shape of our Na-Fluorohectorite particles, as well as due to effects of the double layer, which could result in an overlap of, and even possibly a competition between, nematic ordering and gelation, in our system.

The dependence on ionic NaCl strength display three main visual regimes irrespective of clay concentration: At low ionic strength ($\sim 10^{-4}$ M – $\sim 5\times10^{-3}$ M) the Debye screening length is longer than the van der Waals force range. In this regime, the particles repel each other electrostatically, and entropy driven nematic ordering, in the Onsager sense, may occur, although gelation effects may also play an integral role. For ionic strengths above about 5×10^{-3} M, we believe that the van der Waals force comes into play, and particles attract each other according to the DLVO model. For ionic strengths above $\sim 10^{-2}$ M the clay particles aggregate in bigger assemblies which reduces the observed birefringency.

We have studied the nematic phase in detail between crossed polarizers, and we have found textures showing nematic Schlieren patterns, and by rotating polarizers as well as samples, we have seen examples of disclinations of strengths –1 and –1/2. These patterns can be observed directly by eye, reflecting the large size of the Na-fluorohectorite particles, and thus domain sizes in this system.

For Paper 1, the present author (DMF) was involved in the preparation of the manuscript and its revision, whereas for Paper 2, the present author's role was in the preparation of some of

the samples, on the discussion about how to perform the experiment and in discussing the preliminary results. Paper 2 is the result of the work done mainly by Nils Ivar Ringdal during his Master thesis work.

2.7.2 Structural investigations: Papers 1, 3 and 4

In these three papers, we present x-ray scattering studies of polydisperse suspensions of fluorohectorite clay in saline solutions. Since, the suspended clay colloids consist of stacks of nano-silicate sheets several tenths of a nanometer thick, one may observe Bragg scattering from these particles, i.e. Wide Angle X-ray Scattering (WAXS) diffractograms may be recorded, as in Paper 1, resulting in isotropic or oriented WAXS patterns for the isotropic and nematic phases respectively of such systems. The x-ray data included in Paper 1 represent a summary of the earlier work of DiMasi et al. [20], hence no new x-ray work is reported in Paper 1.

Precise characterization of the phase diagram of the samples as a function of salt concentration and vertical position in the tubes, based on SAXS data, is presented in Papers 3 and 4. The vertical positions of the phase boundaries were monitored by analyzing the eccentricity of elliptic fits to iso-intensity cuts of the scattering images. The intensity profiles along the two principal directions of scattering display two power-law behaviors with a smooth transition between them and show the absence of positional order in all phases. We employed SAXS to determine the proper phase diagram for the NaFHT-NaCl-H_2O system, for which all gel/glass phases are visible simultaneously in each sample tube. The high polydispersity and the interaction of the particles did not allow us to fully understand the structural arrangement in the different phases, but we believe that there are different arrested states (gel and glass phases) in the phase diagram, though further investigation is needed to corroborate that. For future studies to be able to define particle conformation in all phases, information on the particle-size distributions as a function of height in the sample tubes would be useful. To accomplish this, we believe that a cryo-fracture study of the phase diagram should suffice.

The use of a 2D detector and analysis of the data along the two semi axes proved useful in determining the orientational configuration of the platelets in the nematic phase and to some extent in the flocculated phase.

The particle configuration at the center of the tube made it impossible to completely decouple the optical axes of the particles. A new experiment using narrow rectangular-section cells instead of circular ones will probably allow more information to be extracted from the scattering intensity curves. However, by confronting the results from Ref. [10] to our observations, we were able to determine a plausible collective organization of the particles in the nematic phase.

Particles in the nematic and isotropic phases were observed to have similar thickness, whereas the flocculated phase presents thicker particles. The particles in the nematic phase have their edges close to the glass walls of the tube and the platelets are standing (their normal is perpendicular to the tube axis). Particles in the flocculated phase have an almost isotropic distribution of orientations when compared to the nematic phase, but a slight higher number of platelets are lying flat.

The present author (DMF) contributed in all processes of the creation of Papers 3 and 4, i.e. prepared the experiment, performed it together with the other coauthors, did most of the data analysis, and I was involved in the manuscript preparation and its revision.

2.7.3 Transitions by water intercalation: Papers 5 and 6

In the work represented by Papers 5 and 6, the authors performed synchrotron x-ray scattering studies of the dynamics of the water intercalation front in a Na-Fluorohectorite clay. Like other smectite clays, fluorohectorite particles can swell due to intercalation of successive water layers. Monitoring the intensities of WAXS Bragg peaks of the known 1- and 2-water-layer hydration states at different positions in the sample enabled spatial and temporal measurement of the proportions of the different hydration states.

From experiments with controlled temperature and an imposed humidity gradient on a quasi one-dimensional powder sample, the authors were able to localize the intercalation front and demonstrate that the width of this front was smaller than 2mm after penetrating 9mm into the sample. The speed at which the intercalation front advanced through the sample during the diffusion process was shown to decrease with time, as expected in a diffusion like process. The diffraction signature of random water intercalation in the vicinity of the intercalation front also provided information on the changes in the water content of the mesopores around clay particles.

The present author's (DMF) contribution to papers 5 and 6 was in building a temperature control setup used in the experiment, as well as in taking part in parts of the measurements, and marginal involvement in the manuscript preparations.

2.7.4 Oil dispersions under a DC electric field: Paper 7

This paper, which is one of the main publications in the PhD thesis of Kanak Parmar [86] (PhD defense November 2006), is concerned with structuring of clay particles suspended in silicone oil, and subjected to external DC-electric fields of order of magnitude 1kV/mm, i.e. this is an example of a so-called electrorheological system [86]. Microscopy observations show that suspensions of synthetic and natural nanolayered smectite clay particles submitted to such a strong external electric field undergo a fast and extended structuring. This structuring results from the interaction between induced electric dipoles. The authors show that WAXS, synchrotron x-ray scattering experiments provide the orientation distributions for the particles. These distributions are understood in terms of competition between homogenizing entropy and interaction between the particles and the local electric field. The recorded WAXS patterns show they show that clay particles polarize along their silica sheets. The induced dipole is structurally attached to the particle, and this causes particles to reorient and interact, resulting in the observed macroscopic structuring.

The present author (DMF) took part in the experiment of Paper 7 together with the other coauthors, and also contributed to the revision of the manuscript.

Bibliography

[1] P. G. De Gennes and J. Prost, *The Physics of Liquid Crystals*, volume 83 of *International Series of Monographs on Physics*, Clarendon Press, Oxford, 2nd edition, 1993.

[2] B. R. Acharya, A. Primak, and S. Kumar, Phys. Rev. Lett. **92**, 145506 (2004).

[3] M. J. Freiser, Phys. Rev. Lett. **24**, 1041 (1970).

[4] L. A. Madsen, T. J. Dingemans, M. Nakata, and E. T. Samulski, Phys. Rev. Lett. **92**, 145505 (2004).

[5] S. Kralj and E. G. Virga, Phys. Rev. E **66**, 021703 (2002).

[6] F. Bergaya, B. K. G. Theng, and G. Lagaly, editors, *Handbook of Clay Science*, Elsevier Science, Amsterdam, 2006.

[7] F. G. Rossman and C. J. van Oss, *Colloid and Surface Properties of Clays and Related Minerals*, volume 105 of *Surfactant Science Series*, Marcel Dekker, New York, 2002.

[8] A. P. Sullivan and P. K. Kilpatrick, Ind. Eng. Chem. Res. **41**, 3389 (2002).

[9] B. Velde, *Introduction to Clay Minerals: Chemistry, Origins, Uses and Environmental Significance*, Chapman & Hall, London, 1992.

[10] J. E. Gillott, *Clay in Engineering Geology*, Elsevier, 2nd edition, 1987.

[11] R. L. Handy, *The Day the House Fell: Homeowner Soil Problems from Landslides to Expansive Clays and Wet Basements*, American Society of Civil Engineers, 1995.

[12] A. Violante, P. M. Huang, J.-M. Bollag, and L. Gianfreda, editors, *Dynamics, Mobility and Transformation of Pollutants and Nutrients*, Elsevier Science, 2002.

[13] A. Violante, P. M. Huang, J.-M. Bollag, and L. Gianfreda, editors, *Ecological Significance of the Interactions among Clay Minerals, Organic Matter and Soil Biota*, Elsevier Science, 2002.

[14] E. Manias et al., Chem. Mater. **13**, 3516 (2001).

[15] P. Podsiadlo et al., Science **318**, 80 (2007).

[16] S. Guggenheim et al., Clays and Clay Minerals **54**, 761 (2006).

[17] D. M. Moore and R. C. Reynolds, *X-ray Diffraction and the Identification and Analysis of Clay Minerals*, Oxford University Press, New York, 2nd edition, 1997.

[18] P. D. Kaviratna, T. J. Pinnavaia, and P. A. Schroeder, J. Phys. Chem. Solids **57**, 1897 (1996).

[19] G. J. da Silva, J. O. Fossum, E. DiMasi, K. J. Måløy, and S. B. Lutnæs, Phys. Rev. E **66**, 011303 (2002).

[20] E. DiMasi, J. O. Fossum, T. Gog, and C. Venkataraman, Phys. Rev. E **64**, 061704 (2001).

[21] J. O. Fossum et al., Energy **30**, 873 (2005).

[22] A. Mourchid, A. Delville, J. Lambard, E. Lécolier, and P. Levitz, Langmuir **11**, 1942 (1995).

[23] I. Langmuir, J. Chem. Phys. **6**, 873 (1938).

[24] M. Born and E. Wolf, *Principles of Optics: Electromagnetic Theory of Propagation, Interference and Diffraction of Light*, Cambridge University Press, Cambridge, 6th edition, 1997.

[25] F. C. Frank, Discuss. Faraday Soc. **25**, 19 (1958).

[26] N. D. Mermin, Rev. Mod. Phys. **51**, 591 (1979).

[27] R. Repnik, L. Mathelitsch, M. Svetec, and S. Kralj, Eur. J. Phys. **24**, 481 (2003).

[28] L. J. Michot et al., Proceedings of the National Academy of Sciences **103**, 16101 (2006).

[29] J. Als-Nielsen and D. McMorrow, *Elements of Modern X-ray Physics*, John Wiley & Sons, Chichester, 2000.

[30] W. L. Bragg, Proc. Cambridge Philos. Soc. **17**, 43 (1913).

[31] Brindley and Brown, *Crystal structures of clay minerals and their X-ray identification*, Mineralogical Society, London, 1980.
[32] R. C. Reynolds, Reviews in Mineralogy and Geochemistry **20**, 1 (1989).
[33] L. A. Feigin, *Structure Analysis by Small-Angle X-Ray and Neutron Scattering*, Kluwer Academic/Plenum Press, 1987.
[34] G. J. da Silva, J. O. Fossum, E. DiMasi, and K. J. Måløy, Phys. Rev. B **67**, 094114 (2003).
[35] S. B. Hendricks, R. A. Nelson, and L. T. Alexander, J. Am. Chem. Soc. **40**, 1457 (1962).
[36] S. Hendricks and E. Teller, The Journal of Chemical Physics **10**, 147 (1942).
[37] O. Glatter and O. Kratky, editors, *Small Angle X-ray Scattering*, Academic Press, London, 1982.
[38] A. Guinier and G. Fournet, *Small Angle Scattering of X-Rays*, John Wiley & Sons, New York, 1955.
[39] H. D. Bale and P. W. Schmidt, Phys. Rev. Lett. **53**, 596 (1984).
[40] A. F. Craievich, Mat. Res. **5**, 1 (2002).
[41] G. Dietler, C. Aubert, D. S. Cannell, and P. Wiltzius, Phys. Rev. Lett. **57**, 3117 (1986).
[42] A. Erzan and N. Güngör, J. Colloid Interface Sci. **176**, 301 (1995).
[43] S. Förster et al., Journal of Physical Chemistry B **109**, 1347 (2005).
[44] T. Freltoft, J. K. Kjems, and S. K. Sinha, Phys. Rev. B **33**, 269 (1986).
[45] T. Frühwirth, G. Fritz, N. Freiberger, and O. Glatter, J. Appl. Crystallogr. **37**, 703 (2004).
[46] P. W. Schmidt, *The Fractal Approach to Heterogeneous Chemistry: Surfaces, Colloids, Polymers*, chapter 2.2, pages 67–79, John Wiley & Sons, New York, 1989.
[47] C. Williams, *Small Angle Scattering from Solids and Solutions*, volume I — Theory, Instruments and Methods of *HERCULES — Neutron and Synchrotron Radiation for Condensed Matter Studies*, chapter X, pages 235–244, EDP Sciences/Springer-Verlag, 1993.
[48] B. D. Cullity and S. R. Stock, *Elements of X-Ray Diffraction*, Prentice Hall, New Jersey, 3rd edition, 2001.
[49] G. Porod, Kolloid. Z. **124**, 83 (1951).
[50] A. Guinier, *X-ray Diffraction: In Crystals, Imperfect Crystals and Amorphous Bodies*, Dover Publications, New York, 1994.
[51] P. Lindner and T. Zemb, editors, *Neutron, X-rays and Light. Scattering Methods Applied to Soft Condensed Matter*, North Holland, Amsterdam, 2002.
[52] M. H. J. Koch, P. Vachette, and D. I. Svergun, Quarterly Reviews of Biophysics **36**, 147 (2003).
[53] M. V. Petoukhov and D. I. Svergun, Current Opinion in Structural Biology **17**, 562 (2007).
[54] D. I. Svergun, Journal of Applied Crystallography **33**, 530 (2000).
[55] C. A. Murray and D. G. Grier, American Scientist **83**, 238 (1995).
[56] D. J. Shaw, *Introduction to Colloid and Surface Chemistry*, Butterworth-Heinemann, Oxford, 4th edition, 1992.
[57] L. J. Michot et al., Langmuir **20**, 10829 (2004).
[58] L. Onsager, Ann. N.Y. Acad. Sci. **51**, 627 (1949).
[59] D. van der Beek, *Liquid crystal phase behavior of colloidal platelets in external fields*, PhD thesis, Utrecht University, 2005.
[60] P. Poulin, H. Stark, T. C. Lubensky, and D. A. Weitz, Science **275**, 1770 (1997).
[61] I. W. Hamley, *Introduction to Soft Matter: Polymers, Colloids, Amphiles and Liquid Crystals*, John Wiley & Sons, Chichester, 2000.

[62] J. N. Israelachvili, *Intermolecular and Surface Forces*, Academic Press, London, 2nd edition, 1991.
[63] R. A. L. Jones, *Soft Condensed Matter*, Oxford University Press, Oxford, 2002.
[64] P. Bartlett, R. H. Ottewill, and P. N. Pusey, Phys. Rev. Lett. **68**, 3801 (1992).
[65] M. D. Eldridge, P. A. Madden, P. N. Pusey, and P. Bartlett, Mol. Phys. **84**, 395 (1995).
[66] C. He and A. M. Donald, Langmuir **12**, 6250 (1996).
[67] W. B. Russel, D. A. Saville, and W. R. Schowalter, *Colloidal Dispersions*, Cambridge University Press, Cambridge, corrected edition, 1992.
[68] H. van Olphen, *An Introduction to Clay Colloid Chemistry: For Clay Technologists, Geologists, and Soil Scientists*, John Wiley & Sons, New York, 2nd edition, 1977.
[69] B. V. Deryagin and L. D. Landau, Acta. Physicochim. URSS **14**, 633 (1941).
[70] J. W. Verwey and J. T. G. Overbeek, *Theory of the Stability of Lyophobic Colloids*, Dover Publications, 2003.
[71] F. C. Bawden, N. W. Pirie, J. D. Bernal, and I. Fankuchen, Nature **138**, 1051 (1936).
[72] S. Jabbari-Farouji, G. H. Wegdam, and D. Bonn, Phys. Rev. Lett. **99**, 065701 (2007).
[73] H. Tanaka, J. Meunier, and D. Bonn, Phys. Rev. E **69**, 031404 (2004).
[74] D. Bonn, H. Tanaka, H. Kellay, G. Wegdam, and J. Meunier, Langmuir **15**, 7534 (1999).
[75] E. Zaccarelli, J. Phys.: Condens. Matter **19**, 323101 (2007).
[76] H. Z. Cummins, J. Non-Cryst. Solids **353**, 3891 (2007).
[77] F. Sciortino, Gel-forming patchy colloids and network glass formers: Thermodynamic and dynamic analogies, arXiv:0711.2220v1 [cond-mat.soft].
[78] B. Ruzicka et al., Phys. Rev. E **77**, 020402 (2008).
[79] K. N. Pham et al., Science **296**, 104 (2002).
[80] F. Sciortino, S. Mossa, E. Zaccarelli, and P. Tartaglia, Phys. Rev. Lett. **93**, 055701 (2004).
[81] D. Bonn, H. Tanaka, G. Wegdam, H. Kellay, and J. Meunier, Europhys. Lett. **45**, 52 (1999).
[82] D. van der Beek and H. N. W. Lekkerkerker, Europhys. Lett. **61**, 702 (2003).
[83] F. M. van der Kooij and H. N. W. Lekkerkerker, J. Phys. Chem. B **102**, 7829 (1998).
[84] M. A. Bates and D. Frenkel, J. Chem. Phys. **110**, 6553 (1999).
[85] M. A. Bates, J. Chem. Phys. **111**, 1732 (1999).
[86] K. P. S. Parmar, *Oil Dispersion of Nanolayered Silicates in an External Electric Field: An Experimental Study*, PhD thesis, Norwegian University of Science and Technology, 2006.

Paper 1

J. O. FOSSUM, E. GUDDING, D. D. M. FONSECA, Y. MEHEUST, E. DIMASI, T. GOG AND C. VENKATARAMAN

Observations of orientational ordering in aqueous suspensions of a nano-layered silicate

Energy **30**, 873–883 (2005)

Available online at www.sciencedirect.com
SCIENCE DIRECT®
Energy 30 (2005) 873–883
ENERGY
www.elsevier.com/locate/energy

Observations of orientational ordering in aqueous suspensions of a nano-layered silicate

J.O. Fossum [a], E. Gudding [a], D. d. M. Fonseca [a,*], Y. Meheust [a], E. DiMasi [b], T. Gog [c], C. Venkataraman [c]

[a] *NTNU, Department of Physics, The Norwegian University of Science and Technology, N-7491 Trondheim, Norway*
[b] *Brookhaven National Laboratory, Physics Department, Upton, NY 11973-5000, USA*
[c] *Argonne National Laboratory, CMC-CAT, Advanced Photon Source, Argonne, IL 60439, USA*

Abstract

We have studied colloidal suspensions of clay particles in aqueous salt solutions. These suspensions make excellent model systems for the study of interactions between plate-shaped particles, due to the inherent possibility of tuning their electrostatic repulsion with the concentration of the salt. Various gel and sol structures are possible, including nematic liquid crystalline order, although only qualitative identification of the latter in clay colloids has been available so far. Here, we briefly review our earlier synchrotron X-ray diffraction from gravity dispersed solutions of Na fluorohectorite, a synthetic swelling clay, over a large NaCl concentration range. Our use of liquid X-ray scattering techniques allowed us to identify regions in which particles reorient from horizontal to vertical alignments in strata coexisting at different heights within the sample. We thus identified two distinct gel regions characterized by differences in orientational anisotropy and domain size. In addition, we for the first time, present visual observations of birefringence in these systems; these new observations support the interpretation of our X-ray experiments, and thus our new results provide further evidence for nematic order.

1. Introduction

Understanding the role of salt in stabilizing dense clay phases has practical significance, for example, in the context of clay formations originally sedimented in salt water, which can be progressively destabilized by subsequent fresh-water rinsing. Clay is one of the traditional materials, whose applications have played important roles throughout human history. Common present day uses of 2:1 clays thus include building materials, ceramics, rheology modification, catalysis, paper filling, oil well-drilling and -stability, etc. [1].

* Corresponding author. Fax: +47-73597710.
E-mail address: davi.fonseca@phys.ntnu.no (D.d.M. Fonseca).

0360-5442/$ - see front matter © 2004 Elsevier Ltd. All rights reserved.
doi:10.1016/j.energy.2004.04.008

Smectite 2:1 clay particles dispersed in salt solutions have been studied for decades [2]. More recently there has been a growing activity in the studies of complex physical phenomena in clays [3,4]. The individual 2:1 particles are composed of one or more silicate lamellae that stack by sharing exchangeable cations between their faces (Figs. 1a and 1b). Much effort has gone into relating the structural and rheological properties of clay–salt suspensions to optical observations, which find birefringent domains with defect textures characteristic of nematic liquid crystals [5,6]. Small-angle neutron scattering measurements have also suggested the presence of local orientational correlations in smectite clay gels [7]. Direct in situ structural evidence for parallel alignment of platelets, however, has only recently been obtained [8,9].

Although the layered subunit is crystalline, relative registry and orientations between lamellae are usually quite disordered. Substitution of metals within the silicate layer produces a surface charge, which together with exchangeable intercalated cations affects the absorption of water into the interlayer space, and hence controls the layer spacing [10]. These features determine a net negative surface charge for the particle, and in combination with the particle size and the interactions with the screening salt in solution, produce a rich phase behavior in the clay suspensions [2,5,11].

The complexity arises from the several ways in which attractive and repulsive forces act. When van der Waals attraction between the particles is balanced by electrostatic repulsion, particles can remain dispersed, settling only slowly out of solution. Ions from an electrolyte, if present, can screen the repulsive forces between particles and allow them to aggregate together. This aggregation or ''flocculation'' may cause the particles to quickly settle out of suspension [2].

On the other hand, attracted particles may join to form extended networks, resulting in gels. Because the particles will, in general, have a negative surface charge partly compensated by positive charge at the particle edges, it is often suggested that the particles are connected in edge-to-face configurations (Fig. 1c): the result is a suggested isotropic, so-called ''house of cards'' structure that has inspired many theoretical investigations [12], although most recent experimental work has failed to verify this model. Alternative and very interesting structural correlations that may be expected in these systems are those of liquid crystal phases [13].

Within the physics community, there has been particular interest in nematic phases in platelet systems in general, i.e. parallel orientation of the platelets without long-range positional order [13–15]. If the system is made dense enough, it becomes favorable for anisotropic particles

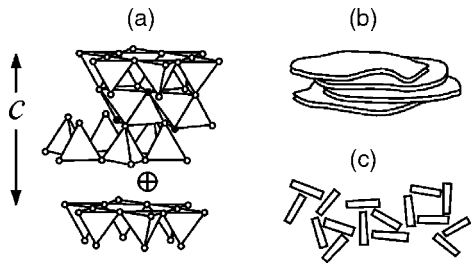

Fig. 1. Taken from DiMasi et al. [8]: (a) Generic structure of fluorohectorite synthetic clay. (b) Micron-scale clay particle formed from stacked lamellae. (c) Face-to-edge and edge-to-edge aggregation of clay particles.

(i.e. rod shaped particles like those utilized in commercial LCD displays, or platelet shaped like in the clay systems discussed here) to align, giving up orientational entropy in exchange for much greater positional entropy. Thus, in plate colloid systems, a transition from an isotropic to a nematic phase is expected at a critical particle density [16]. The salt concentration plays a subtle role here in addition to determining the overall magnitude of repulsive forces, because the spatial extent of electrical diffuse layers modifies the effective anisotropy of the interacting particles [17]. The strong influence of polydispersity in particle size and aspect ratio on the phase diagram of plate colloids is the focus of numerous recent articles [18–21].

In this report, we describe suspensions of the synthetic 2:1 smectite clay Na fluorohectorite (Na-Fh) in aqueous NaCl solutions. Like natural hectorite, Na-Fh is a swelling clay that incorporates a variable amount of water in the interlayer space, resulting in a change in lattice constant along the stacking direction. Na-Fh has a rather large surface charge of 1.2 e^-/unit cell, compared, for example, to other synthetic smectites such as laponite (0.4 e^-/unit cell). [22]. Na-Fh also has a quite large and variable particle size of up to 20 000 Å in diameter [22], and compared to natural clays such as montmorillonite, might be expected to have a more homogeneous composition and charge distribution. The polydispersity in particle size makes the Na-Fh suspensions particularly interesting, because gravitational forces effectively sort the particles by size, stabilizing in some cases several strata of gels, sols and/or sediments within a single sample tube [3,4].

Our aim with the present studies has been to learn about the structural correlations in this system. In particular, we have conducted synchrotron X-ray scattering experiments that are sensitive to the orientation of the particles within the stabilized strata of gels, sols and/or sediments within single sample tubes. In order to check our conclusions about structural particle arrangements, we have subsequently performed visual observations including birefringence studies of the same samples, thus enabling us to suggest a phase diagram of stable phases for this system.

2. Methods

2.1. Samples

Fluorohectorite clay was purchased in powder form from Corning Inc. in New York, and ion exchanged through dialysis to produce Na-fluorohectorite having the nominal chemical formula $Na_{0.6}Mg_{2.4}Li_{0.6}Si_4O_{10}F_2$. For the present experiments, solutions were prepared having 2.91–2.94 weight% clay in NaCl concentrations ranging from 1.0×10^{-4} to 1.2×10^{-2} M.

From 5 to 10 days before the X-ray experiments, the suspensions were shaken thoroughly and poured from their original containers into sealed glass tubes ~8 mm in diameter, with wall thicknesses of 0.2–0.3 mm. Since the experiments on each sample took from one to two days, the last samples studied had a week or more to settle, while those measured first had been sitting only for a few days after being remixed. This was enough time for the strata to stabilize, as judged by boundaries visible to the eye that remained at a fixed height. However, some of our X-ray results suggest that settling or gelation was still occurring within these strata on some samples. Unless noted otherwise, we present here X-ray scattering results only from samples that seemed to be stable on the scale of 10 h. All samples were reexamined five months later,

and at this time the gel regions took up much less volume than in our X-ray study, with much larger volumes of clear liquid at the top of the tubes.

For the visual birefringence experiments described below, samples that had settled for more than a month were studied. For these studies, sample cuvettes with effective sample volumes of about $5 \times 5 \times 30$ mm^3 were used.

Other experiments have also been done by us on samples based on the same Corning powder material. In particular, we have recently performed detailed hydration and dehydration static and dynamic studies in dry pressed bulk samples by means of X-ray synchrotron scattering techniques, thus gaining detailed micro- and nano-structural information about these systems for various temperatures and humidity conditions [23,24].

2.2. Visual observations

Samples were allowed to settle for one month in sample cuvettes as described above. Each phase boundary was measured simply by means of a ruler, and the same procedure was repeated by placing each sample cuvette in between crossed polarizers in order to gain insight into the liquid crystalline nature of the various phases.

2.3. Synchrotron X-ray scattering methods

Because the sample tubes cannot be tilted in the X-ray beam without disturbing the boundaries between the strata, we have made use of a specialized spectrometer designed for the study of liquid surfaces [8]. The present X-ray scattering measurements were carried out using the CMC-CAT liquid surface spectrometer at beamline 9ID-C at the Advanced Photon Source, Argonne National Laboratory, USA. Using the third harmonic of the undulator, the X-rays were monochromised at 19 keV, which corresponds to an X-ray wavelength of 0.653 Å. Incident slits restricted the beam spot size to 0.4×0.4 mm^2. The instrumental resolution was determined principally by 0.5×0.5 mm^2 slits before the NaI single channel detector, 600 mm from the sample.

Different strata within each sample tube were positioned in the beam by means of an elevator stage. We made measurements in two different scattering geometries, as shown in Fig. 2. With a level incoming beam (parallel to the strata, with $\alpha = \beta = 0$), momentum transfer in the horizontal plane is a function of the scattering angle 2θ around a vertical axis: $q_{\|} = (4\pi/\lambda)\sin(2\theta/2)$. Momentum transfer along the vertical direction was achieved by tilting the beam down at an angle α to the strata, while detecting X-rays scattered upwards at angle β, with $2\theta = 0$: $q_{\perp} = (2\pi/\lambda)(\sin\alpha + \sin\beta)$. By measuring intensities of (0 0 L) Bragg peaks in both geometries, we could determine the relative populations of clay platelets in two orientations: horizontal (those lying parallel to the strata, as if flat on the floor) and vertical (as if standing upright on edge).

3. Results and analysis

3.1. Results from visual observations

Fig. 3 shows our main visual observations, and from this we may measure phase positions within each sample, and thus construct a simple phase diagram for this system as a function of NaCl concentration.

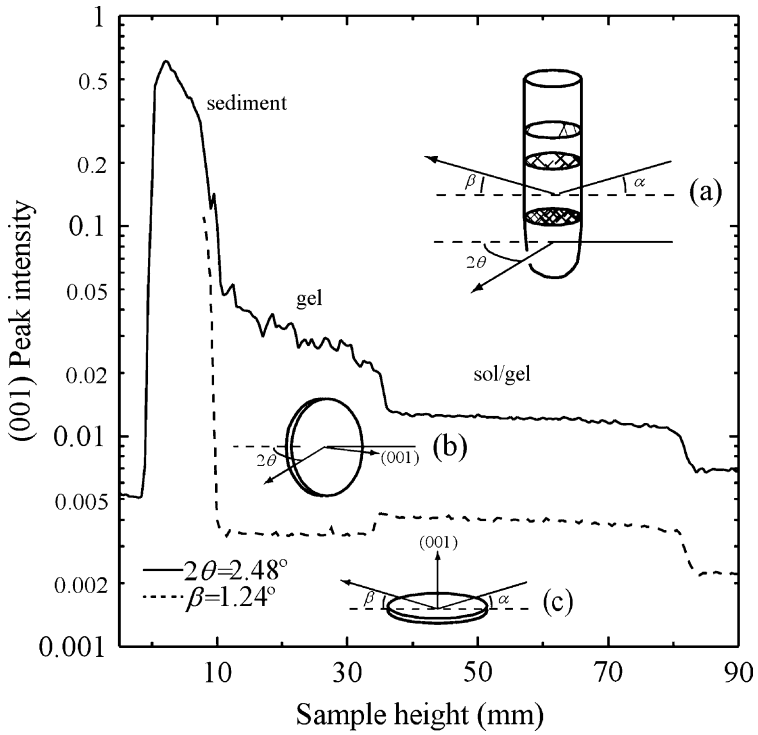

Fig. 2. Adapted from DiMasi et al. [8]: intensity at the (0 0 1) Bragg peak position as a function of beam position in the sample tube for sample with 1.0×10^{-3} M NaCl. The inset (a) shows the two scattering geometries utilized, i.e. $q_{\perp}$ probing horizontal platelets, and $q_{\parallel}$ probing vertical platelets, respectively, as discussed in the text. Top curve (b) $q_{\parallel}$. Lower curve (c) $q_{\perp}$.

We also looked at all the samples placed between crossed polarizers as exemplified in Fig. 4, and our conclusion is that for all investigated NaCl concentrations, it is only the phase located just above the sediment phase, i.e. the second phase form the bottom up in each of our samples, which is visibly birefringent to the eye.

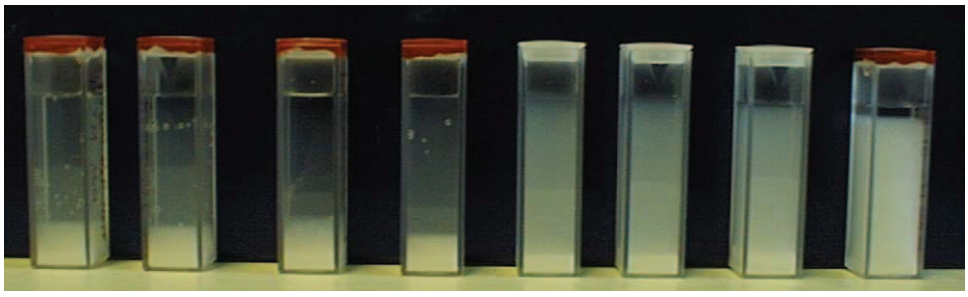

Fig. 3. Taken from Fossum [4]: samples of Na-fluorohectorite. Weight percent Na-fluorohectortie for all samples shown is 3 w/w%. From left to right, the sodium chloride concentrations are 1×10^{-4}, 5×10^{-4}, 1×10^{-3}, 3×10^{-3}, 4.5×10^{-3}, 6×10^{-3}, 8×10^{-3} and 1×10^{-2} M, respectively.

Fig. 4. Example of Na-fluorohectorite samples (3 w/w% clay) viewed when placed between crossed polarizers. The two leftmost samples: 2×10^{-3} M, the two rightmost samples 6×10^{-3}M.

3.2. Synchrotron X-ray scattering experiments

The positions and line shapes of the peaks provide specific information about the clay particles' structure and morphology. We find that the (0 0 1) peak always appears at 0.42 $Å^{-1}$, corresponding to a c lattice constant of 15.0 Å. This is the largest of three c lattice constants observed so far for Na fluorohectorite, which when dried at high temperatures has $c \sim 9.7$ Å, and can also be hydrated under cooler and more humid conditions into states having $c \sim 12.4$ and 15.0 Å, respectively [23,24]. Taken together, our observations on the peak positions and widths tell us that the particles in solution are composed of well-crystallized stacks of 20–100 of the fundamental silicate lamellae. Even when dispersed in water, this clay has no ability to hydrate further or to exfoliate in the solution, at any NaCl concentration investigated here. This behavior is probably due to the large intrinsic layer charge of Na-Fh, which does not permit further separation of the silicate layers from the intercalated cation.

By comparing intensity measured in the two different scattering geometries, we found that particle orientation as well as density changes as a function of height in the tube. Fig. 2 shows raw intensities at the (0 0 1) peak position as a function of sample height, in a tube having three strata discernible by eye. The top curves present a time series taken over 13.5 h, with the spectrometer aligned to scattering in the horizontal plane ($\alpha = \beta = 0$, $2\theta = 2.48^{\circ}$). The resulting intensity comes from that subset of vertical particles that have the correct azimuthal orientation (Fig. 2b). The intensity drops by an order of magnitude from the dense sediment ($z < 10$ mm) to the gel region just above it ($10 < z < 36$ mm), and drops again to near-background levels in

a third sol/gel layer ($36 < z < 80$ mm). These designations refer to the sample appearance, which goes from a powdery sediment at the bottom, to a very viscous cloudy region, and to a translucent white liquid above, that became viscous after about a week. The intensity variations on the scale of millimeter in the gel persist over tens or hundreds of minutes, and are apparently due to density variations in the gel as it relaxes. A sample height scan configured for horizontal platelets is shown in the bottom curve ($\alpha = \beta = 1.24^\circ$, $2\theta = 0$). The same boundaries in sample height are present, but instead of a monotonic decrease in intensity with sample height, an increased intensity is found going from the middle layer to the top layer. This is a direct evidence of particle reorientation: while the density in the top layer may indeed be lower than that of the middle one, the absolute number of horizontal platelets, with their (0 0 1) axes aligned perpendicular to the strata, has nevertheless increased there.

By fitting background-subtracted (0 0 1) X-ray Bragg peaks in the two scattering configurations mentioned above, we can assess the relative populations of horizontal and vertical platelets as a function of sample height. It is important to emphasize an essential difference between the two scattering geometries. The intensity found at the (0 0 1) position in $q_\perp$ will be proportional to all particles that are horizontal (the c axis must be aligned within 0.1° to the momentum transfer, to scatter into our resolution volume). On the other hand, the (0 0 1) intensity in $q_\parallel$ is proportional only to those vertical particles whose (0 0 1) axes have the correct azimuthal orientation, as discussed above.

The orientational anisotropy depends strongly on the salt concentration. Fig. 5 shows integrated (0 0 1) intensities for one example NaCl concentration. The vertical dashed lines separate sediment, gel, sol/gel, and "L" strata as discerned by eye. "L" refers to a clear solution in which clay Bragg peaks were generally too weak to be distinguished from the background. The label "vertical platelets" (open circles) refers to (0 0 1) intensity scattered in the horizontal plane and measured as a function of $q_\parallel$. The (0 0 1) peak of a "horizontal platelet" (closed circles) is characterized by scanning $q_\perp$.

Differences in integrated intensity are due to the combined effects of density and particle orientation. In principle, X-ray analysis can be used to obtain both the density and the particle orientation of these clay gels. Unfortunately, independent measurement of the density of the

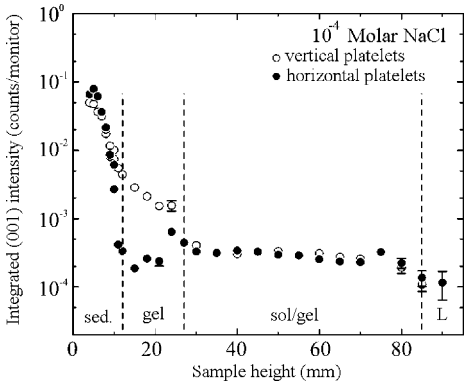

Fig. 5. Adapted from DiMasi et al. [8]: intensities of (0 0 1) peaks coming from vertical and horizontal platelets, showing dominantly vertical platelets in the nematic gel phase, as described in the text.

clay suspensions was not possible to obtain either by X-ray absorption or by scattering under the present experimental conditions. Generally, absorption is dominated by the water. For the sediment at the bottom of the tubes, irregularities in the glass, which has approximately the same mass absorption coefficient as the clay, made quantitative assessment impossible.

The simplest quantitative relationship between the two scattering configurations is the case of an isotropic phase, exemplified by the sol/gel regions in Fig. 5. Here, all particle orientations are equally probable and, therefore, the scattered intensity will not depend upon the direction of the momentum transfer. Intensities as functions of $q_{\|}$ and $q_{\perp}$ are equal, as expected. In the sediments, the samples also appear to be essentially isotropic, with a slight tendency towards predominance of horizontal particles at the bottom. Possibly this predominance of horizontal sediment particles may increase at times much larger than the typical one week sedimentation times utilized for the present X-ray experiments.

In the gels, differences in the two sets of measured intensities clearly show that the samples are anisotropic. Ratios of scattered intensity from vertical vs horizontal particles in the gels range from 10 to 100. As outlined in [6], it is very likely that we are scattering from only a tiny fraction of the vertical particles since the method is sensitive to only those with the correct azimuthal orientation. Thus, the measured anisotropies of 10–100 are only a lower bound and the real anisotropy may be several orders of magnitude greater. Thus, the gel regions of these three samples are composed almost entirely of vertical platelets, with a rather uniform distribution. This orientational anisotropy is required for nematic order, though not strictly equivalent with it. In principle, our data are also consistent with particles that are aligned with their planes in the gravitational field, but are not necessarily parallel to their neighbors. We regard the nematic order as the correct explanation; however, interactions with the tube walls are presumably responsible for the overall vertical alignment.

Since the stability of various types of liquid crystalline order is suggested to depend upon the size dispersity [19], it is important in polydisperse systems to find out the extent to which different sizes are segregated in the solution. Bragg peak width analysis gives us some indication on this, and this is discussed in [6].

4. Discussion and summary

The phase diagram of Fig. 6 summarizes the relationship between NaCl concentration and vertical positions of phase boundaries. The sediment, nematic, and isotropic regions are identified clearly, and obviously depend strongly on NaCl concentration. As we remarked above, our measurements were made within a week or two of the sample preparation, while reports on other clay gel systems report dynamic processes continuing over months or even years, see discussion in [3,4].

After five months' further settling time our (X-ray experimental) samples had changed substantially: to the eye, one or two gels occupied very small volumes above the sediments, with large regions of clear supernatant liquid. Since the volumes occupied by each phase are determined by the speed of gelation or flocculation, we can understand our observed absence of isotropic sol/gel in the salt-rich regions [18]. Here the high ionic concentration leads to more rapid settling, just as similar NaCl concentrations of 0.01–0.1 M were found to flocculate solutions of bentonite and laponite, clays that form gels when the NaCl concentration is lower [5,9,11,16].

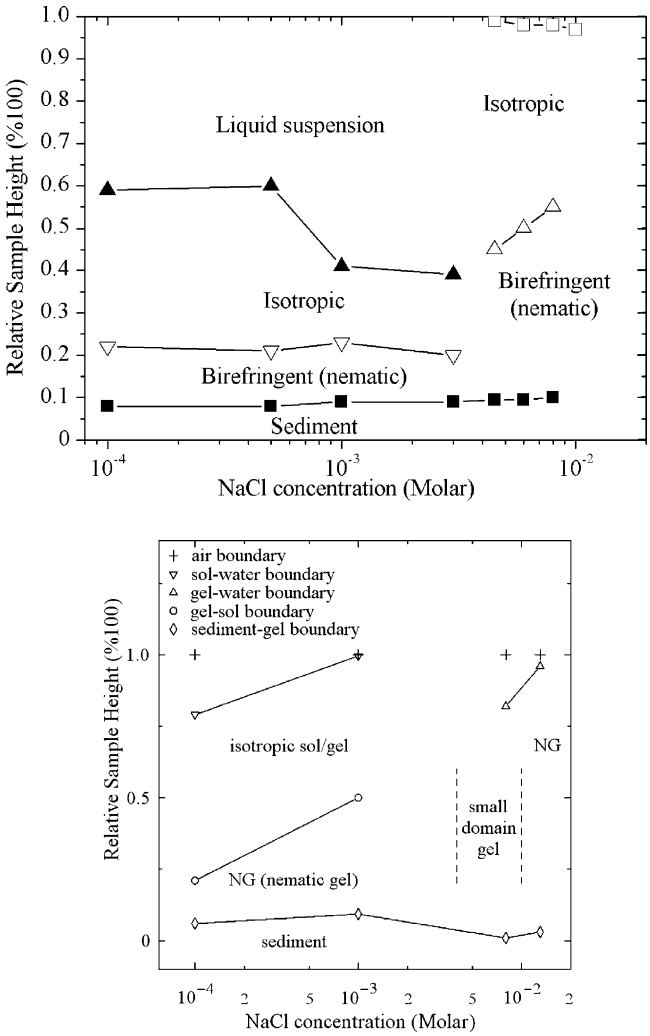

Fig. 6. Upper panel: phase diagram as determined from direct measurements of samples in Fig. 3. The next to bottom phase is birefringent for each sample plotted, indicating nematic ordering. Lower panel: taken from DiMasi et al. [8]: phase diagram as determined from direct measurements of platelet orientations, by means of synchrotron X-ray scattering. Note that the samples studied visually in (upper panel) were left to sediment for a few months, whereas the samples studied at the synchrotron (lower panel) just sedimented for a few days. This explains the more compact phases for the samples reported in the top panel as compared to the samples studied at the synchrotron.

Nowhere in the Na-Fh/NaCl system do we find a stable isotropic gel, and this may provide further evidence against the "house of cards" model.

Our scattering measurements reveal information complementary to other techniques, especially regarding the nematic gel. Our visual observations are also included in Fig. 6, and although the visually observed samples were allowed to settle for about one month before measurements were taken, we observe fair agreement between the X-ray data and the visual data for the location of phase boundaries. Our interpretation of nematic ordering is further supported by

our visual observations of birefringence only for this phase located immediately above the sediment phase.

At present, we do not know how the plates' diameters scale with thickness, so it is not clear whether a change in particle anisotropy plays a role here. To address this and other questions in the present tantalizingly incomplete phase diagram, a high-resolution study of the ($HK0$) peaks is planned, in combination with further crystallographic, small angle scattering (a SAXS study was recently performed by us at ESRF, and detailed analysis of these experiments is underway), and microscopy studies.

We have studied gravity-dispersed phases in suspensions of the synthetic clay Na fluorohectorite in aqueous solutions of 10^{-4}–10^{-2} M NaCl. Two distinct anisotropic gel regions have been identified. One is a nematic gel in which most particles are aligned vertically, and the resulting orientational anisotropy is uniform throughout the whole extent of the layer. The second gel is characterized by a small and nonuniform anisotropy in particle orientation, suggesting the presence of smaller aligned domains. Our present synchrotron experiments are discussed extensively in [8]. Further investigations of the system and the particle morphology are underway.

5. Acknowledgments

We acknowledge the Norwegian Research Council (NFR) for financial support under projects numbers 148865/432, 152426/431 and SUP 154059/420. The CMC beamline is supported in part by the USDOE Office of Basic Energy Sciences and NSF-DMR. The Advanced Photon Source is supported under USDOE Contract No. W-31-109-Eng-38. Preliminary studies performed at beamline X22A at the National Synchrotron Light Source were supported under USDOE Contract No. DE-AC02-98CH10886. E. DiMasi appreciate discussions with B. Noheda and T. Vogt at Brookhaven National Laboratory.

References

[1] Velde B. Introduction to clay minerals. London: Chapman and Hall; 1998.
[2] van Olphen H. An introduction to clay colloid chemistry. New York: Interscience; 1977.
[3] Fossum JO. Physica A 1999;270:270.
[4] Fossum JO. Soft condensed matter: configurations, dynamics and functionality. In: Skjeltorp AT, Edwards SF, editors. NATO Advanced Study Institute Series C Mathematical and Physical Sciences, vol. 552. Dordrecht (The Netherlands): Kluwer Academic Publications; 2000, p. 269.
[5] Gabriel J-CP, Sanchez C, Davidson P. J Phys Chem 1996;100:11139.
[6] Mourchid A, Levitz P. Phys Rev E 1998;57(5):R4887–90.
[7] Ramsay JDF, Lindner P. J Chem Soc Faraday Trans 1993;89:4207.
[8] DiMasi E, Fossum JO, Gog T, Venkataraman C. Phys Rev E 2001;64:61704.
[9] Lemaire BJ, Panine P, Gabriel J-CP, Davidson P. Europhys Lett 2002;59:55.
[10] Solin SA. In: Bernier P, et al., editors. Chemical physics of intercalation II. New York: Plenum Press; 1993.
[11] Mourchid A, Lecolier E, van Damme H, Levitz P. Langmuir 1998;14:4718.
[12] Dijkstra M, Hansen J-P, Madden PA. Phys Rev E 1997;55:3044.
[13] Onsager L. Ann NY Acad Sci 1949;51:627.
[14] van der Kooij FM, Kassapidou K, Lekkerkerker HNW. Nature 2000;406:868.
[15] Gabriel J-CP, Camerel F, Lemaire BJ, Desvaux H, Davidson P, Batall P. Nature 2001;413:504.
[16] Eppenga R, Frenkel D. Mol Phys 1984;52:1303.

[17] Mourchid A, Delville A, Lambard J, Lecolier E, Levitz P. Langmuir 1995;11:1942.
[18] Bates MA. J Chem Phys 1999;111:1732.
[19] Bates MA, Frenkel D. J Chem Phys 1999;110:6553.
[20] van der Kooij FM, Philipse AP, Dhont JKG. Langmuir 2000;16:5317.
[21] Andersen VJ, Lekkerkerker HNW. Nature 2002;416(6883):811.
[22] Kaviratna PD, Pinnavaia TJ, Schroeder PA. J Phys Chem Solids 1996;57:1897.
[23] da Silva GJ, Fossum JO, Di Masi E, Maloy KJ, Lutnaes SB. Phys Rev E 2002;66(1):011303.
[24] da Silva GJ, Fossum JO, Di Masi E, Maloy KJ. Phys Rev B 2003;67(9):094114.

Paper 2

N. I. RINGDAL, J. O. FOSSUM, D. M. FONSECA AND A. GMIRA

Birefringent Textures in the Nematic Phase of Na-Fluorohectorite Synthetic Clay

to be submitted to Langmuir beginning of May 2008

Birefringent Textures in the Nematic Phase of Na-Fluorohectorite Synthetic Clay

N.I. Ringdal, J.O. Fossum, D.M. Fonseca, A. Gmira*

Department of Physics, Norwegian University of Science and Technology, Hoegskoleringen 5, N-7491, Trondheim, Norway.

*jon.fossum@ntnu.no

We have studied stable strata of gravity-induced phase separation in ionic NaCl suspensions of synthetic Na-Fluorohectorite clay. We have observed how the strata depend on clay concentration as well as on salt NaCl contents of the suspension. The mass distribution and density variation at the isotropic – nematic interface indicate that existing models, and assumptions in existing simulations do not account for the present behavior. We suggest that this could be due to the polydispersity and/or the irregular shape of our Na-Fluorohectorite particles, as well as due to the double layer effects, which could result in a competition between, nematic ordering and gelation, in our system. The dependence on ionic NaCl strength display three main visual regimes irrespective of clay concentration. At low ionic strength (~10^{-4} M – ~5×10^{-3} M) the Debye screening length is longer than the van der Waals force range. In this regime, the particles repel each other electrostatically, and entropy driven Onsager type nematic ordering may occur, although gelation effects may also play a role. For ionic strengths above about 5×10^{-3} M, we believe that the van der Waals force come into play, that particles attract each other locally according to the DLVO model, resulting in a regime of small-domain attractive nematic like ordering. In the third regime, for ionic strengths above ~10^{-2} M, the clay particles aggregate into bigger assemblies, due to the dominant van der Waals force, and thus the observed birefringency is reduced. We have studied the nematic phase in detail in between crossed polarizers, and we have found textures showing nematic Schlieren patterns and by rotating polarizers as well as samples, and we have observed examples of disclinations of strengths –1 and –1/2. These patters can be observed directly by eye, reflecting the large size of the Na-fluorohectorite particles, and thus large domain sizes in this system.

KEYWORDS: Nematics, Clays, Birefringence, Schlieren Patterns, Disclination Defects.

1. Introduction

The formation of liquid-crystalline order in colloidal dispersions of anisotropic mineral nanoparticles has recently seen an increased research activity [1–3]. From the early investigations of vanadium pentoxide (V_2O_2) [4] and tobacco mosaic virus (TMV) [5,6], suspensions of various rod-like nanoparticles [7] are found to exhibit a spontaneous transition from an isotropic (I) phase to a nematic (N) phase in good agreement with statistical mechanical theories. In the 1940s, Lars Onsager [8] modeled this phase transition considering the competition between the entropy of confinement (favoring orientational randomness) and the entropy of excluded volume (favoring nematic alignment) of the colloidal system, thus concluding that at a sufficiently high enough particle concentration, the packing (excluded volume) entropy dominates and it becomes favorable for the particles to order in nematic alignment. Onsager showed that interaction between the particles is not necessary for orientational ordering, but the shape anisotropy of the particles alone is enough to drive the I-N phase transition. As Onsager proposed, and as later confirmed by computer simulations [9,10], nematic ordering can occur for plate-like particles that are fairly anisometric. This possibility was first studied experimentally by Langmuir in 1938 [11], who reported observations of an I-N phase transition in sols of natural clay particles, although conclusive evidence for a true thermodynamically stable I-N transition was lacking.

An obstacle against using clay as model to study nematic ordering of colloidal system is the clays tendency to gel when dispersed in solution. The gel structure and its formation, which are responsible for many of the clays practical applications, have from the 30–50s [12–16] until today

been substantially studied [17–37]. A transition from a sol to a gel may take place at very low clay concentrations. In recent years, the presence of orientational order in clay gels have been documented by optical measurements [18,38] showing visual nematic textures. Neutron- [39–41] and x–ray- scattering [42–45] as well as Magnetic Resonance Imaging (MRI) experiments [46–51] have all revealed structural correlations with nematic order. Since the gel phase may not be at thermodynamic equilibrium, the nematic ordering in the gels cannot be explained by the Onsager theory alone.

There is today no theory for the process of orientational ordering in the gel structure. There has been suggestions that the sol-gel transition may be directly related to the I-N transition [17,18,52,53], but this possibility has been contradicted in experiments by Michot et al. [32]. They showed that the concentration for the sol-gel transition of suspensions of size selected Wyoming Na-montmorillonite increases linearly with particle anisotropy. This is opposite to what could be expected for the corresponding evolution of the I-N transition, since large aspect ratio for the particles shifts the I-N transition towards lower volume fractions. Other studies concerning systems of charged colloidal platelets as Mg_2Al LDH [54] and gibbsite [55,56] also suggest that the liquid crystal phase transition, and gelation, are separate and even could be competitive processes. In these last two systems, the I-N phase transition has been observed to take place at a lower concentration than the sol-gel transition [54,57,58]. The thermodynamic stability of the nematic ordering could therefore be achieved and further compared to the Onsager model. For clay platelets, an I-N transition, was recently obtained in suspensions of natural nontronite [59,60]. Experimental systems of colloidal clay suspensions should be expected to differ from the Onsager model, since factors like particle morphology, electrostatic and van der Waals forces [61], gravitational force [62–64] and Brownian motion [65,66] may be of importance to the phase behavior.

In the present manuscript, we describe the phase behavior the synthetic 2:1 phyllosilicate (smectite) clay Na-fluorohectorite (NaFHT) suspended in aqueous NaCl solutions of concentrations ranging from 10^{-4} M to 10^{-2} M. In the gravitational field, a suspension of NaFHT may be effectively separated into different strata of gels, sols and sediments. In one of the phases, particle orientation of nematic order is found as evidenced by previous x-ray scattering [32,43,67] and MRI [51] studies.

Here, we present the birefringent nature of the nematic ordering, the role of different salt concentration and study how the clay concentration varies in the gravity dispersed suspension. We also report on observations of topological defects in the nematic phase. It is known that many of the topological defects which are commonly present in molecular liquid crystals, may also form in mineral liquid crystals. Schlieren textures and different disclinations have been observed in nematic clay gels of bentonite and laponite [38] and in the nematic phase of other systems of nanoplatelets [58,67,75], similar to our present observations.

2. Experimental details

2.1 Materials

Synthetic fluorohectorite clay was purchased in powder from Corning Inc., New York. The chemical formula of NaFHT is $Na_{0.6}Mg_{2.4}Li_{0.6}Si_4O_{10}F_2$, for which two inverted silicate tetrahedral layers share their apical oxygens with one octahedral layer. As shown in Figure 1, the individual NaFHT particles are composed of around 80–100 silicate lamellae [43] that stack by sharing Na^+ ions between their basal plane. Each 2:1 silicate lamellae is around 1 nm thick, with a charge of 1.2 e^-/unit cell (Si_8O_{20}). This charge is relatively large compared to other smectite clays, such as synthetic laponite (0.4 e^-/unit cell) and natural montmorillonite (0.6 e^-/unit cell) [68]. The large surface charge makes the particle stacks remain intact when suspended in water, in contrast to laponite and montmorillonite [42]. From AFM imaging (Figure 1), the polydispersity in particle size is quite large with highly variable particle morphology. The effective diameter of the platelets can vary from a few hundred nanometer up to about 20 microns [68].

70 g of fluorohectorite as purchased from Corning Inc. was added to 1000 ml distilled and deionized water, where it was dissolved and stirred by shaking for 2 days using an incubator at 300 rpm. Sodium ions were added as 60 g NaCl, which corresponds to about 10 times the known surface

charge per unit cell. The suspension was further shaken at 300 rpm for 2 weeks. Cl^- ions were removed by dialysis process, where the Cl^- content was checked regularly using a standard silver nitrate procedure. NaFHT powder was obtained by drying the resultant solution at 105 C° for about 3 days. A mortar with pestle was used before the NaFHT powder was further pulverized using a milling machine (IKA A11 basic).

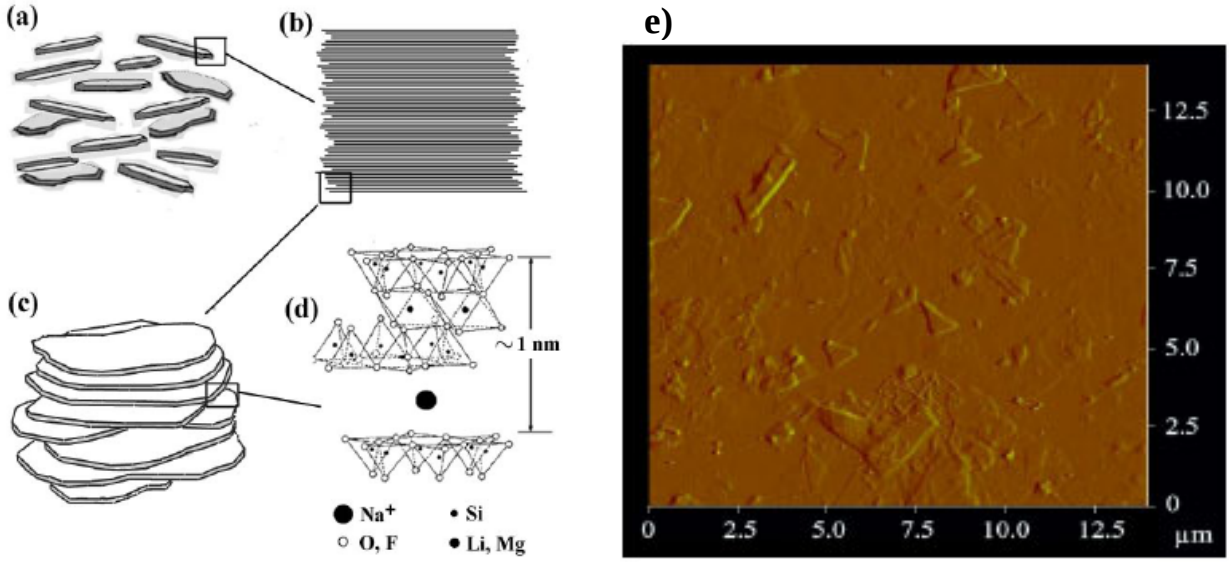

Figure 1. (a) Representation of Na-Fluorohectorite particles in nematic order. (b) Cross-section of a single clay particle, which consists of about 100 crystallized stacked lamellae. (c) The micron scale lamellas are layered with a thickness of around 1 nm. (d) Generic structure of the fluorohectorite, where the intercalated cation is Na+ for NaFHT. (e) Atomic Force Microscope (AFM) image of Na-fluorohectorite particles extracted from the nematic phase and deposited on a freshly cleaved mica surface.

Three different batches of NaFHT were studied in the present experiments, we call them B1, B2 and B3 respectively. All three batches were prepared as described above. Due to some differences in the time sequences spent at the different preparation steps, and due to differences in crushing and milling procedures, there may be differences between the particle sizes of the three batches, so that the particles of batch B1 and B2 are similar, whereas the B3 particles are expected to be smaller than both B1 and B2 type particles.

2.2 Experimental Methods

Two kinds of rectangular sample tubes were used for optical studies of the phase behavior of the suspensions: Vitrotube 4410-100 from VitroCom, is 10 cm long, 1 cm wide and 1 mm thick, a cell made of polyoxymethylene plastic (POM) and micro glass slides have inner dimensions 24×60×1 mm. This cell has glass walls of thickness 0.2 mm. Cylindrically shaped thin walled capillary tubes were also used in some of the studies: Hilgenberg Mark-tubes, of 2mm, and 1 mm respectively. The sample cells used are shown in Figure 2, and in Figure 3, we show the experimental setup used for the reported experiments, thus studying phase behavior of the samples, carefully observed by means of crossed polarizers and a PC-controlled camera.

3. Results

3.1 Clay Concentration

In Figure 4, we show suspended B1 samples with NaFHT concentrations of 0.5, 1, 2, 3, 4, 5 or 6 weight% clay respectively and at 10^{-3} M NaCl. The image in Figure 4 is typical for our investigated samples. For all investigated of powder types or ionic strengths, the phase behavior is very much similar for the different clay concentrations, although subtle differences may be observed:

The main difference between different batch powders (B1, B2, B3) is in the height level and in relative fraction of the separated phases in the sample tubes. For the samples with the lowest clay concentration, the relative amount of birefringence is in general lower for the same induced phase than for those of higher concentration.

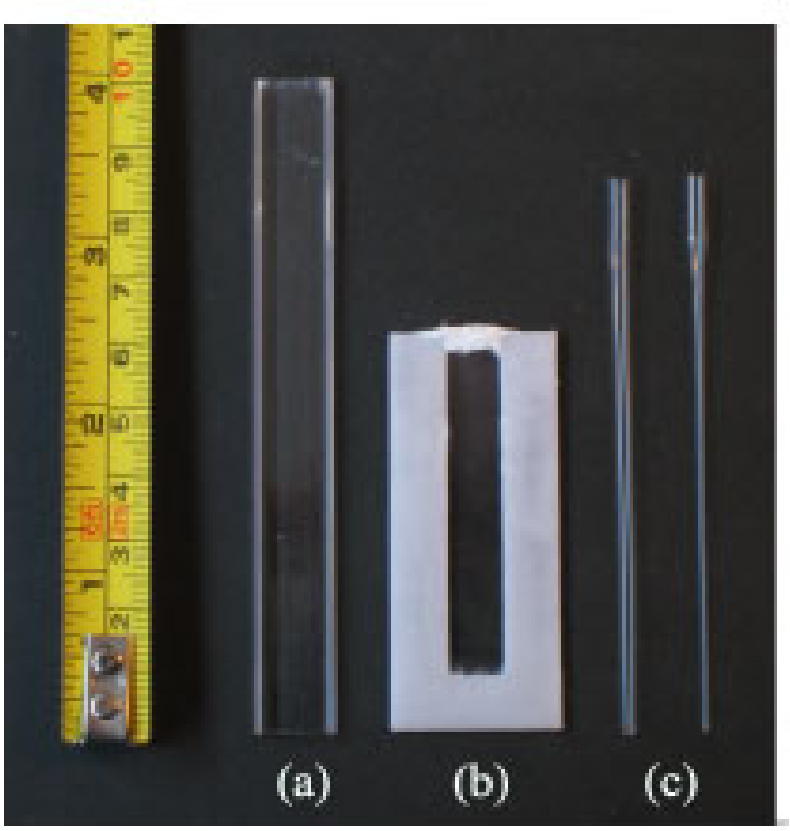

Figure 2. The different sample tubes used in the experiments. (a) Vitrotube 4410-100 from VitroCom (b) Rectangular cell 0 made from POM plastic and microscope slide covers (c) Hilgenberg Mark-tubes, left: 2mm, right: 1 mm.

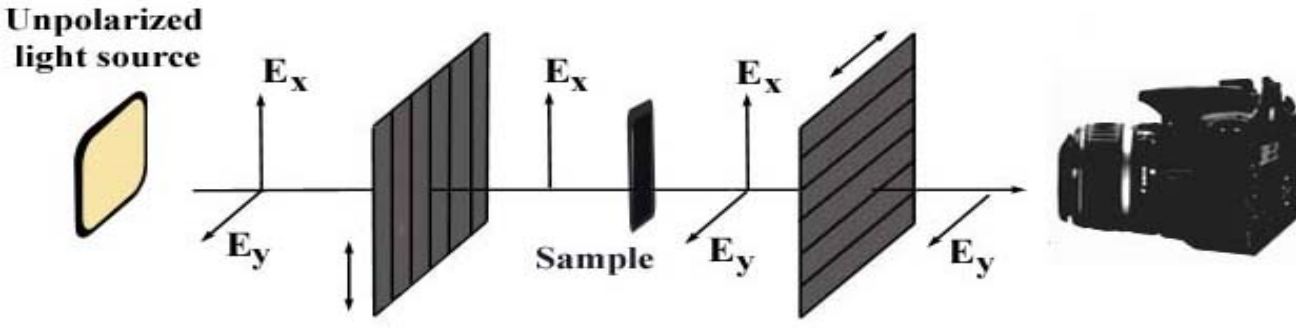

Figure 3. Our simple experimental setup for studying the long time sedimentation and phase behavior of the samples, carefully measured by crossed polarizers and a PC-controlled camera.

The contribution of the sediment to the sample height increases as expected when the clay concentration is increased. Above the sediment, a density profile is observed including formation of an interface between a nematically ordered (birefringent) region and an isotropic region. This is common to all of the samples in this concentration range.

At 6% w/w, the sample does not separate into different regions similar to the other samples, however, some birefringence is observed for this sample as well.

For the 2% w/w sample, the birefringent (nematic) region can be divided into two regions with an upper part being more birefringent than the lower part.

Figure 5 is a graphical representation of Figure 4.

In Figure 6, we show an example of a sample prepared in a capillary tube, and the corresponding SAXS patterns at different heights in the tube, showing anisotropies as previously observed by us in other NaFHT samples [32,43,67]. We see that in the nematic part of the samples, the long axis of the SAXS pattern is horizontal, i.e. indicating that the platelet thickness, i.e. the nematic director, is also horizontal.

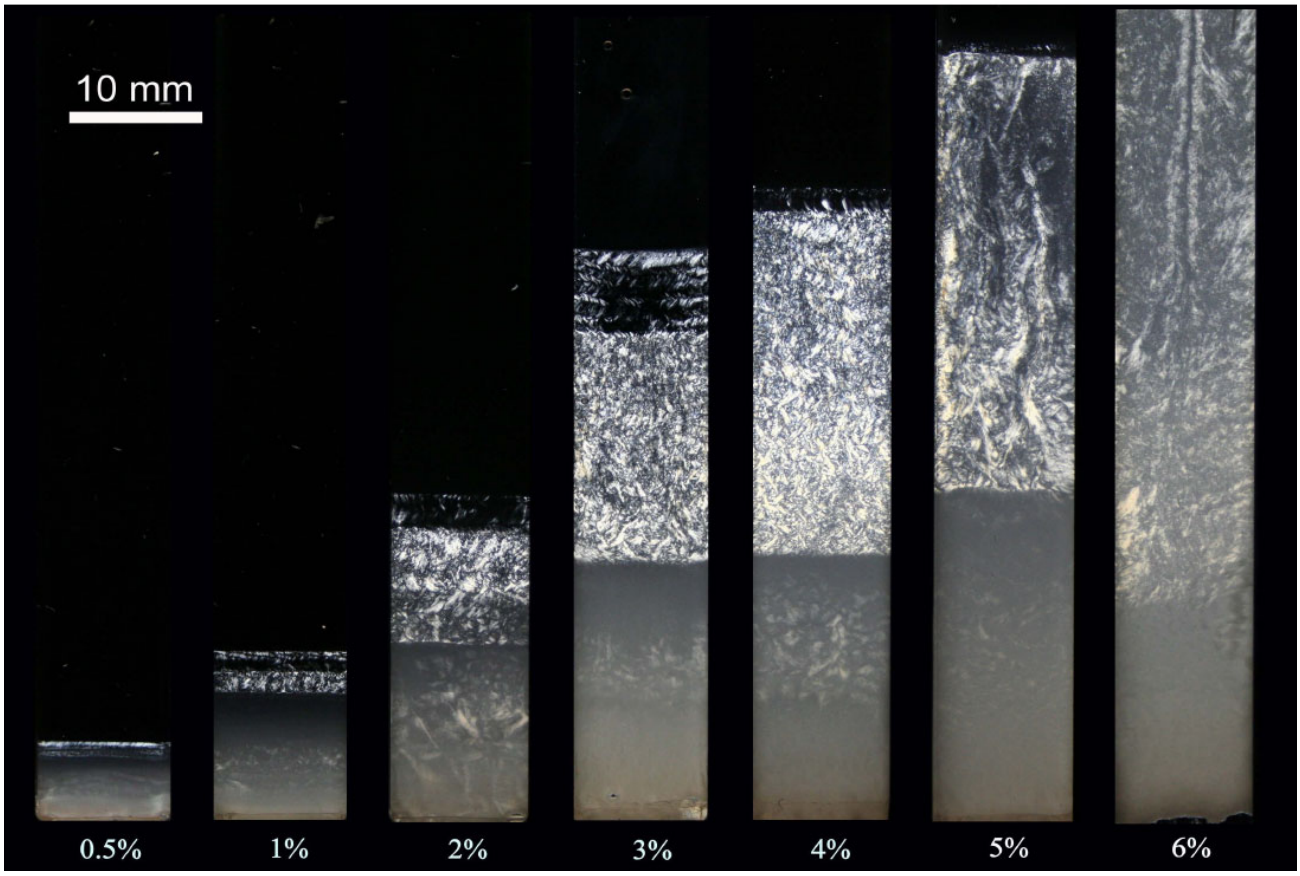

Figure 4. Suspended B1 samples with Na-fluorohectorite concentrations of 0.5, 1, 2, 3, 4, 5 and 6 weight% clay respectively, and all at 10^{-3} M NaCl. The time after preparation for the photographs are 1 months for 0.5 %, 2.5 months for 1%, 3 months for 3% and 5%, 4 months for 6% and 4.5 months for 2% and 4%. The picture of the 3% sample represents the stabilized settling state, where no further dynamics or changes of the phases are observed. The sample therefore looks the same after 4.5 months, and can be directly compared to the 2% and 4% samples.

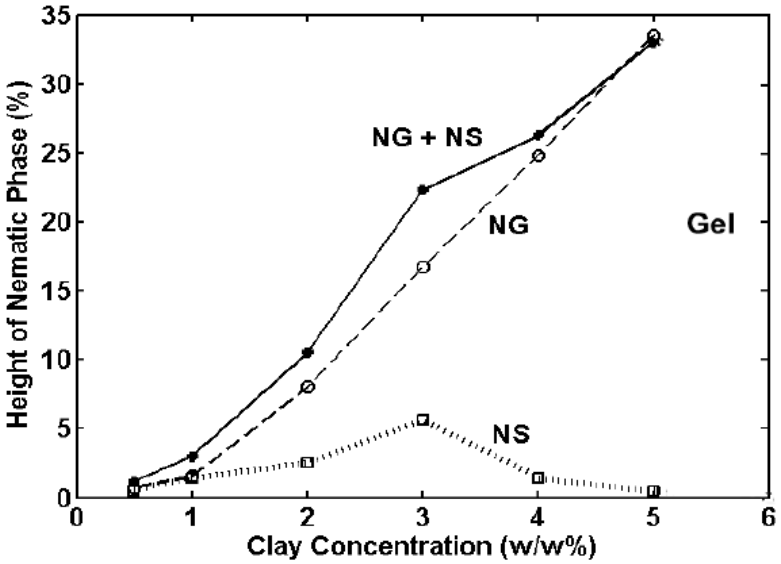

Figure 5. The height (volume) fraction of the nematic phase of the B1 powder at ionic strength 10^{-3} M NaCl as the clay concentration is increased from 0.5% to 4% w/w. The top height of the sample is almost 10 cm, and the fraction % is equal to the relative height of the nematic phase in centimeters

3.2 Mass Distribution

In order to map out density differences between the various phases, and how much the density varies within each phase, the clay concentration was measured for two similar samples of 3% w/w B2 and B3 type samples respectively, both at 10^{-3} M NaCl, from the liquid at the top to the sediment at the bottom. Samples were made in 5 containers of 50 ml each, all with height 7.5 cm and diameter 2.9 cm. The samples were left to settle for 2 months (B2) and 2.5 months (B3) respectively, before the measurements. At this time the samples had separated into different static strata from top to bottom. The measurements were carried out by pipetting out 250 microlitres at a time by inserting the pipette from the top of the container. In total; 177 sampled measurements were done for the M3 sample and 163 sampled measurements for the M2 sample. Since it turned out to be difficult to pipette out the sediment part, the remaining sediment at the bottom of each sample was dried and weighed to be 0.285 gram for the M3 sample (8.5 mm) and 0.561 gram for the M2 sample (14 mm).

Figure 7 shows the clay concentration as function of relative height, where zero is chosen at the edge of the nematic phase for both samples. The volume fraction is found by dividing the clay concentration by the mass density of NaFHT, which is 2.0 g/cm3 where it is taken into account that two water layers are intercalated in between the clay platelets [69].

3.3 Salt Concentration

The salt concentration is known to play a major role of the phase behavior of the aqueous Na-fluorohectorite solutions [42,43], because of the particles surface charge. Figure 8 shows a series of 3% w/w B1samples with an increasing salt concentration from 10^{-4} M to 5×10^{-2} M NaCl. Other examples, made from other powder batches, all show the same trend, irrespective of powder type and clay concentration. At low salt concentrations, the phase separation is the same with the formation of nematic phases between an isotropic gel and an upper dilute isotropic sol. As the ionic strength is increased, the relative height of nematic phase decreases along with an increase of the upper isotropic sol. In general, the relative height of the isotropic gel also clearly decreases with ionic strength from 10^{-4} M to 10^{-3} M NaCl. For the B1 powder in Figure 8, this is not as pronounced as for other batches, where just a very slight decrease can be seen over the same salt concentration range. As the ionic strength is further increased, the height of the isotropic gel and the nematic phase suddenly displays a larger drop when the salt concentration is increased from 2.5×10^{-3} M to 5×10^{-3} M NaCl. A further increase to 7.5×10^{-3} M NaCl makes very little change to any of these heights, but the next increase to 1×10^{-2} M NaCl shows a new pronounced drop for both the nematic and the isotropic gel. Above 1×10^{-2} M NaCl, there seems to be a gravity settled equilibrium distribution of particles in the whole container.

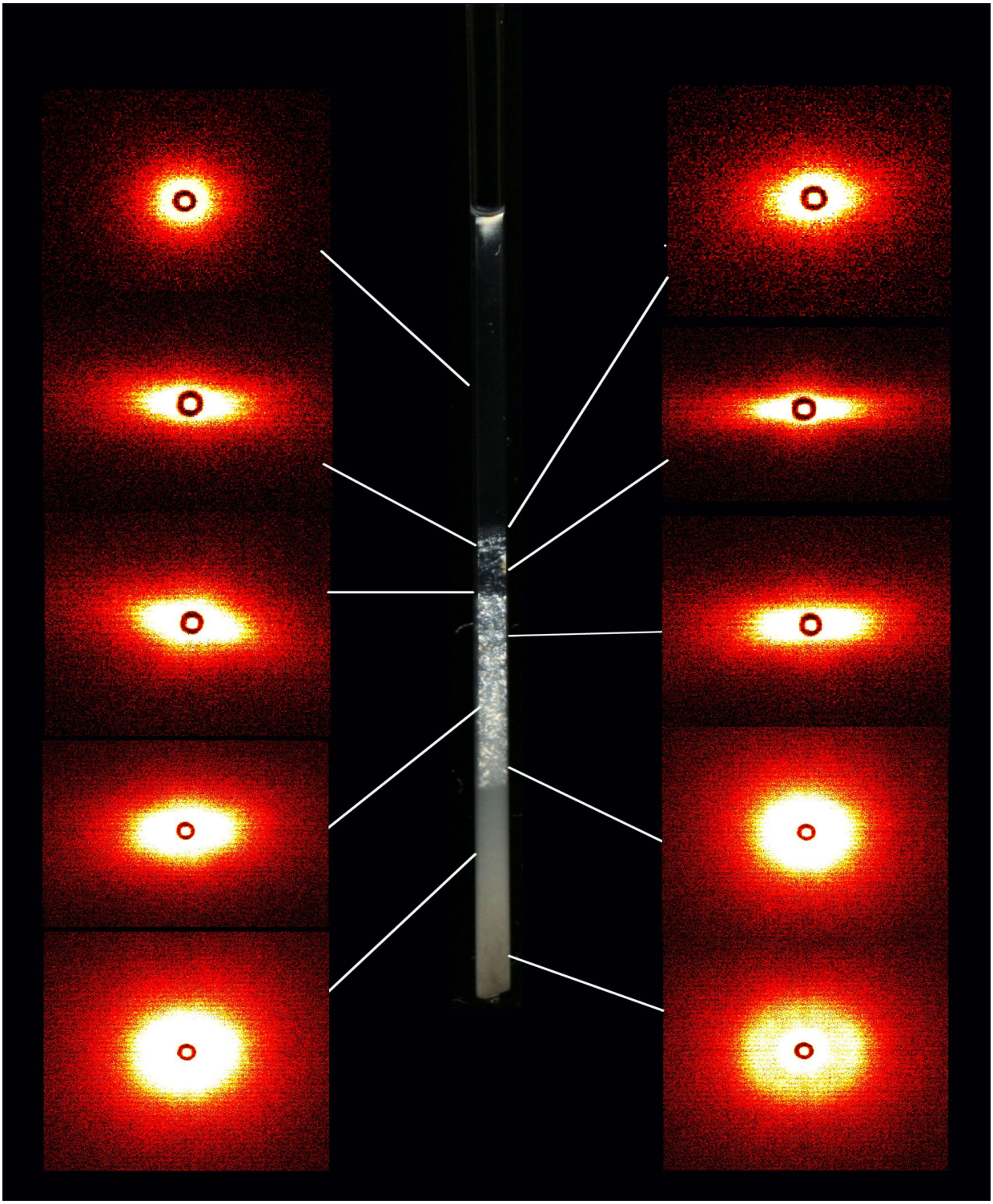

Figure 6. Example of a sample prepared in a capillary tube, and the corresponding SAXS patterns at different heights in the tube, showing anisotropies as previously observed by us in other NaFHT samples [32,43,67]. We see that in the nematic part of the samples, the long axis of the SAXS pattern is horizontal, i.e. indicating that the platelet thickness, i.e. the nematic director, is also horizontal. The SAXS data were obtained on a commercial Bruker Nanostar SAXS instrument with a rotating anode x-ray source (Cu Kα radiation at ~1.54 Å wavelength), and recording using a multiwire detector placed about 1.06 meters from the sample.

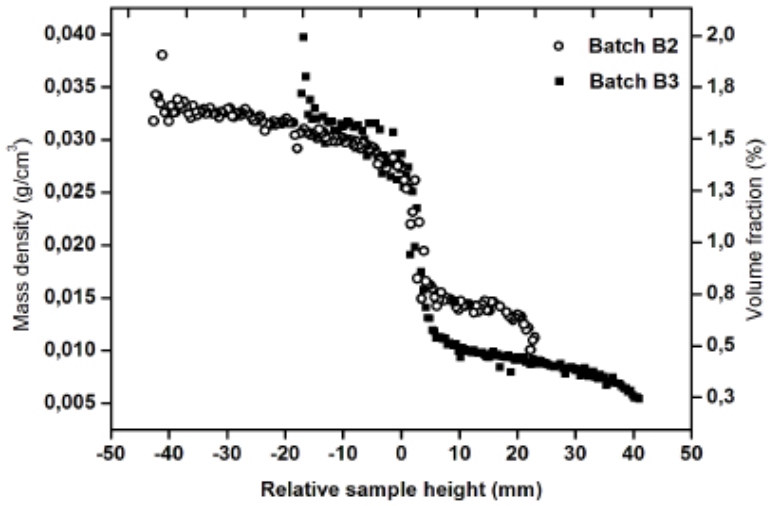

Figure 7. Clay concentration as function of relative sample height for a 3% B3 sample at 10^{-3} M NaCl and for a 3% B2 also at 10^{-3} M NaCl. We have chosen a (zero) reference point at right above the sediment, where the density is about 0.2 g/cm^3.

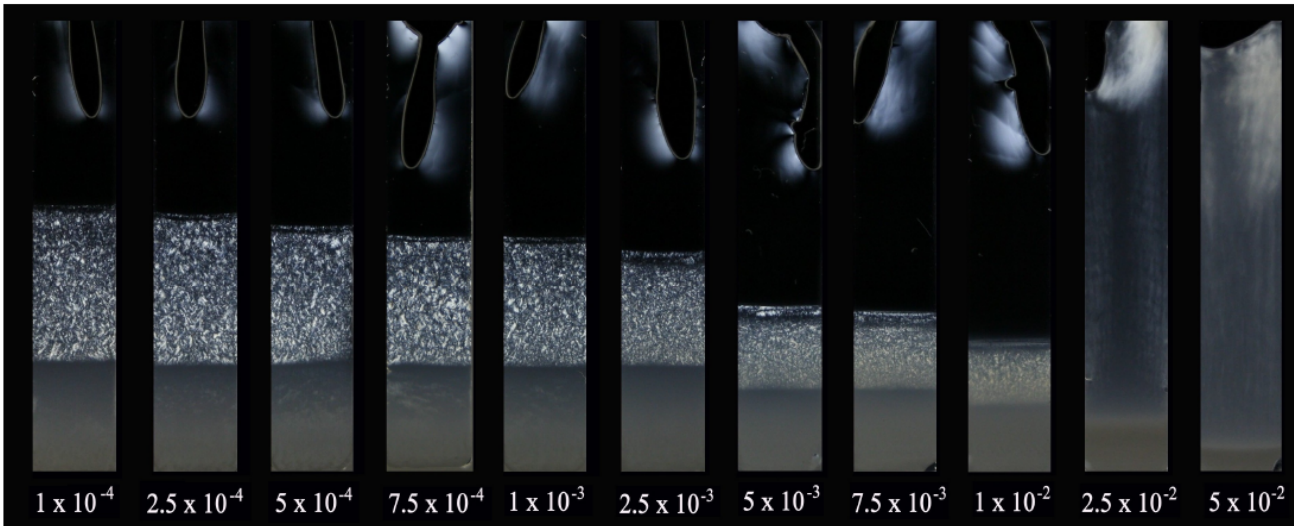

Figure 8. 3% w/w B1 samples at NaCl salt concentration ranging from 10^{-4} M to 2.5×10^{-2} M. The samples are prepared in cells of the type shown in Figure 2, where the formations at the top part are due to artificial sample damage. For each salt concentration; the picture to the right is with the samples placed in between crossed polarizers, while the picture to the left is without polarizers. The relative height of the nematic phase decreases with ionic strength as the electrostatic interaction is more effectively screened. The transition between the repulsive and attractive forces happens at an ionic strength between 10^{-2} M and 2.5×10^{-2} M. The images shown here are typical and reproducible in between samples prepared from different powder batches.

4. Discussion

4.1 Discussion of Mass Distribution

The concentration step between the clay concentration at the nematic and isotropic phase is slightly different for the B2 and B3 based suspensions investigated for this purpose as described in Section 3.1 above: The clay densities at the phase boundaries the B2 sample is about 0.031 g/cm^3 for the nematic phase and 0.010 g/cm^3 at the isotropic phase. For the B3 sample it is 0.029 g/cm^3 and 0.015 g/cm^3 at the nematic and isotropic phase respectively. This difference between the two batches may possibly be explained by that the fact that the B3 batch has been more finely crushed and therefore might have a lower polydispersity.

Because of sedimentation and gelation it is not possible to obtain samples where isotropic or nematic phase constitute the whole volume of the sample. Figure 5 shows that the relative amount of the nematic gel increases linearly from 1% to 5% w/w before gelation takes place at about 6% w/w.

Such a linear increase is similar to other systems reported in the literature, such as gibbsite [58] and nontronite [59,60], when the volume fraction is gradually increased in those systems. Those systems have been reported to display a true thermodynamic isotropic-nematic phase transition, where attractive forces are not believed to interfere with the nematic ordering.

For gibbsite and nontronite, experimental values for the densities of the coexisting isotropic and nematic phases are in reasonable agreement with theoretical computer simulations [70] (for infinitely thin platelets), for which dimensionless number densities, i.e. the number density n = N/V multiplied by the diameter D cubed, at zero polydispersity are found to be $n_{iso}D^3 \sim 3.7$ and $n_{nem}D^3 \sim 4.0$. These simulations [70] were done for infinitely thin platelets, but it has also been found that platelets with a finite thickness do not give any major difference $n_{iso}D^3 \sim 3.8$ and $n_{nem}D^3 \sim 3.9$ when the diameter to thickness ratio is 10 [71]. If the polydispersity is 25%, which could well be the case for our system, the densities are found to be $n_{iso}D^3 \sim 3.5$ and $n_{nem}D^3 \sim 5.0$ respectively [70].

Since the sedimentation process in our NaFHT suspensions may fractionate the particles, the size (or shape) of the particles in the isotropic phase may be different from the particles in the nematic phase. The values in Figure 7 for the volume fractions at the isotropic and nematic phase might still be used to give an estimate for number densities to compare to theoretical and other experimental [55,57] results. The relation between volume fraction ϕ and nD^3 is for circular platelets of diameter D and thickness t is [57]:

$$\phi = n\pi D^2 t/4 = (\pi/4)(t/D)(nD^3) \qquad (1)$$

When polydispersity in taken into account, Equation (1) is replaced by [57]:

$$\phi = (\pi/4)(\langle t\rangle/\langle D\rangle)(n\langle D^3\rangle)(1-\sigma_D^2)/(1+3\sigma_D^2) \qquad (2)$$

where σ_D is the standard deviation representing the polydispersity of the diameter, and $\langle\ \rangle$ denotes average [57]. Rewriting Equation (2) gives

$$n\langle D^3\rangle = \phi\,(4/\pi)(\langle D\rangle/\langle t\rangle)\,(1+3\sigma_D^2)/(1-\sigma_D^2) \qquad (3)$$

An exact value for the polydispersity of our suspensions of Na-fluorohectorite is not known, but AFM pictures (Figure 1) indicates that the polydispersity is quite high. To estimate quantities, the use of an approximated average particle diameter of 2 μm, which corresponds to a circle of same facial area, give the coexisting densities $n_{iso}D^3 \sim 0.4$ and $n_{nem}D^3 \sim 0.8$, when the polydispersity is chosen as high as possible and 100 nm is used for the thickness of the particles. The large difference between the isotropic and nematic densities may be indicative of large polydispersity. These estimated values are about a factor 10 smaller than predicted values of the cited computer simulations [57]. Since the NaFHT particles are highly anisometric, neither Equation (3) nor the cited simulations seem to represent our NaFHT system.

Computer simulations by Bates [72] have shown that the coexisting densities for the nematic-isotropic transition are dependent on the shape of the particles. Bates' study showed that the transition densities for triangular particles (which may be a better approximated shape for NaFHT than a round object), are almost one order of magnitude lower than particles of circular shape. The simulation data [72] do not account for lath-shape biaxial particles with large differences between the facial dimensions, something which is more representative of the present NaFHT particles.

It difficult to be estimate how much influence attractive and repulsive forces might have for the ordering of nematic and isotropic orientation in our suspensions. The high particle charge of the NaFHT particles means that they are not hard-body objects. Attempts to estimate effective diameter and effective thickness from the Debye screening length do not give better agreement with the predictive simulation data.

Also, the different NaFHT particles within the suspension may interact, separate and behave differently from each other depending on particle size. Particles of large size (3–10 μm) may form nematic ordering in coexistence with an isotropic embedding of smaller particles (< 1 μm).

4.3 Discussion of Salt Concentration effects

Since the theoretical understanding of the salt-induced ordering of charged colloidal particles of large particle size is not yet fully established, the phase behavior present in this section are qualitatively discussed within DLVO [61] and Onsager theories [8]. In the pictures of the samples without polarizers in Figure 8, there seems to be a density increase in all the phases which is

expected due to less repulsion as ionic strength increases. For any clay concentration or powder type, the NaFHT suspensions flocculate at a salt concentration of about 5×10^{-2} M, and for higher ionic strengths, the suspensions undergoes fast coagulation and very little sediments settle at the bottom.

In Figure 8, a flocculation transition is found to take place between an ionic strength of 1×10^{-2} M and 2.5×10^{-2} M NaCl. Such a flocculation transition is similar to data found for Wyoming montmorillonite, published by Abend and Lagaly [73], where the transition line shows a negative slope as the clay concentration is increased, which is also probably the case for NaFHT since slightly slower coagulation occur for the lowest clay concentration. Experiments carried out by Michot et al. [59] on sodium nontronite, also show a flocculation transition at ionic strength 10^{-2} M. However, the phase diagram of this clay type has a positive flocculation slope at low volume fractions, and thereafter displaying a negative sol-gel transition as the volume fraction is further increased.

Compared to other clay minerals, the flocculation transition for NaFHT is lower than for bentonite [38] and higher than for laponite [38]. The Debye screening length for the samples different NaCl concentrations is tabulated Israelachvili [61]. When these values are taken together with the total potential energy curve of the DLVO interaction, a secondary minimum at a screening length of 5 nm may correspond to the sudden behavior change that take place for the B1 suspensions at 2.5×10^{-3} M, thus this could indicate a transition form a repulsive Onsager type nematic at low ionic strengths to an attractive small domain nematic at higher ionic strengths, indicating the existence of a “local minimum in the DLVO model”. A flocculation transition at 2.5×10^{-2} M corresponds to a screening length of about 2 nm, for which the interaction is “completely taken over” by van der Waals attraction.

For salt concentrations from 10^{-4} M to 10^{-3} M, the Debye screening length decreases from about 30 to 10 nanometers. As the screening length is roughly proportional to the electric double layer, the particle dimensions effectively increase as the salt concentration is decreased. In aqueous salt solution, the effective particle thickness is roughly increased by two times the screening length. From the Onsager theory including the interplay between excluded volume entropy and orientational entropy, a change in the particle dimensions should reduce the critical concentration of particles at the isotropic-nematic transition. It is difficult to estimate how much influence this growth in effective particle size could have for the observations of the increased nematic ordering with decreasing ionic strength in the NaFHT suspensions. From simulation experiments by Rowan and Hansen [74], it is suggested that the swelling effect is negligible for large particles, and that the phase behavior may be explained solely on electrostatic grounds. In suspensions of very large NaFHT particles, the phase diagram could then be dominated by long-range electrostatics. However, the strong influence of polydispersity in the size of the NaFHT particles should play a role, since the smallest particles remain in the upper isotropic sol after gravity has been acting on the suspension, and the significance of the double layer expansion in particle size could have most influence for this phase.

The extra height of the nematic phase for low salt concentration may possibly be thought of being driven by repulsion alone.

4.4 Discussion of Schlieren Patterns, Textures and Defects

In a normal unaligned nematic phase the director usually points in different directions at different points within the sample. Since the regions where the director orients parallel, perpendicular or along the normal of the polarizer, appear dark, and all other directions appear bright when viewed between crossed polarizers, a nematic phase often consists of both bright and dark areas. In many nematic textures, the brightness often changes abruptly, which indicate that the director also changes abruptly at those places. It is impossible to define the direction of the director at the point of an abrupt change, so such a point represents a defect in the liquid crystalline order. Theoretically, these defects could be points, lines or sheets where the director discontinuously changes in passing through one of the defects. Point defects tend to occur in restricted geometries and at surfaces. For example, point defects sometimes occur in spherical droplets of liquid crystals, around droplets of isotropic liquid in a liquid crystal, and in thin capillary tubes [76]. Sheet defects tend to spread out

so that the change in orientational order is continuous over a slab containing the sheet rather than discontinuous at a set of two-dimensional points defining a sheet. Such structures are called walls.

Line defects are the most common in liquid crystals and have been given the special name disclination, i.e. a "discontinuity" in the "inclination" of the director. Viewed between crossed polarizers, disclinations are often visible as a characteristic pattern with dark branches converging at perpendicular angles. These dark branches are usually named brushes and the pattern is referred to as a Schlieren texture. Many different disclinations are possible, and they can be specified in terms of a description of the change in the director direction around the point where the director field is not defined. A mathematical description of this is done by defining a polar angle, ϕ, and the director direction, Ψ, in the director configuration in the plane perpendicular to the direction of the line:

$$\Psi = m\phi + \phi_0 = \pi/2 \qquad (4)$$

The parameter m is referred to as the strength of the disclination and equals a multiple of ±1/2. For negative strengths, the director rotates clockwise in traversing along the same counter-clockwise path of ϕ. For positive strengths the director rotates counter-clockwise. The strength is a measure of how much the director is rotated when ϕ is increased by 2ϕ. If the strength is ±1/2, the director rotates 180π for one full loop around the disclination point. For a disclination of strength ±1, the director rotates 360π for a similar full loop.

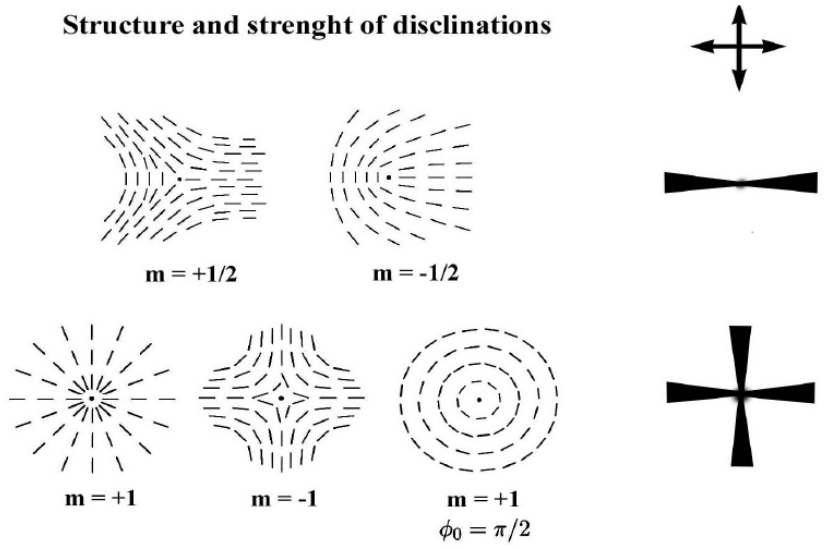

Figure 9. The structure and strengths of five disclinations as described by equation (4). The respective appearances of the structures when viewed between crossed-polarizers are shown to the right. Except for the last four-brush Schlieren structure, all cases have initial director direction $\phi_0 = 0$.

Figure 9 shows the director structure of different disclinations with various strengths and constant ϕ_0. The corresponding appearance of Schlieren brushes when the nematic distortion is also illustrated. These brushes appear black, since the director in these places is either parallel or perpendicular to one of the crossed polarizer axes. The rest of the liquid crystal is bright. Thus there will be two dark bands merging from opposite sides of disclinations of strength ±1/2, and four dark bands emanating from disclinations of strength ±1. The sign of the strength can be determined by a simultaneous rotation of the two polarizers. If they are rotated counter-clockwise, the dark bands will rotate clockwise for disclinations of negative strengths and counter-clockwise for disclinations of positive strengths. By combining the number of brushes with rotation of the crossed polarizers, the type of disclination can easily be identified.

In Figure 10, we show birefringence from a sample of 3% w/w B3 10^{-3} M NaCl at different angles of the crossed polarizers, including a disclination defect [76] with two brushes emanating from each other at 90°. In the first two pictures of the last row, the two more brushes may be seen. The brushes rotate in the same direction as the polarizers, and the strength can therefore be regarded as being +1. Arrow b shows a singularity where two dark brushes meet and rotate in the opposite direction with respect to the crossed polarizers. This corresponds to a disclination with strength –1/2. Arrow c marks the position of dark grooves located between birefringent stripes. The birefringent stripes

become dark when they are oriented along the polarizer or analyzer axes, but it is not possible to tell whether they are composed of clay particles connected edge-to-edge, face-to-face or for that matter face-to-edge. The black grooves do not seem to change in either brightness or position during rotation of the crossed polarizers. This is shown in Figure 10, but it is best observed when the pictures change by overlapping. From this it would be reasonable to imagine the black grooves correspond to regions of isotropic orientation, giving nematic-isotropic coexistence in almost every height of the settled suspension. Another possibility could be that there is homeotropic alignment in the black grooves and the particles crosswise of the stripes orient in a helical structure similar to chiral (cholesteric) nematic phases. A way to test this could be to rotate the sample and see if the black grooves moved either up or down, since that would change the optical position of the homeotropically aligned particles. Unfortunately this has shown to be not practical successful in our samples, since the increase in optical path length through our 1 mm thick samples tubes changes the appearance of the pattern too much.

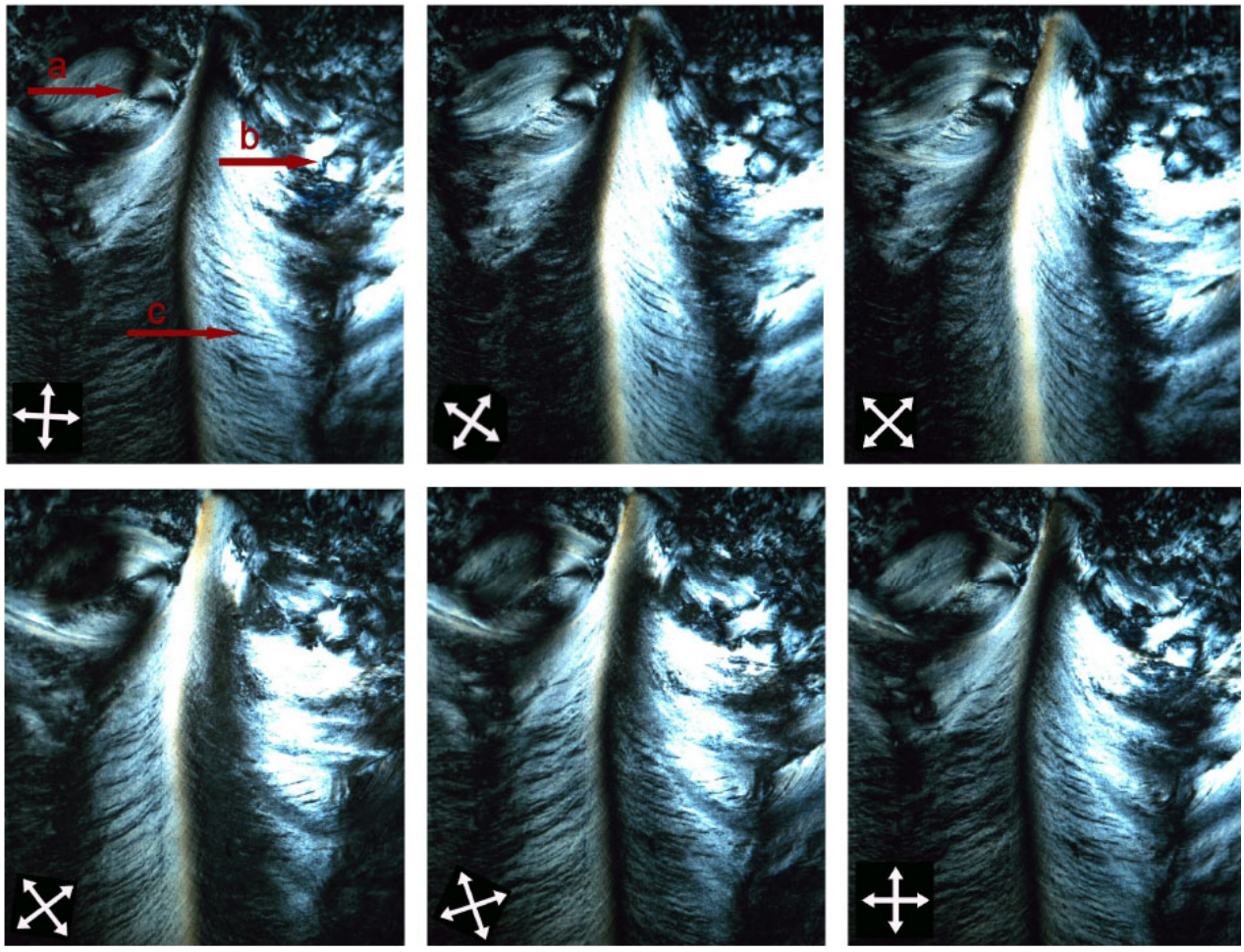

Figure 10. Observed birefringence from a sample of 3% w/w B3 10^{-3} M NaCl at different angles of the crossed polarizers. From the upper left to the lower right picture, the polarizers are rotated successively to 20 °, 45°, 55°, 75° and 90° with respect to the edges of the sample tube. Arrow **a** shows a disclination with two brushes emanating from each other at 90°. In the first two pictures of the last row, the two more brushes may be seen. The brushes rotate in the same direction as the polarizers, and the strength can therefore be regarded as being +1. Arrow **b** shows a singularity where two dark brushes meet and rotate in the opposite direction with respect to the crossed polarizers. This corresponds to the **a** disclination with strength –1/2. Arrow **c** marks the position of dark grooves located between birefringent stripes. As the polarizers are rotated, there are no apparent movements of the grooves.

In Figure 11, we show defects in the nematic region close to the isotropic phase for a sample which is filled with pre-settled suspension of 3% w/w B3 powder at 10^{-3} M NaCl. The pictures are

taken 8 months after the time of injection. Arrow a shows a disclination of strength –1, and arrow b shows a disclination of strength +1. For all the samples that display Schlieren patterns, disclination points are found with both two (strength 1/2) and four (strength 1) emanating brushes. The disclinations seem to appear most frequent in the upper part close to the isotropic phase. The strength of the disclinations is defined in section, where the sign is determined by rotation of the cross-polarizers. If the brushes rotate in the same way as the polarizers, the sign is positive. If they rotate in the opposite direction, the strength is negative. Figures 9 and 10 show disclinations of both strengths –1 and –1/2. The fact that such nematic Schlieren patterns are observed, using 1 mm thick sample tubes, reflects the large size of the Na-fluorohectorite particles.

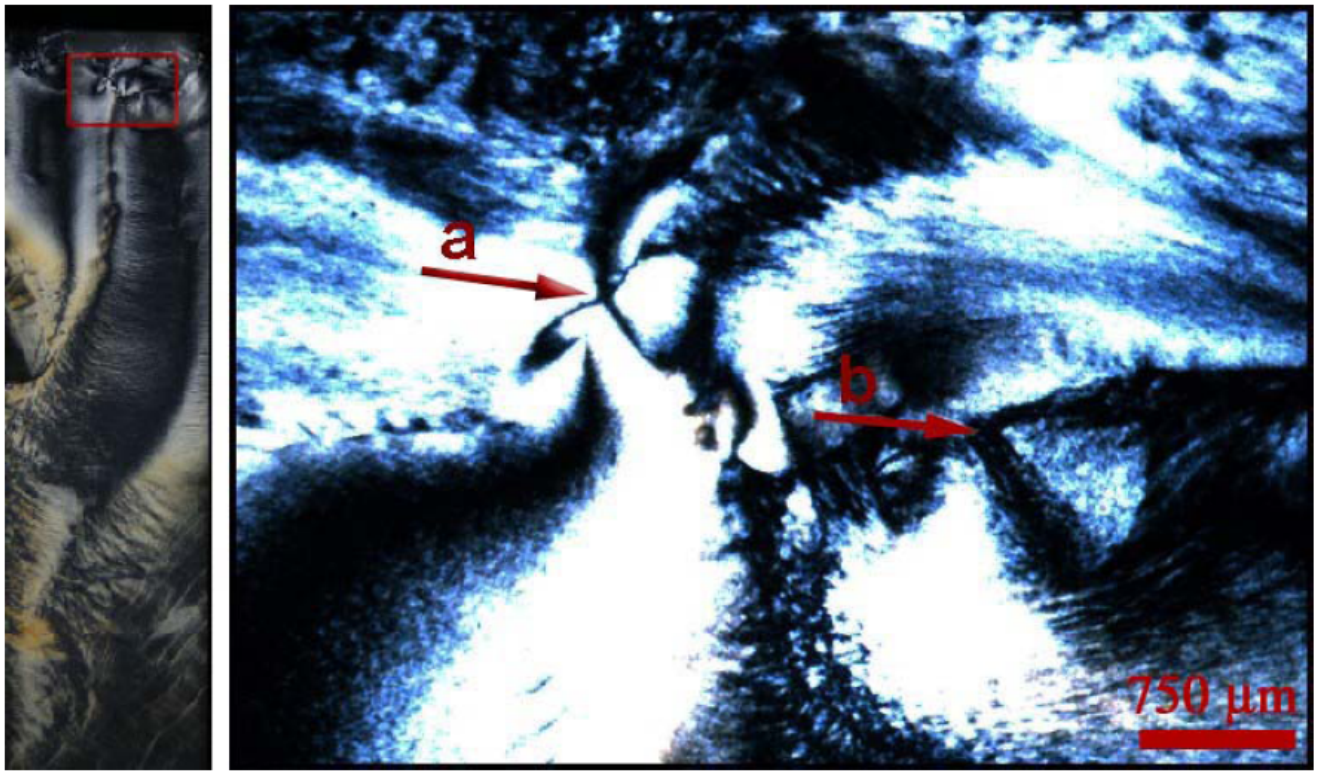

Figure 11. Defects in the nematic region close to the isotropic phase for a sample which is filled with pre-settled suspension of 3% w/w B3 powder at 10^{-3} M NaCl. The pictures are taken 8 months after the time of injection. Arrow **a** shows a disclination of strength –1, and arrow **b** shows a disclination of strength +1.

5. Conclusions

We have studied stable strata of gravity define phase separation in ionic NaCl suspensions of synthetic Na-Fluorohectorite clay. We have observed and reported how the strata depend on clay concentration as well as on salt NaCl contents of the suspension. The mass distribution in the isotropic and in the nematic phase, at the isotropic – nematic as well as the and the density variation at the isotropic – nematic interface indicate that existing models, and assumptions in existing simulations do not account for the present system behavior. We suggest that this could be due to the polydispersity as well as to the irregular shape of the present Na-Fluorohectorite particles, as well as to effects of the double layer, which could result in an overlap of, and even possibly a competition between, nematic ordering and gelation, in our system.

The dependence on ionic NaCl strength displays three main regimes irrespective of clay concentration. At low ionic strength (~10^{-4} M – ~5×10^{-3} M) the Debye screening length is longer than the van der Waals force range. In this regime, the particles repel each other electrostatically, and entropy driven nematic ordering, in the Onsager sense, may occur, although gelation effects may also play an integral role. One may thus use the term “repulsive nematic” for this regime. For ionic

strengths above about 5×10^{-3} M, we believe that the van der Waals force come into play, and that gelation is important, and we may use the term "attractive nematic" for this regime. For ionic strengths above ~10^{-2} M the clay particles form bigger assemblies, due to the dominant van der Waals force, and thus the nematic ordering is reduced.

We have studied the nematic phase in detail in between crossed polarizers, and we have found textures showing nematic Schlieren patterns and by rotating polarizers as well as samples, and we have seen examples of disclinations of strengths –1 and –1/2. These patters can be observed directly by eye, reflecting the large size of the Na-fluorohectorite particles, and thus domain sizes in this system.

Looking in detail at our images, we always spot a narrow nematic like regime just at the interface of the isotropic-nematic transition. This will be the subject of future studies, already underway, along with studies of the dynamics of this phase separation in gravity, also underway. We have previously shown that these phase are sensitive to magnetic fields [51], and this we will also study in more detail in the future both in terms of nematic textures and also by means of other techniques like x-ray scattering and MRI. Beyond our own expertise and capabilities, we also hope that the discrepancies we report between our density measurements, and existing models and simulations, could initiate theoretical or simulation work by other groups.

ACKNOWLEDGMENTS We acknowledge the Research Council of Norway for funding through the Nanomat and the Frinat Programs.

REFERENCES

[1] Sonin, A. S. J. Mater. Chem. **1998**, 8, 2557
[2] Gabriel, J. C. P.; Davidson, P. Top. Curr. Chem. **2003**, 226, 119
[3] Gabriel, J. C. P. ; Davidson, P. Curr. Opin. Colloid Interface Sci. **2005**, 9, 377
[4] Zocher, H. Z. Anorg. Allg. Chem **1925**, 147, 91
[5] Bawden, F. C., Pirie, N. W., Bernal, J. D., and Fankuchen, I. Nature **1936**, 138, 1051
[6] Bernal, J. D.; Fankuchen, I. J. Gen. Physiol. **1941**, 25, 111
[7] Zhang, Z. X.; van Duijneveldta, J. S. J. Chem. Phys. **2006**, 124, 154910
[8] Onsager, L. Ann. N. Y. Acad. Sci. **1949**, 51, 627
[9] Eppenga, R.; Frenkel, D. Mol. Phys. **1984**, 52, 1303
[10] Veerman, J. A. C.; Frenkel, D. Phys. Rev. A **1992**, 45, 5632
[11] Langmuir, I. J. Chem. Phys **1938**, 6, 873
[12] Olphen, H. V. Discuss. Faraday Soc. **1951**, 11, 82
[13] Broughton, G.; Squires, L. J. Phys. Chem. **1936**, 40, 1041
[14] Hauser, E. A.; Reed, C. E. J. Phys. Chem. **1937**, 41, 911
[15] Hauser, E. A. Chem. Rev. **1945**, 40, 287
[16] Norrish, K. Discuss. Faraday Soc. **1954**, 18, 120
[17] Mourchid, A.; Delville, A.; Lambard; J.; L'ecolier; E., Levitz, P. Langmuir **1995**, 11, 1942
[18] Mourchid, A.; L'ecolier; E., Damme, H. V.; Levitz, P. Langmuir **1998**, 14, 4718
[19] Pignon, F.; Piau, J. M.; Magnin, A. Phys. Rev. Lett. **1997**, 76, 4857
[20] Pignon, F.; Magnin, A.; Piau, J. M. Phys. Rev. Lett. **1997**, 79, 4689
[21] Bonn, D.; Tanaka, H.; Wegdam, G.; Kellay, H.; Meunier, J. Europhys. Lett. **1998**, 45, 52
[22] Bonn, D.; Kellay, H.; Tanaka, H.; Wegdam, G.; Meunier, J. Langmuir **1999**, 15, 7534
[23] Levitz, P.; L'ecolier, E.; Mourchid, A.; Delville, A.; Lyonnard, S. Europhys. Lett. **2000**, 49, 672
[24] Knaebel, A.; Bellour, M.; Munch, J.-P.; Viasnoff, V.; Lequeux, F.;Harden, J. L. Europhys. Lett. **2000**, 52, 73
[25] Tanaka, H.; Meunier, J.; Bonn, D. Phys. Rev. E 69 **2004**, 031404
[26] Tanaka, H.; Jabbari-Farouji, S.; Meunier, J.; Bonn, D. Phys. Rev. E **2005**, 71, 021402
[27] Strachan, D. R.; Kalur, G. C.; Raghavan, S. R. Phys. Rev. E **2006**, 73, 041509
[28] Ianni, F.; Leonardo, R. D.; Gentilini, S.; Ruocco, G. Phys. Rev. E **2007**, 75, 011408
[29] Bellon, L.; Gibert, M.; Hernandez, R. Eur. Phys. J. B **2007**, 55, 101
[30] Dijkstra, M.; Hansen, J. P.; Madden, P. A. Phys. Rev. Lett. **1995**, 75, 2236
[31] Kroon, M.; Wegdam, G. H.; Sprik, R. Phys. Rev. E **1996**, 54, 6541
[32] Michot, L. J.; Bihannic, I.; Porsch, K.; Maddi, S.; Baravian, C.; Mougel, J.; Levitz, P. Langmuir **2004**, 20, 10829
[33] Martin, C.; Pignon, F.; Piau, J.-M.; Magnin, A.; Lindner, P.; Cabane, B. Phys. Rev. E **2002**, 66, 021401

[34] Mongondry, P.; Tassin, J. F.; Nicolai, T. J. Colloid Interface Sci. **2005**, 283, 397
[35] Ruzicka, B.; Zulian, L.; Ruocco, G. Langmuir **2006**, 22, 1106
[36] Bihannic, I.; Michot, L. J.; Lartiges, B. S.; Vantelon, D.; Labille, J.; Thomas, F.; Susini, J.; Salome, M.; Fayard, B. Langmuir **2001**, 17, 4144
[37] Cousin, F.; Cabuil, V.; Levitz, P. Langmuir **2002**, 18, 1466
[38] Gabriel, J. C. P. ; Sanchez, C. ; Davidson, P. J. Phys. Chem. **1996**, 100, 11139
[39] Ramsay, J. D. F.; Lindner, P. J. Chem. Soc., Faraday Trans. **1993**, 89, 4207
[40] Ramsay, J. D. F.; Swanton, S. W.; Bunce, J. J. Chem. Soc. Faraday Trans. **1990**, 86, 3919
[41] Martin, C.; Pignon, F.; Magnin, A.; Meireles, M.; Leliere, V.; Lindner, P.; Cabane, B. Langmuir **2006**, 22, 4065
[42] DiMasi, E.; Fossum, J. O.; Gog, T.; Venkataraman, C. Phys. Rev. E **2001**, 64, 061704
[43] Fossum, J. O.; Gudding, E.; d. M. Fonseca, D.; Meheust, Y.; DiMasi, E.: Gog, T.; Venkataraman, C. Energy **2005**, 30, 873
[44] Lemaire, B. J.; Panine, P. ; Gabriel, J. C. P. ; Davidson, P. Europhys. Lett. **2002**, 59, 55
[45] Saunders, J. M.; Goodwin, J. W.; Richardson, R. M.; and Vincent, B. J. Phys. Chem. B **1999**, 103, 9211
[46] Porion, P.; Mukhtar, M. A.; Meyer, S.; Faugere, A. M.; van der Maarel, J. R. C.; Delville, A. J. Phys. Chem. B **2001**, 105, 10505
[47] Porion, P.; Mukhtar, M. A.; Faugere, A. M. ; Pellenq, R. J. M.; Meyer, S. ; Delville, A. J. Phys. Chem. B **2003**, 107, 4012
[48] Porion, P.; Rodts, S.; Al-Mukhtar, M.; Faugere, A. M.; Delville, A. Phys. Rev. Lett. **2001**, 87, 208302
[49] Porion, P.; Al-Mukhtar, M.; Faugere, A. M.; Delville, A. J. Phys. Chem. B **2004**,108, 10825
[50] Porion, P.; Faugere, A. M.; Delville, A. J. Phys. Chem. B **2005**, 109, 20145
[51] de Azevedo, E. N.; Engelsberg, M.; Fossum, J. O.; de Souza, R. E. Langmuir **2007**, 23, 5100
[52] Kroon, M.; Vos, W. L.; Wegdam, G. H. Phys. Rev. E **1998**, 57, 1962
[53] Bhatia, S., Barker, J., and Mourchid, A. Langmuir **2003**, 19, 532
[54] Zhang, J.; Luan, L.; Zhu, W.; Liu, S.; Sun, D. Langmuir **2007**, 23, 5331
[55] van der Beek, D.; Lekkerkerker, H. N. W. Europhys. Lett. **2003**, 61, 702
[56] Mourad, M.; Wijnhoven, J.; van't Zand, D.; van der Beek, D.; Lekkerkerker, H. Phil. Trans. R. Soc. A **2006**, 364, 2807
[57] van der Kooij, F. M.; Lekkerkerker, H. N. W. J. Phys. Chem. B **1998**, 102, 7829
[58] van der Beek, D.; Lekkerkerker, H. N. W. Langmuir **2004**, 20, 8582
[59] Michot, L. J.; Bihannic, I.; Maddi, S.; Funari, S. S.; Baravian, C.; Levitz, P.; Davidson, P. PNAS **2006**, 103, 16101
[60] Michot, L. J.; Bihannic, I.; Maddi, S.; Baravian, C.; Levitz, P.; Davidson, P. Langmuir **2008**, 24, 3127
[61] Israelachvili, J. Intermolecular Surface Forces. Academic Press, Inc., London, **1992**
[62] Schmidt, M.; Dijkstra, M.; Hansen, J.-P. J. Phys.: Condens. Matter **2004**, 16, S4185
[63] Baulin, V. A. J. Chem. Phys. **2003**, 119, 2874
[64] Dogic, Z.; Philipse, A. P.; Fraden, S.; Dhont, J. K. G. J. Chem. Phys. **2000**, 113, 8368
[65] Gonzalez, A. E. Phys. Rev. Lett. **2001,** 86, 1243
[66] Gonzalez, A. E. Eur. Phys. J. E **2004** 13, 165
[67] Fonseca, D. d.M. ; Meheust, Y. ; Fossum, J. O. ; Knudsen, K. D. ; Maly, K. J. ; Parmar, K. P. S. J.Appl. Cryst. **2007**, 40, 292
[68] Kaviratna, P. D.; Pinnavaia, T. J.; Schroeder, P. A. J. Phys. Chem. Solids **1996**, 57, 1897
[69] Knudsen, K.D.; Fossum, J.O.; Helgesen, G.; Bergaplass, V. J.Appl.Cryst. **2003**, 36, 587
[70] Bates, M. A.; Frenkel, D. J. Chem. Phys. **1999**, 110, 6553
[71] Veerman, J. A. C.; Frenkel, D. Phys. Rev. A **1992**, 45, 5632
[72] Bates, M. A. J. Chem. Phys. **1999**, 111, 1732
[73] Abend, S.; Lagaly, G, Applied Clay Science **2000**, 16, 201
[74] Rowan, D. G.; Hansen, J. P. Langmuir **2002**, 18 , 2063
[75] van der Beek, D.; Davidson, P.; Wensink, H. H.; Vroege, G. J.; Lekkerkerker, H. N. W. Phys. Rev. E **2008**, 77, 031708
[76] Peroli, G. G.; Hillig, G.; Saupe, A.; Virga, E. G. Phys. Rev. E **1998**, 58, 3259

Paper 3

D. M. FONSECA, Y. MÉHEUST, J. O. FOSSUM, K. D. KNUDSEN, K. J. MÅLØY AND K. P. S. PARMAR

Phase behavior of platelet-shaped nanosilicate colloids in saline solutions — a small-angle X-ray scattering study

Journal of Applied Crystallography **40**, s292–s296 (2007)

Journal of
Applied Crystallography
ISSN 0021-8898

Received 16 August 2006
Accepted 7 March 2007

Phase behavior of platelet-shaped nanosilicate colloids in saline solutions – a small-angle X-ray scattering study

D. M. Fonseca,[a]* Y. Méheust,[a,d] J. O. Fossum,[a]* K. D. Knudsen,[b] K. J. Måløy[c] and K. P. S. Parmar[a]

[a]Physics Department, Norwegian University of Science and Technology (NTNU), Trondheim, Norway, [b]Physics Department, Institute for Energy Technology (IFE), Kjeller, Norway, [c]Physics Department, University of Oslo (UiO), Oslo, Norway, and [d]Geosciences Rennes, UMR CNRS 6118, Université de Rennes 1, Rennes, France. Correspondence e-mail: davi.fonseca@phys.ntnu.no, jon.fossum@ntnu.no

A study of polydisperse suspensions of fluorohectorite clay in saline solutions is presented. The suspended clay colloids consist of stacks of nanosilicate sheets several tenths of a nanometre thick. They are polydisperse both with respect to the number of stacked nanolayers and with respect to their extension along the sheets. Due to this polydispersity, a spontaneous gravity-induced vertical segregation occurs in the sample tubes and results in the presence of up to four different phases on top of each other. Precise characterization of the phase diagram of the samples as a function of salt concentration and vertical position in the tubes, based on small-angle X-ray scattering data, is presented. The vertical positions of the phase boundaries were monitored by analyzing the eccentricity of elliptic fits to iso-intensity cuts of the scattering images. The intensity profiles along the two principal directions of scattering display two power-law behaviors with a smooth transition between them and show the absence of positional order in all phases.

1. Introduction

Colloidal suspensions of 2:1 clay particles in aqueous salt solutions make ideal model systems for the study of interactions between platelet-shaped particles. Indeed, the particle–particle interaction consists of (i) the van der Waals attraction and (ii) the electrostatic repulsion between the particles' electric double layer (McBride & Baveye, 2002). The extension of the latter repulsion can be easily tuned by changing the electrolyte concentration (Israelachvili, 1992). This complex particle–particle interaction combined with the strong particle anisotropy results in rich phase behaviors. The phase diagram of the monodisperse synthetic 2:1 clay laponite dispersed in saline solution, in particular, has been the subject of much attention (Mourchid *et al.*, 1998; Bonn *et al.*, 1999; Lemaire *et al.*, 2002). Such dispersions are now well known for the existence of a spontaneous nematic arrangement of the platelets at given salt and particle concentrations (Mourchid *et al.*, 1998; Lemaire *et al.*, 2002; van der Beek & Lekkerkerker, 2003).

Another synthetic clay, sodium fluorohectorite (NaFHT), has been found to exhibit interesting phase behavior when suspended in saline solutions. NaFHT presents polydispersity in both particle size and aspect ratio (Kaviratna *et al.*, 1996). In the presence of polydispersity a spontaneous phase segregation occurs in the suspensions (Fossum, 1999; Bates, 1999; van der Kooij *et al.*, 2001), with several phases coexisting in strata. X-ray diffraction studies of such systems (DiMasi *et al.*, 2001) have investigated the clay particles' orientations in these NaFHT–NaCl–H_2O systems, taking advantage of their nano-layered nature. Three distinct gel regions were identified and characterized by differences in orientational order and/or the size of ordered domains. One phase was presented as nematic. Those findings are consistent with visual observations (Fossum *et al.*, 2005), including observations through crossed polarizers: a birefringent region, coinciding with the region exhibiting orientational order (as inferred from the wide-angle X-ray scattering study), was observed. More recently, the existence of an isotropic-to-nematic transition in these systems has been corroborated by MRI studies of anisotropic water self-diffusion (de Azevedo *et al.*, 2007).

However, the corresponding phase diagram has not yet been determined with precision, nor has the orientationally ordered gel phase been fully characterized as nematic. In the present work, synchrotron small-angle X-ray scattering (SAXS) is used to obtain a fine characterization of the phase diagram over a large NaCl concentration range.

2. Experimental method

2.1. Samples

The samples consist of NaFHT crystallites suspended in a saline solution. They were prepared in the following way: lithium fluorohectorite clay was purchased in powder form from Corning Inc. (New York). It was cation-exchanged using NaCl, and then the extra Cl^- ions were removed through dialysis. After drying, the obtained clay crystallites have the nominal chemical formula $Na_{0.6}(Mg_{2.4}Li_{0.6})Si_4O_{10}F_2$.

Several suspensions of such crystallites were subsequently prepared, with a 3 wt% concentration of clay and NaCl concentrations ranging from 0.1 to 25 m*M* (Table 1). After addition of the clay

Table 1
Vertical positions at which SAXS data were recorded for each sample.

Saline concentration (m*M*)	Starting position† (mm)	Step size (mm)	Number of SAXS scans
0.1	0	1	15
0.25	0	1	23
0.5	0	1	23
0.75	0	0.5	45
1.0	0	0.5	45
2.5	1	0.5	45
5.0	1	0.5	45
7.5	1	0.5	45
10	1	0.5	45
25	1	0.5	55

† Above the bottom of the sample.

powder to the saline solution, the suspensions were left shaking overnight; after twelve hours, they were poured into 2 mm diameter capillaries made of quartz glass (Hilgenberg Mark tubes with 0.01 mm wall thickness). They were then allowed to settle for 30 days. After this time, one could observe up to four superimposed phases, as shown in Fig. 1: the phase at the very bottom is opaque; that on top of it is a translucent gel; the third phase observed from the bottom up is a transparent gel; the top phase is a transparent sol.

2.2. Scattering setup

SAXS experiments were performed on the Dutch–Belgian Beamline (DUBBLE) at the European Synchrotron Radiation Facility (ESRF) in Grenoble (France). This beamline provides focused monochromatic radiation with an energy tunable in the range 5–30 keV, corresponding to wavelengths between 0.41 and 2.48 Å. A wavelength of 1.55 Å was chosen for this experiment.

The experimental hutch contains the SAXS camera with a maximum and minimum sample-to-detector distance of 8 and 1.4 m, respectively. The maximum camera length $D = 8$ m was chosen for the whole length of the measurements, so as to investigate length scales as large as possible. Two-dimensional SAXS images were recorded using a two-dimensional multiwire gas-filled detector (Gabriel & Dauvergne, 1982). This detector has an image size of 133× 133 mm with a spatial resolution of 250 ± 5 µm. The beam size that we used had a diameter of ~0.2–0.3 mm and the beam stop was approximately a 5 × 5 mm square. Consequently, for the chosen wavelength λ of 1.55 Å, the q range accessible in the experiment was 0.013–0.33 nm^{-1} [where $q = (4\pi/\lambda)\sin\theta$ and 2θ is the scattering angle], corresponding to probed length scales between 20 and 480 nm. The measurement setup also contains a linear wide-angle X-ray scattering (WAXS) detector based on a curved microstrip glass strip counter. This allowed us to simultaneously record SAXS and WAXS data with a time resolution down to 1 ms per timeframe. The WAXS data will not be discussed in this paper.

In order to avoid repeatedly entering the experimental hutch to change samples, a sample holder containing ten capillaries placed side by side and regularly spaced was employed. The samples were placed in the beam in turn by translating the holder using a remotely controlled horizontal translation stage. Another translation stage allowed control of the vertical position of the sample with respect to the beam.

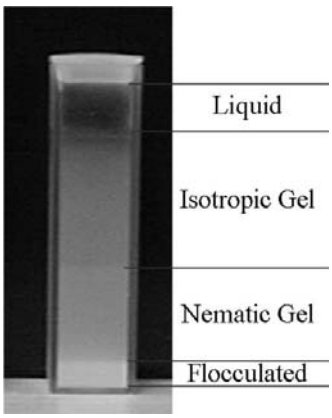

Figure 1
A sodium fluorohectorite sample with a particle concentration of 3 wt% and an NaCl concentration of 4.5 m*M*. The four phases are easily identifiable.

2.3. Experimental protocol

For each sample: (i) a vertical transmission scan was carried out and (ii) SAXS patterns at different heights were collected. Table 1 lists the details of the vertical positions at which SAXS data were recorded for each sample. The liquid phase at the top of the sample tube was not investigated. All SAXS images were recorded with an exposure time of 60 s. They were subsequently corrected for the detector's transfer function and normalized with respect to the sample transmission. Scattering from the empty tubes proved to be negligible compared to the data and therefore no subtraction of the empty tube data was necessary.

3. Data analysis

3.1. Method

Fig. 2 displays examples of SAXS images recorded from the lower and upper gel phases for a salt concentration of 1 m*M*. The data in

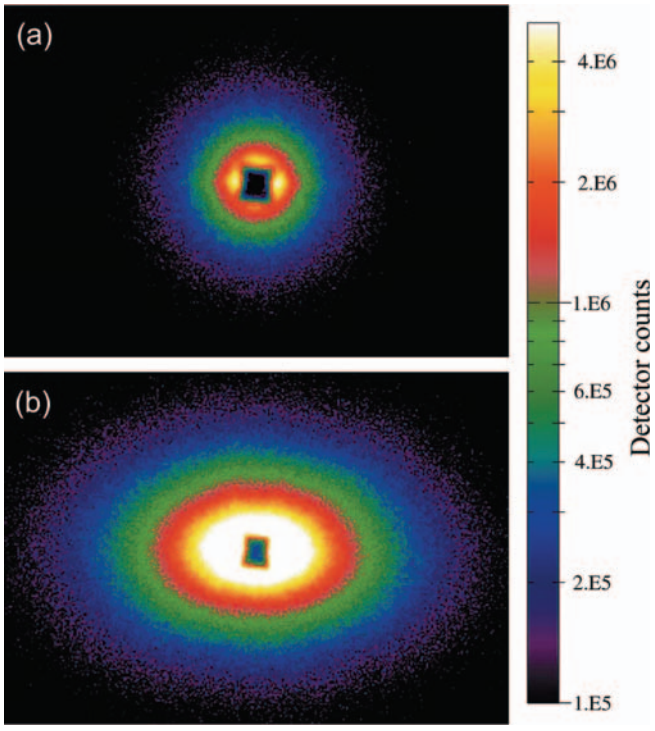

Figure 2
SAXS images recorded in the upper (*a*) and lower (*b*) gel phases. The anisotropic image in (*b*) indicates a preferential orientation of the clay crystallites in the lower phase.

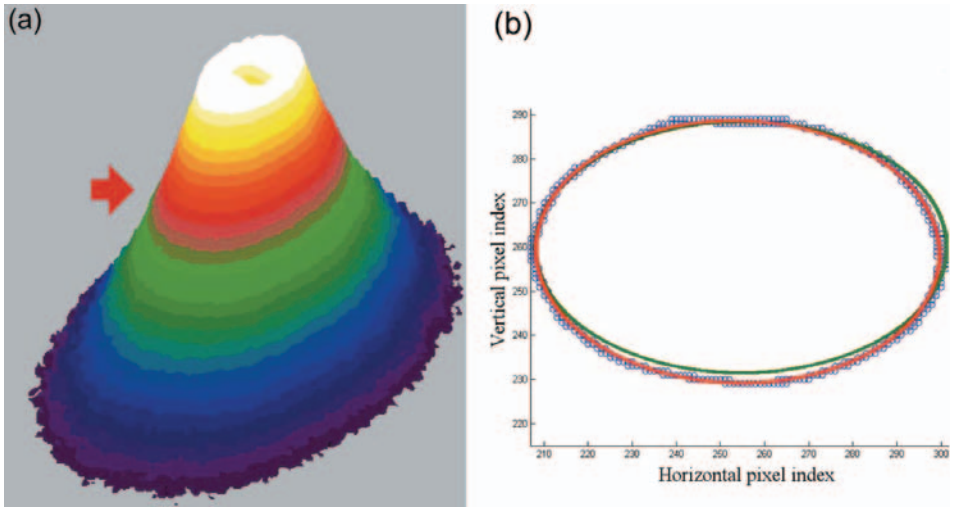

Figure 3
(*a*) A three-dimensional view of a scattering image. The arrow indicates a range that could be used to generate the cloud of points. (*b*) The blue circles represent the cloud of points inside the range of the scattering profile. The green ellipse is the initial guess for the fitting procedure. The red ellipse is the evaluated best fit to the cloud of points.

Fig. 2(*a*) are isotropic, while those displayed in Fig. 2(*b*) are clearly anisotropic, indicating a preferential orientation of the clay crystallites.

Iso-intensity lines of the SAXS images are well described by ellipses. Hence, a custom-made *MATLAB* program was used to fit ellipses to such iso-intensity lines. The fitting procedure is accomplished in the following way. First, a narrow intensity range is selected (Fig. 3*a*), and then the pixels with an intensity that falls in that range are extracted from the two-dimensional SAXS image. Subsequently an ellipse is fitted to the cloud of points defined by the horizontal and vertical coordinates of the selected pixels (Fig. 3*b*). This procedure provides the center of the ellipse, the length of its major axis, a, that of its semi-minor axis, b, and its angle of tilt with respect to the horizontal. From a and b one can calculate the eccentricity, e, where $e = [1 - (b^2/a^2)]^{1/2}$. This procedure was tested at different intensity levels and the fit results were shown to depend only weakly on the intensity range used to obtain them.

The obtained fit parameters can be related to the scattering process as follows: (i) the center of the ellipse is a fine estimate for the position of the direct beam; (ii) the principal axes of the ellipse are related to the orientational ordering of the scattering clay particles; (iii) the eccentricity of the ellipse is a measure of the image's anisotropy: an image with a perfect axial symmetry would yield a value e = 0, while a value closer to 1 denotes a very anisotropic image; and (iv) the angle of tilt of the ellipse is related to the preferential orientation of the scatterers with respect to the laboratory frame.

Finally, one-dimensional intensity profiles of scattering intensity *versus* q along the principal axes of the ellipses were computed. Those profiles were generated by integrating the images over azimuthal angles in 5° wide sectors around each of the principal directions. The resolution of these profiles along the radial direction was set to 250 radial bins.

3.2. Results

3.2.1. Phase diagram. The computed eccentricities were plotted as a function of the vertical position for each sample. From these plots (not shown here) it is readily noticeable that: (i) a region at the bottom part of the sample corresponds to eccentricities spread over a wide range of values, (ii) a region which only contains high eccentricity values is found on top of the latter one, and (iii) the third region from the bottom up contains only low eccentricity values. Note that the fourth (and top) phase observed visually in the highest part of the sample tube was not studied by SAXS, and will not be discussed in what follows. The three regions found from the SAXS data correspond to the three bottom phases observed visually. Since the anisotropy of the scattering images is characteristic of particle orientational ordering, the phases were identified as the sediment, a gel phase with preferential particle ordering and an isotropic gel, respectively.

From these plots for individual samples, a surface plot taking all samples into account was constructed. Since the concentrations used here form a nonregular and nonmonotonic grid, *MATLAB* was used to interpolate the data on a regular grid. Fig. 4(*a*) shows a grayscale view of the surface plot, with salt concentration along the horizontal axis and vertical position along the vertical axis; grayscale intensities denote the eccentricity value at a given point of the parameter space. In this representation, sudden changes in the gray level denote possible phase boundaries. A dark gray zone at the top of the image obviously denotes the isotropic gel phase, since the scattering from that phase is isotropic. On the other hand, the images collected in the gel phase with a preferential orientation of the particles must correspond to high eccentricities, since the characteristic orientational ordering causes a very anisotropic scattering. Therefore, the white zone on the left part of the image, under the region corresponding to the isotropic gel, corresponds to that anisotropic gel.

In order to complete our understanding of the phase boundaries as inferred from the SAXS data, a grayscale image of the transmission data was also made (Fig. 4*b*). Owing to the relatively sharp change in transmission from the sediment to the gel phases, it is easy to identify the sediment. Note that the images of Figs. 4(*a*) and 4(*b*) complement each other; their joint interpretation allows clear definition of the phase boundaries for the sediment, anisotropic gel and isotropic gel. We are left with an unidentified region in the right-hand part of the image, between the regions corresponding to the sediment and to the isotropic gel. That region exhibits moderate attenuation and moderate eccentricity values that vary on a small scale in the parameter space. It also exhibits all possible angles of tilt for the fitted ellipses (tilt-angle data are not shown here).

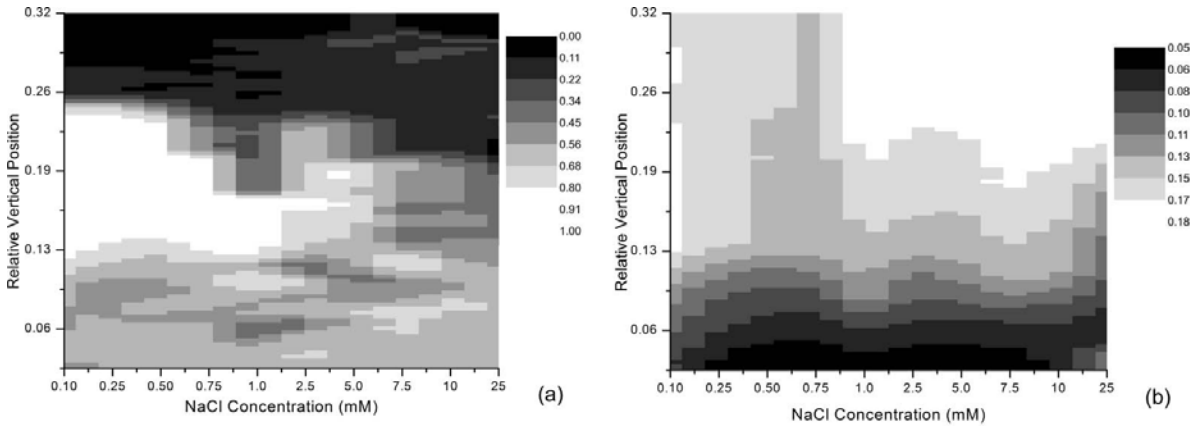

Figure 4
(*a*) Grayscale map for the eccentricity values computed from the SAXS data as a function of the salt concentration and vertical position in the sample tubes. (*b*) As for (*a*), but computed from the transmission data.

Fig. 5 summarizes this phase diagram for the suspensions. Note that the use of the relative vertical position as a vertical axis in Fig. 5 is somewhat unphysical. It can however be related to a more physical parameter such as the particle volume fraction. Indeed, the vertical phase segregation is thought to be related to a vertical gradient in volume fraction, as a consequence of polydispersity. In this sense, the phase diagram in Fig. 5 can be related to better-known phase diagrams of clay colloids in saline solution (that of laponite, for example) as a function of particle volume fraction and ionic strength of the solution. We do not know yet how the relative vertical position in the tube translates into local volume fraction, hence we cannot convert the vertical axis into a volume fraction axis. When Fig. 5 is compared to the two previous estimates of the diagrams, one from visual observation, the other one from WAXS data [see DiMasi *et al.* (2001) and Fossum *et al.* (2005)], it is evident that the main features are consistent. The anisotropic gel found here is the nematic gel phase as identified from WAXS data. Fig. 2(*b*) is a typical SAXS image recorded from this phase; the orientation of the elliptic iso-intensity lines is consistent with the previous WAXS analyses, according to which the platelet-shaped clay particles are standing on

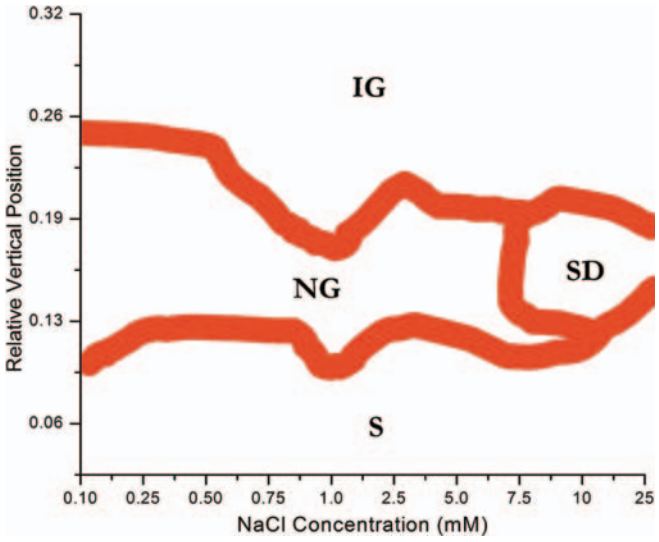

Figure 5
Phase diagram created from the grayscale maps for eccentricity and transmission. The displayed regions are sediment (S), nematic gel (NG), isotropic gel (IG) and a region containing small domains (SD). The line thickness corresponds to the uncertainty on the boundary position.

average with their short dimension along the horizontal (DiMasi *et al.*, 2001). The rightmost region in the diagram (Fig. 4*a*) corresponds to what DiMasi *et al.* (2001) denote as a small nematic domain phase (SD). We believe that this region contains in fact many small nematic regions. On the scale of the scattering volume, this results in SAXS data with a moderate anisotropy, the magnitude and preferential orientation of which are not fixed for the whole region.

Two discrepancies between the current phase diagram and the previous estimates can be spotted. One of them is that the phase boundaries are not exactly at the same vertical position. This is expected since the samples in the different experiments were allowed to settle for unequal times and the phase boundaries are known to change position for several months before they stabilize. The other evident new observation compared to our previous studies concerns the boundary of the two gel phases at low salt concentrations. Its first two points in the previous estimates are much higher than that observed here (around two times higher) with respect to the rest of that boundary. The behavior observed in the present experiment is systematic and is observed for five different concentrations here, whereas it was observed for only two concentrations in the other works. Currently, one may suggest several alternative explanations for this difference and this will be a subject for future work.

3.2.2. Spectra along the principal axes. For a given SAXS image, the scattering intensity as a function of the modulus q of the scattering vector was also plotted along the two principal directions of the image, as determined by the fitting of ellipses to iso-intensity lines. Fig. 6 presents such q plots for a SAXS image in the isotropic phase and another one in the nematic phase of the sample with a saline concentration of 1 m*M*.

The q plots in Fig. 6 appear as consisting of several power-law regimes. This is expected in SAXS data from systems of aggregated particles (Schmidt, 1991). On all plots, a smooth crossover is noticed. It corresponds to a characteristic length scale of ~20 nm. This could be related to the average thickness of the stacks of clay platelets, which is the only characteristic length of the particles that can be probed in the q range investigated with SAXS. Another interpretation for this crossover scale would be that small nematic domains exist locally in the two gel phases, with a typical particle-to-particle distance of around 20 nm. The crossover is smooth due to polydispersity in the particle thicknesses. Note that the characteristic length scale does not correspond to a regular periodicity in the mesostructure, since no peak is visible in the data at the corresponding q value. Hence, none of the phases exhibits positional order on the length scales probed by the SAXS experiment. In particular,

Table 2
Power-law exponents determined from Fig. 6.

	Slope left of crossover	Slope right of crossover
Nematic along semi-major axis	-2.2 ± 0.2	-2.8 ± 0.1
Nematic along semi-minor axis	-2.3 ± 0.1	-2.9 ± 0.1
Isotropic along semi-major axis	-2.2 ± 0.1	-2.4 ± 0.1
Isotropic along semi-major axis	-2.5 ± 0.1	-2.4 ± 0.2

the lower gel phase is ordered with respect to particle orientations but not to positions.

The values for the exponents of the power laws, as estimated from slopes in the log–log plots in Fig. 6, are presented in Table 2. We notice that at higher q values the slopes seem to approach -4, possibly indicating crossover into the Porod regime as the probed length scales become smaller than the crossover length scale. We also notice that at lower q values the slopes approach -2. This is expected for monodisperse platelets with no correlations between particle positions and orientations, either (i) nematically oriented, provided that q is pointing along the normal to the platelets, or (ii) randomly oriented (Ramsay, 1990). For nematically oriented monodisperse platelets with no correlations between positions and orientations, a slope of -3 is expected when q points perpendicular to the short plate direction (Ramsay, 1990). Note that our observations in terms of power-law exponents may be influenced by the fact that our platelets are not monodisperse, and that positions and orientations of particles may be correlated.

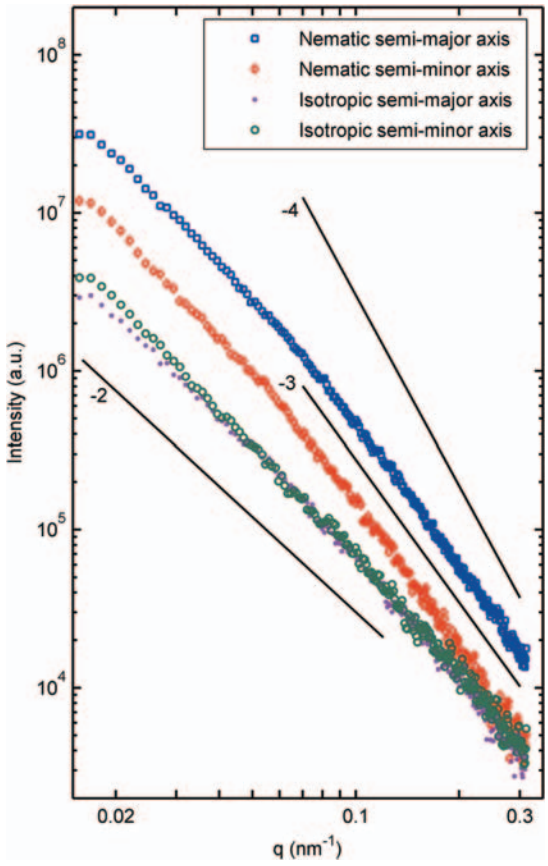

Figure 6
Integrated intensity plots as a function of the modulus of the scattering vector, q, along the principal axes of the ellipse, for a point in the isotropic phase and also for a point in the nematic phase. The smooth crossover is positioned at a q value corresponding to a length scale of about 20 nm. The solid lines denote reference slopes.

4. Conclusion

SAXS experiments have allowed a precise characterization of the phase diagram of suspensions of sodium fluorohectorite platelet-shaped particles in saline solutions. The characterization was done based on transmission data and on two-dimensional SAXS images.

Ellipses were fitted to iso-intensity lines of the SAXS images. The phase boundaries were obtained through joint analysis of the transmission data and of results for the eccentricities and tilt angles of the ellipses. Among the different phases observed, one is a gel phase exhibiting a high degree of orientational order, while another is an isotropic gel. This phase diagram is consistent with our previous estimates using other approaches. Moreover, plots of the integrated intensities *versus* the modulus of the scattering vector along the principal axes of the ellipses for both gel phases exhibit power-law behaviors with a smooth crossover at a characteristic length scale that may correspond to the typical particle thickness, and exponents that approach those of well known configurations at the lower and higher q values. These q plots confirm that no positional order exists in any of the phases.

X-ray scattering techniques have proved to be appropriate for discriminating between different phases in these samples. Future work concerns further understanding of the differences between the different phases, in terms of the geometry of the porous space between the particles (Knudsen *et al.*, 2004), focusing on the power-law behavior of the q plots. The ultimate goal is to understand the underlying mechanisms responsible for the formation of the different phases.

The authors acknowledge the European Synchrotron Radiation Facility for provision of synchrotron radiation facilities and we would like to thank Dr Igor Dolbnya for assistance in using beamline BM26B. The two anonymous referees are also acknowledged for helping to improve the manuscript. This work has received partial financial support from the Research Council of Norway (RCN) through the NANOMAT Program: RCN project numbers 152426/431, 154059/420 and 148865/432, as well as through 138368/V30 and SUP154059/420.

References

Azevedo, E. N. de, Engelsberg, M., Fossum, J. O. & de Souza, R. E. (2007). *Langmuir*, **23**, 5100–5105.
Bates, M. A. (1999). *J. Chem. Phys.* **111**, 1732–1736.
Beek, D. van der & Lekkerkerker, H. N. W. (2003). *Europhys. Lett.* **61**, 702–707.
Bonn, D., Tanaka, H., Kellay, H., Wegdam, G. & Meunier, J. (1999). *Langmuir*, **15**, 7534–7536.
DiMasi, E., Fossum, J. O., Gog, T. & Venkataraman, C. (2001). *Phys. Rev. E*, **64**, 61704.
Fossum, J. O. (1999). *Physica A*, **270**, 270–277.
Fossum, J. O., Gudding, E., Fonseca, D. d. M., Méheust, Y., DiMasi, E., Gog, T. & Venkataraman, C. (2005). *Energy*, **30**, 873–883.
Gabriel, A. & Dauvergne, F. (1982). *Nucl. Instrum. Methods*, **201**, 223–230.
Israelachvili, J. (1992). *Intermolecular and Surface Forces*. London: Academic Press.
Kaviratna, P. D., Pinnavaia, T. J. & Schroeder, P. A. (1996). *J. Phys. Chem. Solids*, **57**, 1897–1906.
Knudsen, K. D., Fossum, J. O., Helgesen, G. & Haakestad, M. W. (2004). *Physica B*, **352**, 247–258.
Lemaire, B. J., Panine, P., Gabriel, J. C. P. & Davidson, P. (2002). *Europhys. Lett.* **59**, 55–61.
McBride, M. B. & Baveye, P. (2002). *Soil Sci. Soc. Am. J.* **66**, 1207–1217.
Mourchid, A., Lecolier, E., van Damme, H. & Levitz, P. (1998). *Langmuir*, **14**, 4718–4723.
Ramsay, J. D. F. (1990). *J. Chem. Soc. Faraday*, **86**, 3919–3926.
Schmidt, P. W. (1991). *J. Appl. Cryst.* **24**, 414–435.
Van der Kooij, F. M., van der Beek, D. & Lekkerkerker, H. N. W. (2001). *J. Phys. Chem. B*, **105**, 1696–1700.

Paper 4

D. M. FONSECA, Y. MÉHEUST, J. O. FOSSUM, K. D. KNUDSEN AND K. P. S. PARMAR

Phase diagram for polydisperse suspensions of platelet-shaped Na-Fluorohectorite: A synchrotron SAXS study

to be submitted to Physical Review E beginning of May 2008

The phase diagram of polydisperse Na-Fluorohectorite–water suspensions: A synchrotron SAXS study

D. M. Fonseca,[1,*] Y. Méheust,[1,2] J. O. Fossum,[1] K. D. Knudsen,[3] and K. P. S. Parmar[1,4]

[1] *Department of Physics, Norwegian University of Science and Technology (NTNU), Trondheim, Norway*
[2] *Geosciences Rennes, UMR CNRS 6118, Université de Rennes 1, Rennes, France*
[3] *Physics Department, Institute for Energy Technology (IFE), Kjeller, Norway*
[4] *Department of Chemical Engineering, Pohang University of Science and Technology, Pohang, South Korea*

(Dated: May 1, 2008)

Systems of platelet-shaped colloidal nanostacks of the synthetic clay Na-Fluorohectorite (Na-FH), suspended in saline solutions of various salt concentrations, exhibit a rich phase behavior with up to four phases coexisting in a single sample tube. They are studied here using small angle X-rays scattering: the anisotropy of the SAXS images is quantified, which, together with X-ray absorption measurements, provides a precise determination of the phase boundaries, as well as a measure of the orientational ordering of the clay colloids in the various gel phases. The vertical coordinate is shown to be associated within the samples to the clay particle fraction, which allows determination of a phase diagram for those Na-FH systems, as a function of the particle fraction and salt concentration.

I. INTRODUCTION

Liquid suspensions of clays have received special attention lately. This is due among other factors to their role as model systems for nanoparticle assembly and ordering, including long-range ordering phenomena. These clay systems are interesting both for industrial applications and also from a basic science point-of-view. Industrial applications for clay minerals range from petroleum relevance to food and cosmetics. Fundamental studies of the complex physical phenomena in clay systems, and the resulting applications, are far from complete. Being "abundant, inexpensive and environment friendly", clays are recognized by some authors as "the materials of the 21st century" [1].

The fluorohectorite studied here is a smectite clay, characterized by a layer structure with a layer thickness in the nanometer range. The smectite clay layer consists of one aluminum octahedral layer between two silicon tetrahedral layers (2:1 layer unit). The layers stack together but owing to their negatively charged surfaces, interacalate cations such as Na^+ or K^+ balance the charge and allow their stacking , see Fig. 1. Furthermore, these particle stacks can swell in the presence of water, i.e. water molecules may enter the interlayer space increasing the distance between layers [2].

The basic colloidal particle that we will be discussing in the present paper, are the stacks of such layers with counter-ions between them, which we will call platelet. The thickness, length, and surface charge of the platelets varies according to the type of ymsmectite clay. The extensively studied Laponite [3–5] for instance, has a platelet composed by a single 2:1 layer unit with a diameter of around 30 nm and thickness of 1 nm [6].

In the present work we study sodium fluorohectorite (NaFHT) which is a synthetic 2:1 clay mineral where Na^+ is the counter-ion in the interlayer space. NaFHT is characterized by a high surface charge, 1.2 e^- per unit cell and by its high polydispersity in both particle size and aspect ratio [7], the platelets display lengths varying from around 100 nm to 20 µm, and the observed thickness is in the 20–100 nm range [8]. NaFHT-NaCl-H_2O systems exhibit several coexisting phases which have been studied by X-ray diffraction [8], leading to the identification of three different gel phases characterized by differences in orientational order and/or size of the domains. Visual observations including the use of crossed-polarizers [9] corroborated these WAXS measurements since a birefringent region was found coinciding with the oriented one. Recent Magnetic Resonance Imaging (MRI) studies of anisotropic water self-diffusion [10] which confirmed the isotropic-to-nematic transition and helped understanding the orientation of the platelets, and small-angle x-ray scattering experiments (SAXS) [11] which attempted to obtain a fine characterization of the phase boundaries over a wide NaCl concentration range.

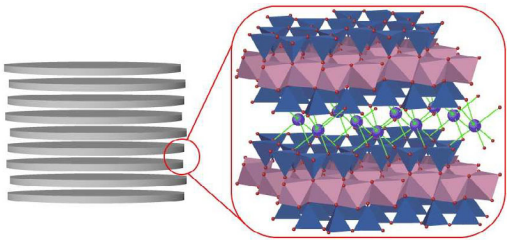

FIG. 1: (Color online) Simplified clay structure. The present smectite clay particles are formed by stacked platelets with a thickness in the range 20–100 nm and a length in the range 100–20000 nm. Detail: two platelets, each formed by a octahedral layer between two tetrahedral layers, and the counter-ions between them. For NaFHT the octahedra have Li and Mg and the tetrahedra are composed by Si, both structures have vertices of O and F, and the counter-ion is Na^+.

*fonseca@ntnu.no

Saline solutions of NaFHT exhibit interesting phase behaviors owing to the competition between the van der Waals attraction and the electrostatic repulsion between the particles [12] and also due to the strong particle anisotropy. Since the electrostatic repulsion can be controlled by adding ions [13], systems of smectite clays in saline solutions are good systems for the study of self-assembly from platelet-shaped colloidal particles, including nematic self-assembly [3, 5, 14]. The particle anisotropy plays an important role as showed by Onsager [15] is his prediction that they undergo an isotropic to nematic transition at appropriate concentrations. Another interesting system are hard colloidal gibbsite platelets with an average diameter of 237 nm and thickness of 18 nm, the system was the first one to display isotropic, nematic, and columnar phases [16, 17].

In order to study NaFHT dispersed in saline solutions we employ SAXS here we to attempt to obtain a proper phase diagram for the system, as determined by the volume fraction of clay and the concentration of sodium chloride. We also try to understand its conformation from the scattered spectra in the SAXS patterns: at the selected range of X-ray scattering vectors, SAXS provides information on the arrangement regarding some of the dimensions of interest for our system, namely the inter-particle spacing and the thickness of the particles.

II. EXPERIMENT

Li-fluorohectorite clay was purchased in powder form from Corning Inc. (New York). It was cation-exchanged using NaCl, and then dialyzed in order to remove the excess Na^+ and Cl^- ions, and finally dried at 105°C. The obtained clay crystallites have the nominal chemical formula $Na_{0.6}(Mg_{2.4}Li_{0.6})Si_4O_{10}F_2$. The samples were prepared though suspension of NaFHT in saline solutions at several concentrations, they are 3% NaFHT by mass and have the following NaCl concentrations: 0.1, 0.25, 0.5, 0.75, 1, 2.5, 5, 7.5, 10, and 25 mM. After their preparation they were left shaking for twelve hours at 1000 rpm. After that they were poured into 2 mm quartz capillaries until 7 cm of the capillaries were filled. Then the capillaries were sealed with melted wax and left settling for thirty days. After a few days of settling, one can observe up to four phases in each capillary depending on the saline concentration, Figs. 2(a)–2(b). The phase at the bottom is made of flocculated particles and is opaque; the one on top of it is translucent gel-like and is constituted by particles with a preferred direction of orientation; the next phase transparent gel-like created by particles without ordering; and the phase at the top is transparent sol-like. In case the saline concentration is further increased — at some point — it will lead to total flocculation of the clay particles. It is worth mentioning that the nomenclature used here could be wrong regarding our use of the *gel* word [4, 18]; since we could actually have a gel, a glass, or both at different electrolyte/clay concentrations. Discrimination between gel and glass for the present system is beyond the scope of the present work.

When the samples are put between crossed-polarizers, one can easily observe a birefringent phase, Fig. 2(c) clearly displays the birefringency of the nematic phase.

The SAXS experiment was performed on the Dutch-Belgian beamline (DUBBLE) at the European Synchrotron Radiation Facility (ESRF). The setup used covered the q-range $0.015 < q < 0.33\text{nm}^{-1}$ ($q = |\mathbf{q}| = \frac{4\pi}{\lambda}\sin\theta$, where λ is the X-ray wavelength and 2θ is the scattering angle), hence, the studied spatial resolution was approximately from 20 to 420 nm. Therefore, only the thickness of the aggregated particles and the expected interspacing can be present in the data. By collecting two dimensional (2D) data, we are able to distinguish standing aggregates from the laying ones and hence parallel arrangements from staggered ones.

Vertical transmission scans were performed for each sample, followed by the data collection of SAXS patterns at different heights, from 1 mm up to 23 mm above the bottom of the sample. The clear liquid phase is located higher than that for all samples, and it was not studied here. Examples of patterns collected at the nematic and isotropic phases are displayed in Fig. 3, it is clear that the patterns are quite different from one phase to the other. In the isotropic gel the iso-intensity lines are circles; for the nematic gel they are ellipses with high eccentricity.

After the end of the experiment the patterns and the transmission data were carefully data-reduced. The empty capillary scattering was not subtracted from the SAXS patterns since its scattering proved to be negligible compared to the scattering from the samples, but the empty tube absorption was taken into account in order to data-reduce the transmission data.

III. DATA ANALYSIS AND DISCUSSION

A. Phase Diagram

In order characterize the various phases we determine iso-intensity lines of the SAXS patterns. For instance in case we select an intensity of around 2×10^6 detector counts, we would have a circle in Fig. 3(a) and an ellipse for Fig. 3(b). In order to automate this analysis MATLAB was used to open each pattern, take a thin slice in intensity, and fit an ellipse to it. From this process, values for the semi axes a and b of the ellipse and its the angle of tilt were obtained; more details on this procedure can be found in Ref. [11]. Tables for the eccentricity ($e = \sqrt{1 - b^2/a^2}$) and the angle of tilt were built. However, since the saline concentrations used in the experiment form a non-regular and non-monotonic grid they were re-gridded in order to create color-maps from these tables, Figs. 4(a)–4(c). Owing to the fact that the angle of tilt has little significance for low eccentricity patterns (i.e., ellipses close to circles), the low eccentricity ($e < 0.5$) regions of Figs. 4(b) were whitened. Also,

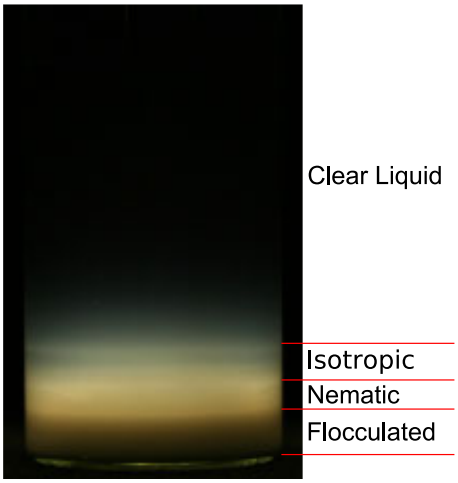

(a)Four phases coexist (different strata) in a single sample tube (circular Ø3 cm). 1 mM NaCl.

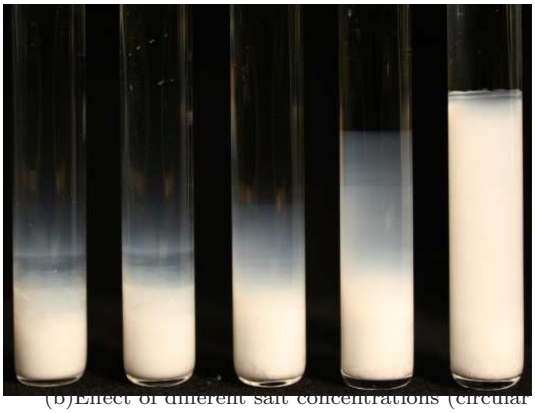

(b)Effect of different salt concentrations (circular sample tube Ø1 cm). The amount of electrolyte plays a very significant role on the system. NaCl concentrations from left to right: 0.01, 0.5, 1, 5, and 10 mM.

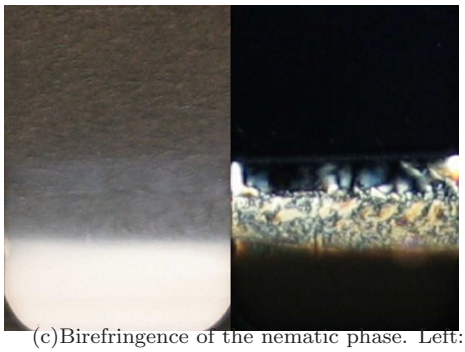

(c)Birefringence of the nematic phase. Left: sample with black paper behind (its texture is seen). Right: sample between crossed polarizers. From bottom to top: Opaque sediment, birefringent nematic, black isotropic with dendrites from nematic, and clear liquid separated by a thin line from isotropic (rectangular sample tube 1 × 10 mm^2).

FIG. 2: (Color online) Samples: H_2O+NaCl+NaFHT after settling under action of gravity. All studied samples are 3% by mass NaFHT.

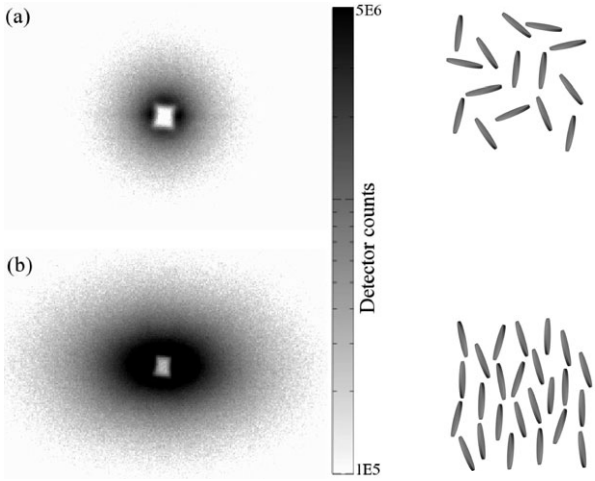

FIG. 3: Typical scattering patterns obtained in the experiment: (a) at isotropic phase, (b) at nematic phase. The sets of thin disks (viewed from the side) on the right exemplify possible arrangements responsible for creating the scattering patterns on the left.

since we are only interested in how much the particle orientations deviate from the horizontal and vertical, the angle data were re-mapped from the interval (0,360] degrees to (0,90] degrees.

From Figs. 4(a) and 4(b) we can easily identify the borders of the phases. The identification of the isotropic and nematic gels is rather straightforward since the former is characterized by low eccentricities (the ellipses are almost circles), while the latter is characterize by high eccentricities and low angles of tilt (the ellipses are horizontal). The sediment/flocculated phase display from low to average eccentricities and all possible angles of tilt, but on average they exhibit high angles of tilt (close to 90°). However for higher saline concentrations there is a change in behavior and, in the place where we would expect the nematic, higher angles of tilt are noticed, the eccentricities there are lower than in the nematic but higher than in the isotropic phase. Also, some of the SAXS patterns in this region seem to be the superposition of ellipses at different angles of tilt (hence the final eccentricity — as computed here — is lower than for the individual ellipses). This agrees with a previous suggestion [8] of small domains (SD) for those saline concentrations. Lastly, in order to separate the SD from the sediment we assumed that the transmission values associated to the angle of tilt data that separated sediment from nematic ($T \approx 0.1$) are still the threshold. The identified borders were put together in Fig. 5(a).

The next step is to go from the phase borders to a proper phase diagram, i.e. instead of using the height above the sample bottom we employ an intensive parameter; in the present case the clay volume fraction, which is known from Onsager's theory to be a potential order parameter for the isotropic-nematic transition. In order to determine its values we used the transmission data,

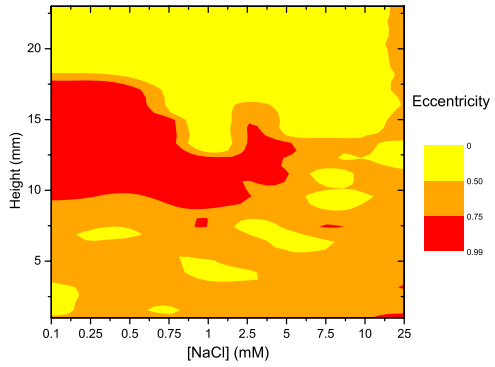

(a)Eccentricity.

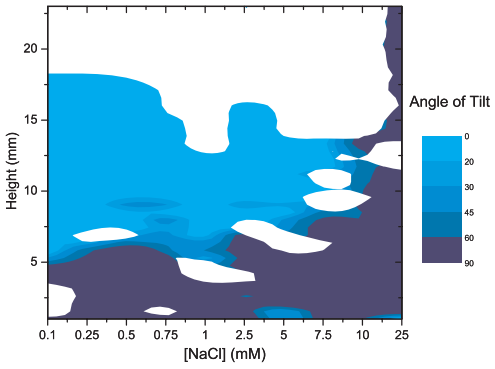

(b)Angle of tilt (low eccentricity areas were whitened).

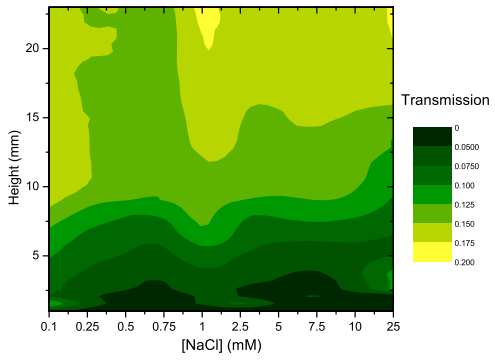

(c)Transmission.

FIG. 4: Color maps for the NaCl concentrations studied. The height above the bottom of the sample tube ranges from 1 up to 23 mm. (a) and (b) are constructed from analysis of so-intensity lines of the SAXS patterns.

starting by assuring that the data was properly reduced, i.e. the transmission comes only from the sample (no glass). The transmission is given by

$$T = \exp(-\mu\rho d)\,, \tag{1}$$

where μ is the mass absorption cross coefficient, ρ is the material density, and d is the thickness of the sample. Also, the linear absorption coefficient is defined as $\alpha \equiv \mu\rho$.

The x-rays illuminate a volume $V = Ad$, where A is the section of the incoming beam, and d is the diameter of the tube (if the beam is well centered on the tube). In case the probed volume is much greater than the volume of the particles, as it is in the present case, we can write

$$\alpha = \frac{\alpha_c V_c + \alpha_s (V - V_c)}{V}\,, \tag{2}$$

where α_c and α_s are the absorption coefficients for the clay and the solution, respectively, and V_c is the total volume occupied by the clay particles in the probed volume. Using Eq. 1, Eq. 2 becomes

$$\frac{1}{d}\ln T = -\frac{\alpha_c V_c + \alpha_s (V - V_c)}{V}\,. \tag{3}$$

We now note that the volume fraction of clay is given by

$$\Phi = \frac{V_c}{V}\,. \tag{4}$$

Putting together Eqs. 3 and 4 we obtain

$$\Phi = -\frac{\frac{1}{d}\ln T + \alpha_s}{\alpha_c - \alpha_s}\,. \tag{5}$$

In Eq. 5, T was measured in the experiment, d is known, and the values for α_s and α_c can be determined theoretically as follows. Knowing the energy of the x-rays (7.999 keV) one can evaluate the scattering cross section for each of the elements [19]. And then, from knowledge of the chemical formula, the cross sections for elements are weight-averaged in order to obtain the cross section for the components of our samples (see Table I). Here the cross section is the sum of both photoabsorption and inelastic scattering cross sections, since we have light elements. Also, it is worth noting that the energy employed is far from absorption edges.

Using the values from Table I and the density, one can find the respective linear absorption coefficients (Table II). From Eq. 5 and Tables I and II, a volume fraction color map is plotted (not shown here), and the borders from Fig. 5(a) are superimposed on this plot. Then, the values of the clay volume fraction along the borders are manually collected. And finally the phase diagram for the system is created by plotting these values, namely as Fig. 5(b). Note that the clear liquid phase was not studied and therefore its border is not presented here and that for the highest saline concentration the isotropic phase starts higher than the studied range thus it is not shown in the figure. We note that this approach is not completely sound measurement performed too close to the bottom of the sample, since the diameter of the capillaries usually varies there.

TABLE I: Calculated cross-sections.

NaCl				
Element	Atomic Weight	Relative Weight	Cross-section	Weighted cross-section
1× Na	22.99	0.39	28.42	11.178
1× Cl	35.45	0.61	104.89	63.629
Total	58.44			**74.807**
NaFHT				
Element	Atomic Weight	Relative Weight	Cross-section	Weighted cross-section
0.6× Na	13.79	0.04	28.42	1.014
2.4× Mg	58.33	0.15	39.79	6.003
0.6× Li	4.16	0.01	0.37	0.004
4× Si	112.34	0.29	61.67	17.919
10× O	159.99	0.41	11.35	4.696
2× F	38	0.1	15.52	1.525
Total	386.62			**31.160**
H_2O				
Element	Atomic Weight	Relative Weight	Cross-section	Weighted cross-section
2× H	2.02	0.11	0.35	0.040
1× O	16	0.89	11.35	10.078
Total	18.02			**10.118**

TABLE II: Cross sections for the compounds of interest at 20°C and for a wavelength of 1.55 Å.

Compound Material	ρ (g/cm^3)	μ (cm^2/g)	α (cm^{-1})
$Na_{0.6}(Mg_{2.4}Li_{0.6})$ $Si_4O_{10}F_2$	2.75	31.160	85.69
H_2O	0.9982	10.118	10.100
NaCl	2.16	74.807	161.583
0.1 mM NaCl	0.99824	10.118	10.100
0.25 mM NaCl	0.99825	10.119	10.101
0.5 mM NaCl	0.99826	10.120	10.102
0.75 mM NaCl	0.99827	10.121	10.103
1 mM NaCl	0.99828	10.122	10.104
2.5 mM NaCl	0.99834	10.127	10.111
5 mM NaCl	0.99844	10.137	10.121
7.5 mM NaCl	0.99855	10.146	10.132
10 mM NaCl	0.99865	10.156	10.142
25 mM NaCl	0.99927	10.212	10.205

The phase diagram shows a number of peculiarities for the NaFHT dispersions. We start by noting that it does not show a columnar phase as owing to the high polydispersity of the system. And then we observe that in the low NaCl range (up to 0.75 mM), an increase in saline or particle concentration favors flocculation regarding the NG–F transition; and it favors the nematic phase in the IG–NG case. Both cases were expected since as one adds more particles, making them approach each other more closely, one favors the alignment of the particles (hence, the nematic phase), and screening their charges through addition of electrolyte leads to the same result. As the particle/saline concentration is further increased it leads to flocculation of the particles.

From 1 mM to 2.5 mM there seems to be a discontinuity from the behavior at the left and at the right of this region. This has been confirmed since sudden changes in sample behavior happen for saline concentrations around 1 mM.

In the range from 2.5 mM and higher we notice that as the NaCl amount is increased the small domain phase appears. At the highest saline concentration studied, i.e. 25 mM, the phase diagram shows that the flocculated and nematic phases seem to have merged into a single phase which goes higher in the sample tube. Visual observation of the sample does not reveal a dividing line between nematic flocculated phases as the other samples do. This isotropic phase, which visually looks as the other isotropic phases for the lower saline concentrations, was not studied here and it is not shown in the phase diagram.

One possible interpretation for the observed behavior in the phase diagram is that we have both gel formation at lower saline concentrations (NG below 1 mM) and glass formation at higher phases (NG above 1 mM), similar to what was recently observed for Laponite [18]. Hence, we suggest that the region around 1 mM could be a transition region between both arrested states of matter. In this picture, a further increase in saline concentration leads to an attractive glass formation at high NaCl concentration (around 25 mM). This makes the present system a very interesting one for the current colloidal gel phase debate [18, 20].

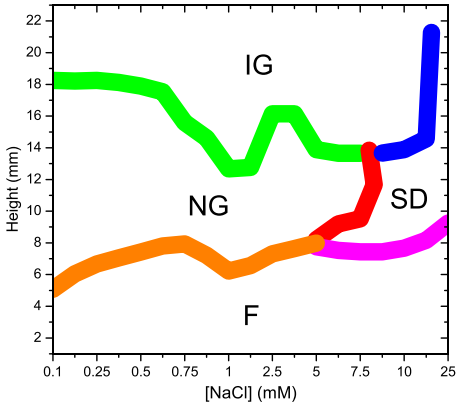

(a)Phase borders inferred from the eccentricity and angle of tilt color maps.

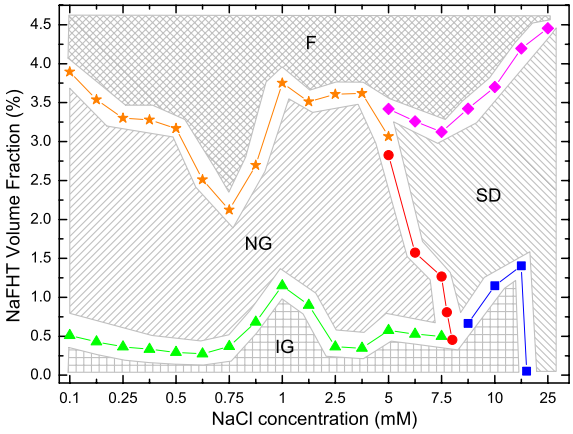

(b)The phase diagram of the Na-Fluorohectorite system, constructed from the (C_{salt}, z) phase borders and from the z to Φ (clay volume concentration) relation inferred from the transmission color map.

FIG. 5: (Color online) Phase borders for the samples.

Further studies are needed to understand the phases present in the diagram. Cryofracture could possibly elucidate how the particles are organized in each phase, and provide some idea about the particle distribution size at each phase. This information will help in attempting to model the NaFHT–NaCl–H_2O system.

B. Power Laws

When considering the radial decay of the scattering images, we notice that our system displays power-law behaviors, i.e. $I(q) \propto q^{-\kappa}$.

We have analyzed profiles of the scattering intensity, $I(q)$, as a function of q from cake integrations along the semi axes of the ellipse. Typical profiles for the three studied phases are exemplified in Fig. 6, where the plots regarding the sediment have been translated vertically by a factor of 10 whereas the ones for the isotropic phase have been displaced by 0.1. The obtained profiles do not present peaks, indicating the lack of positional ordering within this q-range.

The scattering patterns displayed in Fig. 6 show shoulders around 0.05–0.06 nm^{-1}, thus $1/q$ is approx. 20 nm. However, in the present case, with a system of thin platelets, the relevant crossover length is $2/q$, as shown in Eqs. A.5–A.7 in the Appendix. Thus we observe a characteristic average dimension of ca. 40 nm for the particles in our system. The shoulder is seen clearest for the nematic phase, but is present for all studied phases. It must therefore correspond to some dimension present in all phases, hence it is most likely related to the average platelet thickness in our system. We discuss now the slopes for high-q range, defined here as those where $q > 0.06$ nm^{-1}.

In Fig. 6(b) we notice that the slopes drop from -3.2 in the sediment to -2.4 in the isotropic phase. It is interesting to note that it changes differently in the nematic phase, for the semi-major axis it just decreases in a step to -2.8. However for the semi-minor axis it initially drops to -2.8 and then linearly decreases to -2.4. Owing to the polydispersity of the system and also to the particle interactions we can only attempt a qualitative analysis. We know (see the Appendix) that for highly ordered disks the decay in scattered intensity decays with exponent -3 for scattered vector perpendicular to the normal of the disk. On the other hand, along the direction where the scattering vector is parallel to the normal the power law has an exponent of -2. Hence from Fig. 6(b) we can infer qualitatively how the platelets are oriented in the nematic phase, since the ellipse tilt is 0° and since along the semi-major axis we observe a slope close to -3 whereas for the semi-minor axis it is around -2. This together with information from MRI results in Ref. [10] allows us to draw Fig. 7. From the MRI conclusions we also notice that we could not expect values of -3 and -2 since the particles with normal parallel to the beam (like those close to the wall) contribute to decrease the higher slope and increase the lower one. Here, since the sample tube is narrow, we have a nematic phase with a line defect with winding number equal to $+1$ [21, 22] and in case the diameter of the sample tube was increased the bulk would become isotropic, though the platelets close to the glass wall would still be oriented. A similar reasoning regarding the mild split in power-law slope can be used for the sediment. In that case the populations of standing and lying particles are similar in number (the split is small) but the higher number of lying platelets is responsible for the observed eccentricity.

The angles at the sediment (closer to 90°) are in agreement with Azevedo et al. [10], which concluded that at the transition from the nematic to the isotropic phases below (isotropic in terms of water movement) and above are edge to face this also agrees with Ref. [23].

In Fig. 8 we have plotted the evolution of the slopes along both semi axes, for all samples. For the semi-major

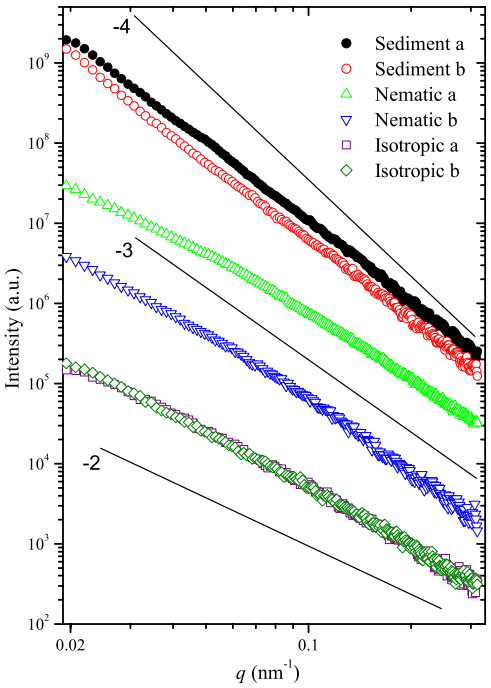

(a)Power law behavior along the semi axes a and b in the sediment (vertically displaced by ×10), nematic (no displacement) and isotropic (displaced ×0.1) phases. Note a shoulder around 0.05–0.06 nm^{-1} corresponding to an average particle thickness of around 40 nm. The lack of peaks indicates that there is no positional ordering.

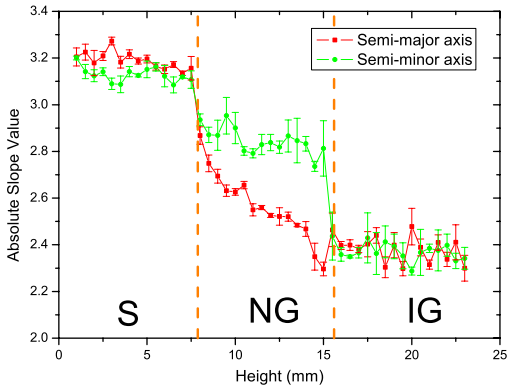

(b)Slope values at high-q range versus height in sample. There is a clear split in its values in the nematic phase and a small one in the sediment.

FIG. 6: (Color online) Scattering along the semi-major (a) and the semi-minor (b) axes for the 0.75 mM NaCl sample.

axis, all samples present the same behavior, with the exception of the highest saline concentration, namely 25 mM, which behaves in a similar way along both axes having a higher value than the others throughout. On the other hand, the semi-minor axis is different for the other concentrations; there we observe something curious, for

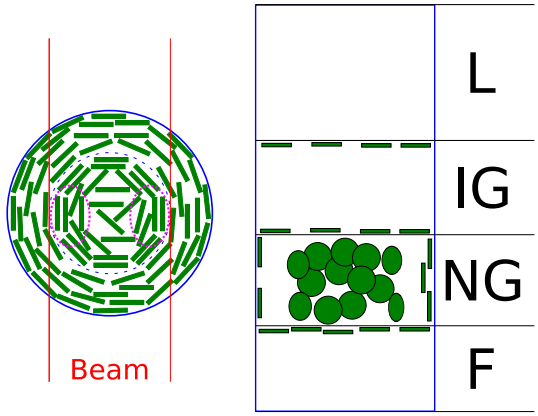

FIG. 7: (Color online) Organization of the platelets in the nematic phase and close to the phase borders. The disproportional image on the left is a section at the nematic phase. At the NG phase the particles contributing to the anisotropic scattering are between the particles close to the wall and those in the center, and they must have their length along the beam-path, they are denoted by the magenta dotted ellipses.

the low saline concentrations, namely 0.1–2.5 mM but not 1 mM, the decrease in slope now exhibits a step, while for the rest of the concentrations the decrease now starts higher in the sample tube.

Fig. 8 was plotted as colormaps. In Fig. 9, the difference between both axes is plotted, from which it is very clear that most of difference in behavior happens at the nematic phase were the absolute value of the slopes is higher for the semi-minor axis.

From Fig. 10 the characteristic length — inversely proportional to the position of the crossover — indicates thicker clay particles in the sediment (as expected). The behavior along both axes is very similar, indicating that the extinction of ordering in the center of the tube makes the diameter of the platelets visible along both axes, though weaker for b. In case we convert the shoulder position to the characteristic length, $2/q$, we note that in the sediment it has a value of around 45 nm for the a axis and 55 nm for the b one whereas for isotropic phase both are approximately equal to 30 nm, close to the value found in [2] and [8].

In Fig. 11 it seems that the particles are thicker for semi-minor axis at higher saline concentrations. However we believe that this comes from the statistics met when computing it, which was poorer than for the semi-major axis. Also, this suggests that particles are thicker in the floculated/sediment phase, but that they have similar dimensions in both isotropic and nematic gels.

IV. CONCLUSION

We employed SAXS to determine the proper phase diagram for the NaFHT-NaCl-H_2O system, for which all gel/glass phases are visible simultaneously in each sam-

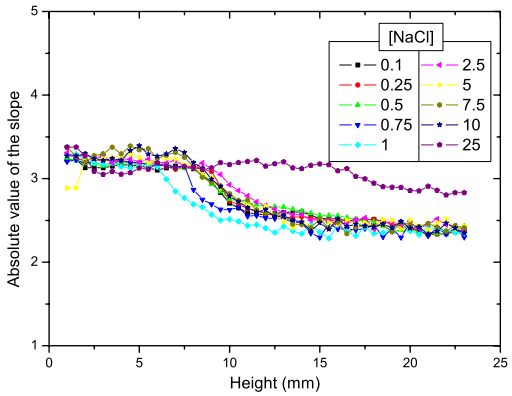

(a)Semi-major axis. For saline concentrations 0.1–10 mM all samples are similar of the exception of 0.75 and 1 mM which are in a discontinuity region from the gel to the glass.

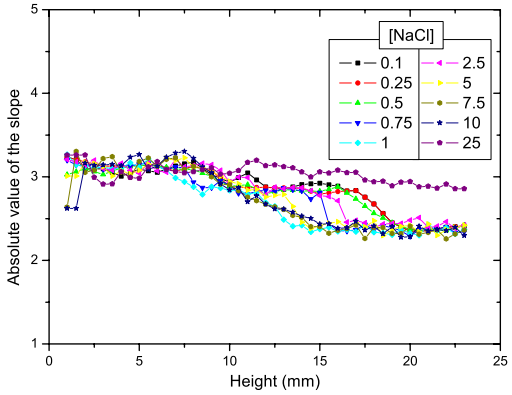

(b)Semi-minor axis. Some of the saline concentrations now exhibit a step.

FIG. 8: (Color online) Absolute values of the slopes at the high-q range for NaCl concentrations. The behavior at 25 mM NaCl is clearly different from that of the other saline concentrations

ple tube. The high polydispersity and the interaction of the particles did not allow us to fully understand the structural arrangement in the different phases, but we believe that there are different arrested states (gel and glass phases) in the phase diagram, though further investigation is needed to corroborate that. For future studies to be able to define particle conformation in all pahse, information on the particle-size distributions as a function of height in the sample tubes would be useful. To accomplish this, we believe that a throughout cryofracture study of the phase diagram should suffice. Also, we plan to complement our small-angle scattering data towards lower q-ranges than the one used here, in order to probe the length of the particles, using small angle light scattering (SALS) (or ultra SAXS); dynamic light scattering (DLS) could also provide information on the dynamics on the system.

The use of a 2D detector and analysis of the data along the two semi axes proved useful in determining the orientational configuration of the platelets in the nematic phase and to some extent in the flocculated phase. Unfortunately the particle configuration at the center of the tube made it impossible to completely decouple the optical axes of the particles. A new experiment using narrow rectangular-section cells instead of circular ones will probably allow more information to be extracted from the scattering intensity curves. However, by confronting the results from Ref. [10] to our observations, we were able to determine a plausible collective organization of the particles in the nematic phase.

Particles in the nematic and isotropic phases were observed to have similar thickness, whereas the flocculated phase presents thicker particles. The particles in the nematic phase have their edges close to the glass walls of the tube and the platelets are standing (their normal is perpendicular to the tube axis). Particles in the flocculated phase have an almost isotropic distribution of orientations when compared to the nematic phase, but a slight higher number of platelets is lying flat.

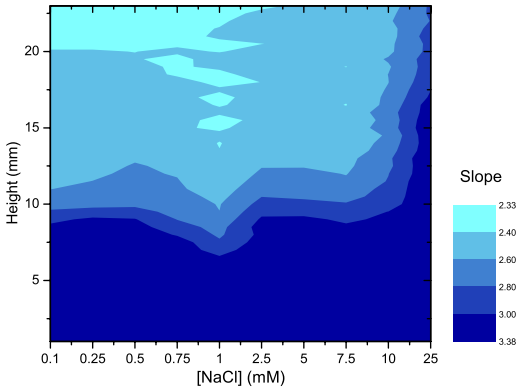

(a)Semi-major axis.

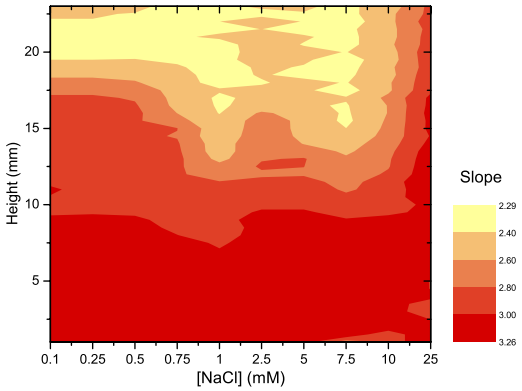

(b)Semi-minor axis.

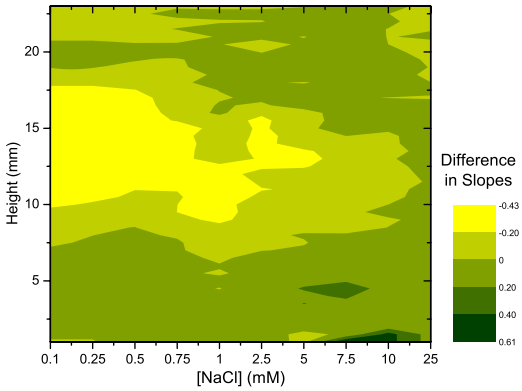

(c)Difference between (a) and (b).

FIG. 9: (Color online) Color maps for the absolute values of the slopes at the high-q range. We observe that (a) displays steeper slopes in the sediment, whereas (b) displays steeper slopes in the nematic phase.

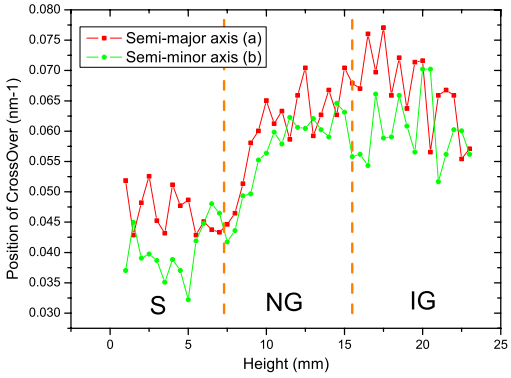

FIG. 10: (Color online) Crossover positions for sample with 2.5 mM NaCl.

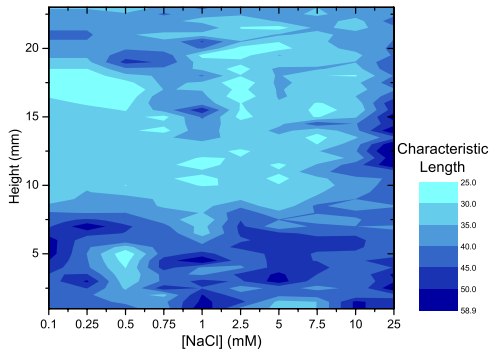

(a)Semi-major axis.

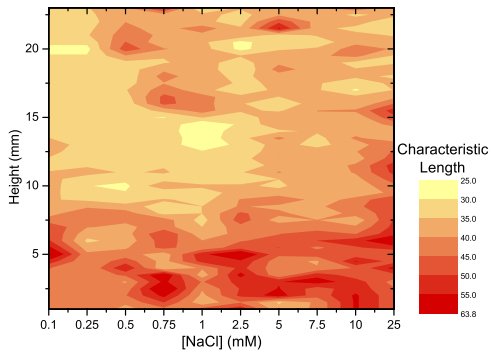

(b)Semi-minor axis.

FIG. 11: (Color online) Color map for the corresponding characteristic lengths for the crossover positions.

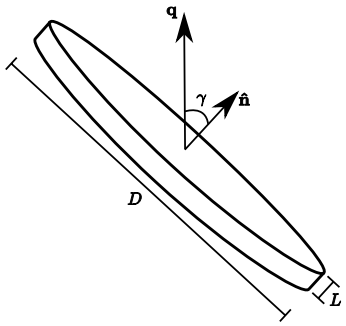

FIG. 12: Platelet.

Appendix: Power law behavior of model platelet systems

The form factor, $F(q)$, for a cylinder of diameter D and thickness L is given by [24]

$$F(q,\gamma) = \rho V \frac{\sin w}{w} \frac{2J_1(x)}{x}\,, \tag{A.1}$$

where

$$w = qL\cos\gamma/2 \tag{A.2}$$

and

$$x = q\frac{D}{2}\sin\gamma\,. \tag{A.3}$$

Here γ is the angle between $\mathbf{q}$ and the normal of the disk, $\hat{\mathbf{n}}$ (see Fig. 12), V is its volume, ρ is the electronic density difference between the particle and the medium, and J_1 denotes the first-order Bessel function of first kind.

For simplicity sake we will assume that the particles do not interact, hence the structure factor will be neglected, i.e. $S(q) = 1$. Also, we assume that the disks are monodisperse. In this case the scattered intensity for an isotropic system is

$$I(q) = K\langle|F(q)|^2\rangle_\gamma\,, \tag{A.4}$$

where K is an experimental constant and $\langle\rangle_\gamma$ show be understood as an average over all directions.

Following the results obtained in Ref. [25] for isotropic and oriented systems of platelets, we note that for thin platelets ($D \gg L$) the term in x in Eq. A.1 falls of much faster than then one in w. Hence only small values x will contribute to the average, i.e. when $\mathbf{q} \perp \hat{\mathbf{n}}$. Thus Eq. A.4 can be approximated to

$$I(q)_{\text{isotropic}} \approx KA\frac{2\pi}{q^2}\left[\frac{\sin(qL/2)}{qL/2}\right]^2\,. \tag{A.5}$$

Thus the scattering intensity obeys a q^{-2} power law, and in the limit of high-q it changes to the q^{-4} power law. However Eq. A.5 is not valid at low-q since in that case x becomes significant.

On the other hand, for highly oriented systems we can divide the observed behavior in two cases, namely transferred momentum along the normal of the platelet and perpendicular to it. In the former case, only the dependence in the diameter of the particle will survive, hence

$$I(q,\gamma=0)_{\text{oriented}} = K\left[\rho V\frac{\sin(qL/2)}{qL/2}\right]^2\,. \tag{A.6}$$

For the latter case we note the opposite, thus only dependence on the particle thickness contributes

$$I(q,\gamma=\pi/2)_{\text{oriented}} = K\left[2\rho V\frac{J_1(qD/2)}{qD/2}\right]^2\,. \tag{A.7}$$

Eqs.A.5–A.7 are plotted in Fig. 13 where the power law behavior for this model platelet system can be seen. From them we note that the crossover for randomly oriented disks occurs at $q \approx 2/L$. Also, we observe the modulation arising from $J_1(x)$ and $\sin w$. The expected power law behaviors are summarized in Table III.

Acknowledgments

The authors acknowledge the European Synchrotron Radiation Facility for provision of synchrotron radiation facilities and we would like to thank Dr. Igor Dolbnya for assistance in using beamline BM26B. This work has received partial financial support from the Research Council of Norway (RCN) through the NANOMAT Program: RCN project numbers 152426/431, 154059/420 and 148865/432, as well as through 138368/V30 and SUP154059/420.

[1] F. Bergaya, B. K. Theng, and G. Lagaly, eds., *Handbook of clay science* (Elsevier, Amsterdam, 2006).
[2] G. J. da Silva, J. O. Fossum, E. DiMasi, K. J. Måløy, and S. B. Lutnæs, Phys. Rev. E **66**, 011303 (2002).
[3] A. Mourchid, E. Lécolier, H. Van Damme, and P. Levitz, Langmuir **14**, 4718 (1998).
[4] D. Bonn, H. Tanaka, H. Kellay, G. Wegdam, and J. Meunier, Langmuir **15**, 7534 (1999).
[5] B. J. Lemaire, P. Panine, J. C. P. Gabriel, and P. Davidson, Europhys. Lett. **59**, 55 (2002).
[6] A. Mourchid, A. Delville, J. Lambard, E. Lécolier, and P. Levitz, Langmuir **11**, 1942 (1995).
[7] P. D. Kaviratna, T. J. Pinnavaia, and P. A. Schroeder, J. Phys. Chem. Solids **57**, 1897 (1996).
[8] E. DiMasi, J. O. Fossum, T. Gog, and C. Venkataraman, Phys. Rev. E **64**, 061704 (2001).
[9] J. O. Fossum, E. Gudding, D. d. M. Fonseca, Y. Meheust, E. DiMasi, T. Gog, and C. Venkataraman, Energy **30**,

TABLE III: Expected power law behavior.

Non-interacting monodisperse disks	(low-q)	$\frac{2\pi}{L}$	(medium-q)	$\frac{2\pi}{D}$	(high-q)
Randomly oriented	—		q^{-2}		q^{-4}
Highly oriented ($\mathbf{q} \perp \hat{\mathbf{n}}$)	—		—		q^{-3}
Highly oriented ($\mathbf{q} \parallel \hat{\mathbf{n}}$)	—		q^{-2}		q^{-2}

873 (2005).
[10] E. N. de Azevedo, E. Engesberg, J. O. Fossum, and R. E. de Souza, Langmuir **23**, 5100 (2007).
[11] D. M. Fonseca, Y. Méheust, J. O. Fossum, K. D. Knudsen, K. J. Måløy, and K. P. S. Parmar, J. Appl. Cryst. **40**, s292 (2007).
[12] M. B. McBride and P. Baveye, Soil Sci. Soc. Am. J. **66**, 1207 (2002).
[13] J. N. Israelachvili, *Intermolecular and Surface Forces* (Academic Press, London, 1992), 2nd ed.
[14] D. van der Beek, Ph.D. thesis, Utrecht University (2005).
[15] L. Onsager, Ann. N.Y. Acad. Sci. **51**, 627 (1949).
[16] F. M. van der Kooij, K. Kassapidou, and H. N. W. Lekkerkerker, Nature **406**, 868 (2000).
[17] D. van der Beek, P. Davidson, H. H. Wensink, G. J. Vroege, and H. N. W. Lekkerkerker, Phys. Rev. E **77**, 031708 (2008).
[18] B. Ruzicka, L. Zulian, R. Angelini, M. Sztucki, A. Moussaïd, and G. Ruocco, Phys. Rev. E **77**, 020402 (2008).
[19] `http://henke.lbl.gov/optical_constants/pert_form.html`.
[20] F. Sciortino, proceeding of Stat-Phys 2007. EPJB in press. (arXiv:0711.2220v1).
[21] N. D. Mermin, Rev. Mod. Phys. **51**, 591 (1979).
[22] R. Repnik, L. Mathelitsch, M. Svetec, and S. Kralj, Eur. J. Phys. **24**, 481 (2003).
[23] M. Dijkstra, J.-P. Hansen, and P. A. Madden, Phys. Rev. E **55**, 3044 (1997).
[24] A. Guinier and G. Fournet, *Small Angle Scattering of X-Rays* (Wiley, New York, 1955).
[25] J. D. F. Ramsay, S. W. Swanton, and J. Bunce, J. Chem. Soc. Faraday Trans. **86**, 3919 (1990).

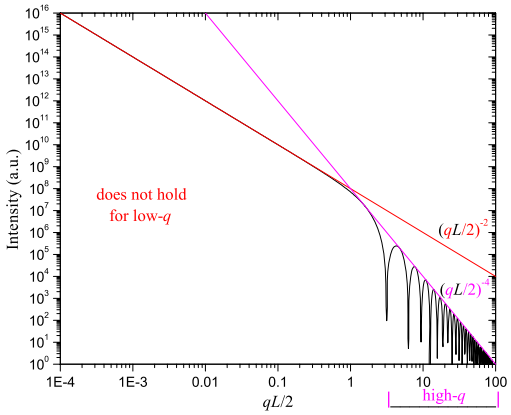

(a)Randomly oriented platelets case.

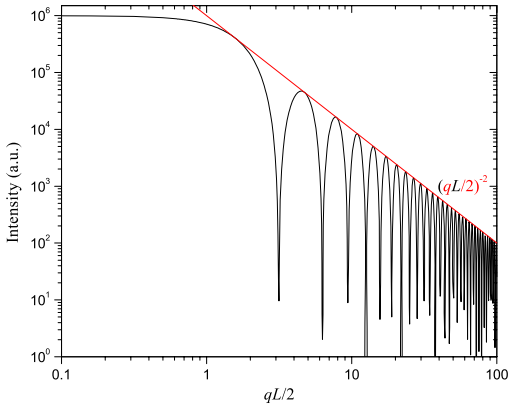

(b)Highly oriented platelets, parallel case ($\mathbf{q} \parallel \hat{\mathbf{n}}$).

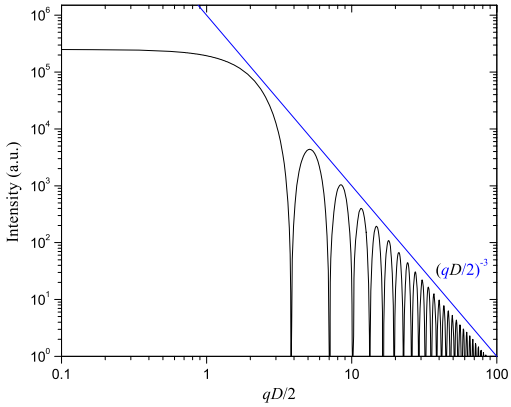

(c)Highly oriented platelets, perpendicular case ($\mathbf{q} \perp \hat{\mathbf{n}}$).

FIG. 13: (Color online) Expected power law behavior for non-interacting monodisperse platelets.

Paper 5 (Appendix)

Y. MÉHEUST, B. SANDNES, G. LØVOLL, K. J. MÅLØY,
J. O. FOSSUM, G. J. DA SILVA, M. S. P. MUNDIM, R. DROPPA
AND D. D. MIRANDA FONSECA

Using synchrotron X-ray scattering to study the diffusion of water in a weakly hydrated clay sample

Clay Science **12**, 66–70 (2006)

Clay Science 12 Supplement 2, 66-70 (2006)

Using Synchrotron X-ray Scattering to Study the Diffusion of Water in a Weakly-hydrated Clay Sample

Y. MÉHEUST [a, *], B. SANDNES [b], G. LØVOLL [b], K. J. MÅLØY [b], J. O. FOSSUM [a], G. J. DA SILVA [c], M. S. P. MUNDIM [c], R. DROPPA [d] and D. d. MIRANDA FONSECA [a]

[a] *Department of Physics, Norwegian University of Science and Technology, Hoegskoleringen 5, NO-7491 Trondheim, Norway*

[b] *Physics Department, University of Oslo, Postboks 1048 Blindern, NO-0316 Oslo, Norway*

[c] *Physics Department, University of Brasilia, Caixa Postal 04455, 70919-970 Brasília – DF, Brazil*

[d] *The Brazilian Synchrotron Laboratory (LNLS), Caixa Postal 6192, CEP 13084-971 Campinas – SP, Brazil*

(Received August 23, 2005. Accepted December 28, 2005)

ABSTRACT

We study the diffusion of water in weakly-hydrated samples of the smectite clay Na-fluorohectorite. The quasi one-dimensional samples are dry compounds of nano-layered particles consisting of ~ 80 silicate platelets. Water diffuses into a sample through the mesoporosity in between the particles, and can subsequently intercalate into the adjacent particles. The samples are placed under controlled temperature. They are initially under low humidity conditions, with all particles in a 1WL intercalation state. We then impose a high humidity at one sample end, triggering water penetration along the sample length. We monitor the progression of the humidity front by monitoring the intercalation state of the particles in space and time. This is done by determining the characteristic spacing of the nano-layered particles in situ, from synchrotron wide-angle X-ray scattering measurements. The spatial width of the intercalation front is observed to be smaller than 2mm, while its velocity decreases with time, as expected from a diffusion process.

Key words: Smectite, Nano-layered material, Water diffusion, Intercalation, WAXS

INTRODUCTION

Fluorohectorite is a synthetic smectite with formula $X_x(Mg_{3-x}Li_x)Si_4O_{10}F_2$ per half unit cell, where X is a cation (Na, Ni, Li, Fe). It is polydisperse, with platelets sizes ranging from a few tenth of nm up to a few micrometers, and has a large surface charge[1] (1.2 e- per unit cell, against 0.6 for montmorillonite) which causes platelets to remain stacked in water suspensions, even in low saline environment. These stacks are strengthened by the presence of the intercalated cation X, which is shared by two adjacent silica sheets in the stack. They contain on average around 80 platelets[2]. As for natural smectites, water molecules can also intercalate inside theses nano-layered particles, causing them to swell in a stepwise molecular packing process[3-5] where some configurations are thermodynamically favoured and interpreted as "water layers" successively intercalated in the stacks.

For Na-fluorohectorite (X=Na), which we study here, we observed no more than 3 intercalated water layers[6]. The hydration state of a nanolayered particle depends on the temperature and surrounding humidity. Characteristic platelet separation[6] (d=1.0, 1.2 and 1.5 nm) and transition temperatures[7] under conditions of low (~5 %) and high (~ 98 %) relative humidity have been determined for the three hydration states, respectively.

In this paper we study the macroscopic diffusion of water into weakly hydrated Na-fluorohectorite samples. These samples, obtained by dehydration of water suspensions, are dry assemblies of the nano-layered particles described above. Water diffuses inside of them through the mesoporosity in between the particles. Applying a gradient of vapor partial pressure between the two ends of quasi-dimensional samples, we study this water diffusion, at the macroscopic scale. Depending on the temperature, a particle inside the assembly is likely to swell as the water diffusion front reaches it, due to the increase in the humidity level of the surrounding

E-mail of the corresponding author: meheust@phys.ntnu.no

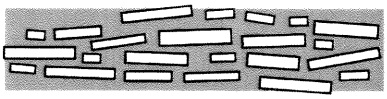

Fig. 1: 2D view of the sedimented samples' geometry. The mesoporous space is denoted by the gray shading. The clay particles have their silica sheets oriented along the horizontal direction, on average. The RMS deviation for the alignment of individual particles from this mean orientation is between 15 and 16.5° [11].

mesoporous space. Under those conditions, the diffusion of water through the mesoporous space goes along with the progression of an intercalation (or swelling) front inside the sample. We monitor the progression of this intercalation front by repeatedly recording the characteristic platelet separation, d, at distances regularly spaced from the wet sample end. The value for d is obtained from in situ wide angle X-ray scattering measurements.

Many studies of water transport in a porous medium have used NMR[8,9]. This is to our knowledge the first study of such a system using wide angle X-ray scattering.

SAMPLES

The samples were prepared in the following way. Raw fluorohectorite powder was purchased from Corning Inc. (New York). It was dissolved in deionized water; the suspension was stirred for several days. NaCl was then added in an amount ~ 10 times larger than the estimated amount of interlayer charges in the suspensions, so as to force the replacement of all intercalated cations by Na^+. This caused the suspension to flocculate. After 2 weeks of stirring, it was left to sediment, and the supernatant was removed. Excess ions were subsequently removed by placing the flocculated clay in dialysis membranes and in contact with deionized water, which was changed every second day, until a test using $AgNO_3$ showed not presence of remaining Cl^- ions. At this point, two types of samples were prepared.

(i) Part of the sediment was heated for 6 hours at 120°C. The resultant powder was grinded in a mortar. The grinded powder was then placed in X-ray glass capillaries, with a diameter 2mm and a wall thick 0.01mm. They were vibrated while filling them up so as that the compaction of the powder inside the tube be as uniform as possible. We refer to these samples as "powder samples".

(ii) Part of the sediment was suspended in deionized water again, and after stirring, water was expelled by heating up. The resulting assemblies were then cut in strips of 4mm by 47mm. We refer to these samples as "sedimented samples". In contrast to the powder samples that are isotropic, these samples are anisotropic, with a marked average alignment of the clay particles parallel to the horizontal plane[10,11] (see Fig. 1).

EXPERIMENTAL METHOD

The experiments consist in repetitive in situ measurements of the proportions of particles in the 1WL- and 2WL- hydration states, at positions regularly spaced along the sample length. This is done by positioning these points of the sample in front of a horizontal X-ray beam, and recording one-dimensional scattering spectra for each position and time.

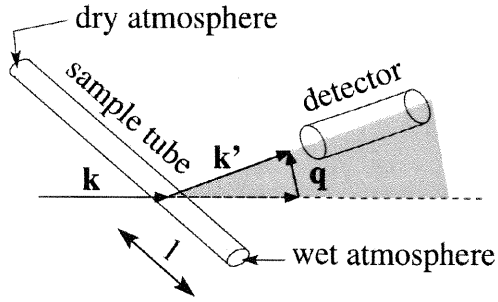

Fig. 2: Sketch of the scattering geometry, featuring the momentum of the incident photons, **k**, that of the scattered photons, **k'**, and the momentum transfer **q**. These 3 vectors are in a vertical plane (denoted by the gray shadings) in which the detectors moves to record the scattering spectra. The sample can be translated along its length so as to vary the distance l from the wet end at which the beam hits the sample.

X-ray scattering setup

Wide angle scattering (WAXS) experiments were carried out at the D12A XRD1 beamline at LNLS (the Brazilian Synchrotron Laboratory). The Si(111) two-crystal monochromator with horizontally focusing, coupled to a vertically focusing Rh-coated X-ray mirror, provided a 1x1mm² or 1x3 mm² beam with an energy E = 10.4 kV and a dispersion on the energy ΔE=E/1170. The sample was placed horizontally, with its length perpendicular to the incoming X-ray beam, and a scattering spectrum was recorded in a vertical plane, using a 3-circle Huber diffractometer and a NaI scintillation point detector. The scattering geometry is shown in Fig. 2.

Sample holder

The sample was placed on a thermally-controlled copper block, as shown in Fig. 3(a), with heat-conducting paste in between them. The temperature control setup allowed both cooling and heating of the copper block, and consisted of a Peltier element placed under the block, a thermistor to measure its temperature, and a computer-controlled PID system to adjust the Peltier's excitation to the measured temperature. The Peltier was applied a reference temperature on its side opposite to the copper block, in the form of water circulating from a regulated water bath. The temperature of the bath could be changed so as to increase the range of temperature available in the copper block. The overall precision of the temperature control system was found to be around 0.01 K.

The sample environment was also controlled in humidity. It was sealed along its length and in contact with two reservoirs at its ends. Air with a controlled humidity was circulated separately in the two reservoirs, which allowed to impose different controlled humidity levels at the sample ends, and therefore to impose a humidity gradient inside it. A picture of the sample holder as it was during the experiment is presented in Fig. 3(b). It features the sample (i) on its holder, the two pairs of plastic tubing (ii) at each end of the sample, and the temperature sensor (iii).

Experimental protocol

The experiments were initiated in the following way. Prior to the scattering measurements, the samples were maintained at

a temperature of 24°C, with dry air circulating at both ends,

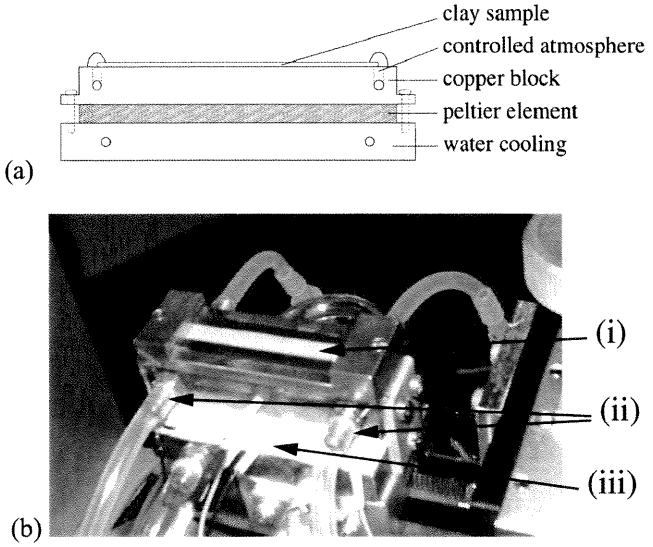

Fig. 3: (a) Side view of the sample holder, with copper block and Peltier element underneath - (b) Photo of the sample environment during an experiment carried out on a sedimented sample. The sedimented sample is isolated from the lab atmosphere by a thin kapton film glued on top of it.

long enough for all scatterers to be at equilibrium under a 1WL hydration state. Reference scattering spectra were then recorded. The spectrum labeled "1WL" in Fig. 4 is an example of such a graph. Temperature was then lowered down to 5°C. Half an hour later, thermal equilibrium was reached and we started circulating humid air at one end of the sample, imposing a humidity gradient across the length of the sample. This was defined as the initial time for water diffusion. Water penetrating the sample came in contact with particles in the 1WL state at a temperature where their equilibrium state is 2WL, hence triggering the displacement of an intercalation front in the sample, along with water diffusion.

Pressure was measured in the chambers at both ends of the samples prior to- and at the end of- the experiment. No significant pressure gradient was measured between the sample ends.

X-RAY DATA

Scattering from the nano-layered particles

The one-dimensional scattering spectra display sharp peaks for deviation angles 2θ corresponding to a Bragg reflection of some of the scatterers in the scattering volume. Apart from peaks from quartz impurities (denoted by "Q" in Fig. 4), these sharp peaks are mostly those characteristic of Bragg planes associated with the particle stacks. In Fig. 4, we show reference spectra for scattering volumes where the scatterers are in the 1WL and 2WL hydration states, and for the two types of samples. The various (00k) orders observed are indicated. Due to form factor effects, some of those orders are extinct. The spectra for the sedimented samples exhibited a large background caused by the silicon glue that we used to seal the top of the samples to the kapton. This was not observed for the powder samples, as they were inside capillary tubes.

The (001) peaks are very weak for the sedimented samples, this is due to some shadowing effect by the copper block at low angle as these samples are actually lying in a trench

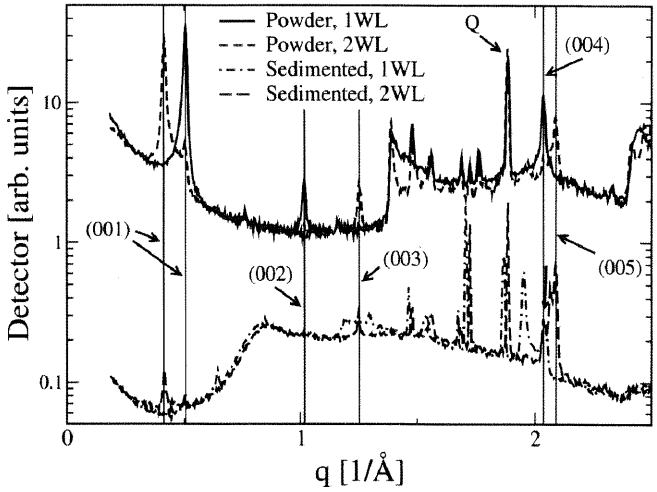

Fig. 4: Scattering spectra as a function of the momentum transfer q for powder (spectra at the top) and sedimented samples (spectra at the bottom). In each case, two spectra are shown: one recorded at a position in the sample where most of the scatterers are in the 1WL hydration state, the other at a position where most are in the 2WL state. The vertical scale is logarithmic, the spectra have been normalized arbitrarily for conveniency.

carved onto the top surface of the copper block. For that reason we had to treat higher order peaks when working with the sedimented samples, while for powder samples we could use the first order peaks, which are also the better resolved ones. For that reason we only present, in what follows, data obtained from the powder samples.

Hydration transition at a given position

Fig. 5(a) is a close view of the spectrum measured at a position l = 7.0 mm from the wet end of the sample, at different times after the diffusion process has started. The width of the beam was 3 mm. As water diffuses inside the sample, the relative humidity in the scattering volume increases. Consequently, water starts intercalating in some of the scattering particles. This is marked by a decrease in the intensity of the peak characteristic for the pure 1WL hydration state, and the appearance of an asymmetry in its shape. This asymmetry evolves into a broad and low intensity peak that appears between the 1WL and 2WL peaks. This is characteristic of the existence of scatterers in various coexisting mixed Hendricks-Teller intercalation states, with different proportions of 1WL and 2WL spacings inside scatterers[12]. These mixed states progressively blend into the shoulder of the pure 2WL peak that has started appearing after 7 hours. After ~ 17 h, only a pure 2WL peak is observed. We therefore consider that the intercalation front has penetrated in the scattering volume at t = 7.0 h, and left it 10±1 hours later.

From Fig. 5(a), we have plotted the evolution of the relative intensities for the pure 1WL and 2WL peaks as a function of time (see Fig. 5(b)). This was done by first subtracting the background from Fig. 5(a), and then normalizing the amplitudes by those observed when no random intercalation is present. From the intersection of the two curves, we infer that the time at which the mean front position is in the middle of the scattering volume is ~ 8.7±1 h, at l = 7±1 mm.

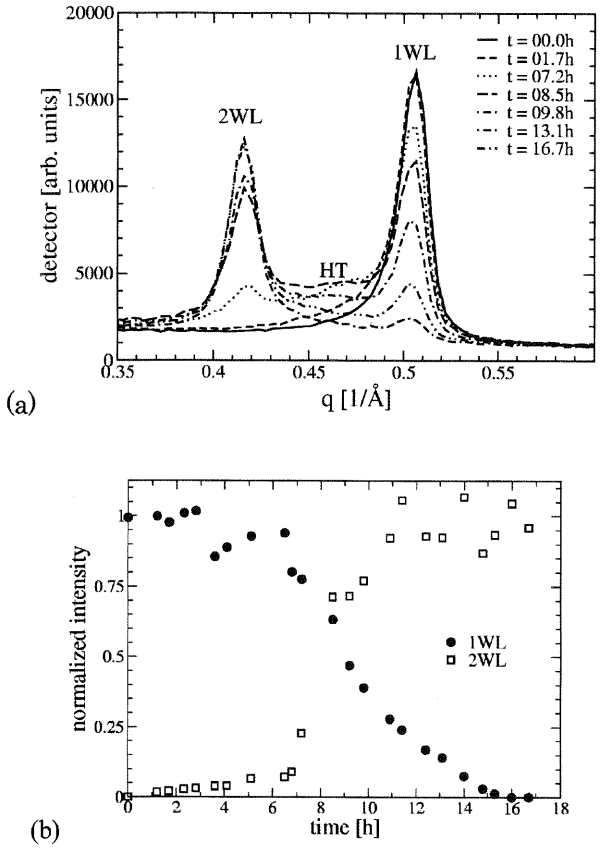

Fig. 5: (a) Close view of the scattering spectra recorded at l = 7.0 mm from the wet end of the sample, at various times between 0 and 16.7 h. As the intercalation travels through the scattering volume, the spectrum continuously moves from a pure 1WL peak to a pure 2WL peak. - (b) Normalized relative intensities of the pure 1WL and 2WL peaks in (a), as a function of time.

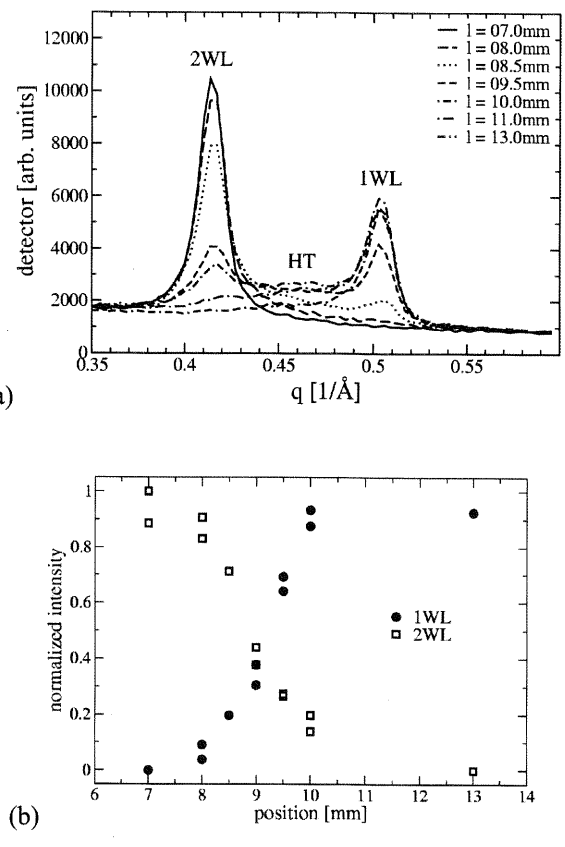

Fig. 6: (a) Close view of the scattering spectra recorded at time t = 19 h from the beginning of the water diffusion, and at several distances l from the wet end of the sample. - (b) Normalized relative intensities of the pure 1WL and 2WL peaks in (a), as a function of l. A transition from 2WL to 1WL is observed for increasing values of l.

Hydration transition at a given time

Fig. 6(a) shows the evolution of the 001 peaks at a given time, t = 19h, and for various positions l from the wet sample end. When traveling from the wet to the dry end of the sample, a similar transition is observed from the pure 2WL state to the pure 1WL state, through Hendricks-Teller states of random intercalation. In Fig. 6(b), we have plotted the relative intensities of the pure peaks in Fig. 6(a), as a function of the distance l. This provides us with a "spatial picture" of the intercalation front. However, the apparent width of the front in Fig. 6(b), around 3mm, results from the convolution of the front profile by the width of the X-ray beam, which is this case was 1mm. Hence, we can conclude that the intercalation front is quite sharp: less than 2mm in width. We also observe that the mean spatial position of the front at t = 19±1 h is l = 9.1±0.5 mm.

DISCUSSION

In each of the two previous sections, we have obtained one estimate of the intercalation front position as a function of time: 7.0±1 mm after 8.7±1 h, and 9.1±0.5 mm after 19.0±1 h. We can use the estimate of the front width (2mm) obtained in the previous section to obtain two more estimates. Supposing that the front penetrates the scattering volume at the time when the 2WL peak in Fig. 5(a) starts appearing, and taking the beam width into account, we infer a mean position of the front of 4.5±1mm after 7.2±1 h. In the same way we can assume that when the front leaves the scattering volume after 17±1 h, his mean position if 9.5±1 mm. Those 2 points, plus the initial point (0h,0mm), are plotted in Fig. 7.

How the progression of a sharp intercalation front is related to the penetration of water molecules inside the mesoporosity remains an open question. A possible mechanism would be that the vapor partial pressure in the scattering volume need to reach a certain triggering value before significant intercalation is observed. The intercalation front would then occur in the vicinity of the iso-humidity line defined by that particular value of the vapor partial pressure. Since there is no pressure difference between the two sample ends, the driving force of the water transport is the gradient of relative humidity, or water partial pressure, along the sample length. The water transport is thus expected to be a diffusive process. Let us consider a standard diffusive process with boundary conditions corresponding to our experimental configuration, that is: (i) a constant humidity difference between the two sample ends, and (ii) an initial configuration where the whole sample is at the lowest humidity. If the sample length is infinite, the solution is well known: the humidity profile has as shape defined by an error function, and its position varies as a square root function of t; so does the position of any iso-humidity line. In our experiment, due to the finite sample length, the humidity profile is expected to evolve from a step function at t = 0 to a linear profile between the two boundary values at infinite time.

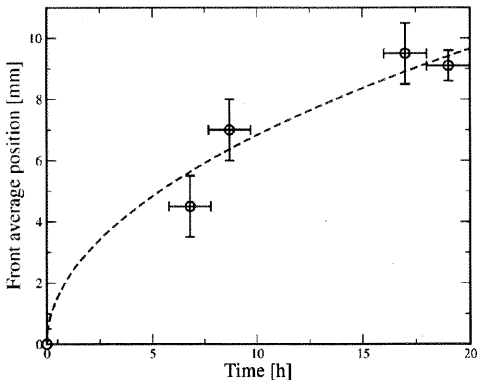

Fig. 7: Position of the mean intercalation front position as a function of time. The dashed line is a fit to the behavior expected from a standard diffusion process, where $l \sim t^{1/2}$.

Consequently, if intercalation is triggered by a threshold humidity value h_c, the intercalation front is expected to stop at the position l_c where the final humidity profile reaches h_c. Hence, the evolution of the front position as a function of time does not follow a square root law. However, at initial times, as the dry end of the sample is not "felt" by the water molecules entering at the wet end, this evolution should be close to a square root law. For the data plotted in Fig. 7, the largest probed l value is smaller than the 4th of the overall sample length, hence we believe that the standard diffusive transport through an infinite sample could be a first approximation description. The dashed line in Fig. 7 corresponds to a square root law that best fits the data; in the limit of the large uncertainties, it is consistent with the data.

Let us point out that in our experiment, water molecules that enter the sample do not remain in the mesoporosity, but intercalate into clay particles, which act as a sink for diffusing water. In addition, the subsequent swelling of clay particles modifies the configuration of the porous space, diminishing its porosity. Those two factors should have an impact on the transport, so diffusion process is expected to be slightly different from what is described by a standard diffusion equation. Obviously, uncertainties and data scarcity do not allow addressing that discrepancy in the current study.

CONCLUSION AND PROSPECTS

We have studied the diffusion of water inside quasi one-dimensional weakly-hydrated samples of Na-fluorohectorite, after imposing different humidity levels at their two ends. We used WAXS measurements to monitor the displacement of an intercalation front as water diffuses in the mesoporosity of the samples. The front was observed to be less than 2mm wide when it reached a distance l = 9mm from the wet side of the sample. In the range of l values investigated, its progression as a function of time is in first approximation consistent with a diffusive law for an infinite sample: $t^{1/2}$.

We shall carry out more extended measurements of the intercalation front position as a function of time, in order to get a better description of its displacement in time. The use of a micro-focus beam, allowing the removal of the uncertainty due to the beam size, is planned.

In order to better understand the connection between the intercalation front and the diffusion of water in the mesoporous space, we plan to precisely determine which relative humidity value (or vapor partial pressure value) triggers the intercalation of a second layer of water. This shall be done through carefully temperature- and humidity-controlled intercalation experiments on a very small amount of clay powder, with gravimetry and wide angle X-ray scattering measurements. With those measurements coupled to microfocus WAXS diffusion experiments, we eventually hope to be able to confront our data to theories for anomalous scattering[13-14], like in a recent study on related systems[15].

The results presented here were obtained on powder samples. For reasons explained earlier, sedimented samples, where clay particles exhibit a marked alignment along the horizontal plane, did not provide data where the 001 peaks could be analyzed. Another prospect of the study is to solve this technical problem in order to compare the typical diffusion time scale for those samples, as opposed to the isotropic samples.

ACKNOWLEDGEMENTS

We are grateful to the staff at LNLS for their technical support during the WAXS experiments. We also acknowledge helpful discussions with Kenneth D. Knudsen. This work is supported by the Research Council of Norway (RCN) through funding granted in the framework of the RCN Nanomat Program and the RCN Strategic University Program.

REFERENCES

1) Karivatna, P. D., Pinnavaia, T. J., Shroeder P. A. (1996) *J. Phys. Chem. Solids*, **57** (12), 1897-1906.
2) Di Masi, E., Fossum, J. O., Gog T., Venkataram, C. (2001) *Phys. Rev. E*, **64**(6), 061704.
3) Skipper, N. T., Soper, A. K., McConnell, J. D. C., Refson, K. (1990) *Chem. Phys. Lett.*, **166** (2), 141-145.
4) Skipper, N. T., Soper, A. K., McConnell, J. D. C. (1991) *J. Chem. Phys.*, **94** (8), 5751-5760.
5) Skipper, N. T., Refson, K., McConnell, J. D. C. (1991) *J. Chem. Phys.*, **94** (11), 7434-7445.
6) da Silva, G. J., Fossum, J. O., Di Masi, E., Måløy, K. J., Lutnæs, S. B (2002) *Phys. Rev. E*, **66**(1), 011303.
7) da Silva, G. J., Fossum, J. O., Di Masi, E., Måløy, K. J. (2003) *Phys. Rev. B*, **67**(1), 094114.
8) Hugues, P., McDonald, E., Halse, E., Leone B., Smith, E. (1995) *Phys. Rev. B*, **51** (17), 11332-11338.
9) Hugues, P., McDonald, E., Smith, E. (1996) *J. Mag. Res. Ser. A*, **121** (2), 147.
10) Knudsen, K. D., Fossum, J. O., Helgesen, G., Haakestad, M. (2004) *Physica B*, **352**, 247-258.
11) Méheust, Y., Fossum, J. O., Knudsen, K. D., Måløy, K. J., Helgesen, G. (2005), Preprint to be submitted.
12) Méheust, Y., Fossum, J. O., da Silva, G. J., Knudsen, K. D., Måløy, K. J. (2005), Preprint to be submitted
13) Metzler, R., Nonnenmacher, T. F. (2002) *Chem. Phys.*, **284**, 67 (2002).
14) Vargas, W. L., Palacio, L. E., Dominguez, D. M. (2003) *Phys. Rev. E*, **67**, 026314 (2003).
15) de Azevêdo, E. N., de Souza, R. E., Engelsberg, M. (2005), Preprint to be submitted.

Paper 6 (Appendix)

G. LØVOLL, B. SANDNES, Y. MÉHEUST, K. J. MÅLØY,
J. O. FOSSUM, G. J. DA SILVA, M. S. P. MUNDIM,
R. DROPPA JR. AND D. M. FONSECA

Dynamics of water intercalation fronts in a nano-layered synthetic silicate: A synchrotron X-ray scattering study

Physica B: Condensed Matter **370**, 90–98 (2005)

Available online at www.sciencedirect.com
SCIENCE DIRECT®
Physica B 370 (2005) 90–98
PHYSICA B
www.elsevier.com/locate/physb

Dynamics of water intercalation fronts in a nano-layered synthetic silicate: A synchrotron X-ray scattering study

G. Løvoll[a], B. Sandnes[a], Y. Méheust[c], K.J. Måløy[a], J.O. Fossum[b,*], G.J. da Silva[d], M.S.P. Mundim[d], R. Droppa Jr.[e], D.M. Fonseca[c]

[a]*Department of Physics, University of Oslo, Pb. 1048 Blindern, NO-0316 Oslo, Norway*
[b]*Department of Physics, University of Oslo, Sem Scelandsvei 24, 0371 Oslo, Norway*
[c]*Department of Physics, Norwegian University of Science and Technology, Høgskoleringen 5, NO-7491, Norway*
[d]*Department of Physics, University of Brasilia, Brazil*
[e]*LNLS, Campinas, Brazil*

Received 14 June 2005; received in revised form 1 September 2005; accepted 1 September 2005

Abstract

We performed synchrotron X-ray scattering studies of the dynamics of the water intercalation front in a Na–Fluorohectorite clay. Like other smectite clays, fluorohectorite particles can swell due to intercalation of successive water layers. Monitoring the intensities of Bragg peaks of the known 1- and 2-water-layer hydration states at different positions in the sample enabled spatial and temporal measurement of the proportions of the different hydration states. From experiments with controlled temperature and an imposed humidity gradient on a quasi one-dimensional powder sample, we were able to localize the intercalation front and demonstrate that the width of this front was smaller than 2 mm after penetrating 9 mm into the sample. The speed at which the intercalation front advanced through the sample during the diffusion process was shown to decrease with time. The diffraction signature of random water intercalation in the vicinity of the intercalation front also provided information on the changes in the water content of the mesopores around clay particles.

PACS: 66.30.Pa; 61.10.Eq; 61.43.Gt; 71.20.Tx

Keywords: Clay; Diffusion; Nano-layered materials; Water intercalation; WAXS

1. Introduction

Nano-layered silicates, or clays, have been widely studied and discussed as geological materials, and

*Corresponding author. Tel.: +47 22 85 64 44; fax: +47 22 85 64 22.
E-mail addresses: bsand@fys.uio.no (B. Sandnes), Jon.Fossum@phys.ntnu.no (J.O. Fossum).

0921-4526/$ - see front matter © 2005 Elsevier B.V. All rights reserved.
doi:10.1016/j.physb.2005.09.026

many industrial uses of clays are based on history and phenomenological knowledge [1,2]. Yet there are many open questions regarding static and dynamic properties of clays in relation to their nano-structure. Clays in the dispersed form are considered as plate-shaped physical colloidal particles in suspension [3]. Clays in the solid form may, on the other hand, be viewed as intercalation compounds [4] within the general context of "nano sandwiches" [5]. The fundamental building block of all clays is a layered silicate mesostructure. The silicate sheets of the so-called 2:1 smectite clays in general consist of three atomic layers: one metal hydroxide layer sandwiched in between two identical silicon tetrahedral oxide layers. The thickness of each sheet is ~1 nm with a negative surface charge and a smaller positive edge charge. In the dehydrated state these sheets stack, like decks of cards, by sharing charge-compensating cations. The ability to intercalate guest species results in a "nano-porous" material where the plate separation can to some extent be controlled. This makes fundamental studies of clay important as one of the possible building blocks in future nanotechnologies [5,6]. Clays in the dehydrated state have the ability to swell by absorbing water between the silica sheets. In this case, successive monolayers of water are absorbed between the silica sheets, thus pushing the silica sheets apart. The stepwise process of swelling originates in molecular packing effects [7–10].

In this paper we report the results of in situ X-ray diffraction experiments on the dehydrated synthetic smectite clay Na–Fluorohectorite (Na–FH) [11] at the Brazilian Synchrotron Light Laboratory (Campinas, Brazil). Na–FH has the chemical formula $Na_{0.6}(Mg_{2.4}Li_{0.6})Si_4O_{10}F_2$ per half unit cell [12], and is a polydisperse clay with platelet diameters ranging from a few nm up to ~10 μm [12]. For Na–FH, the intercalation process does not go beyond a few monolayers of water. This is due to the high negative surface charge of fluorohectorite, which is about $1.2\,e-$/unit cell. In comparison, the smectites montmorillonite and laponite have surface charges of about $0.6\,e-$/unit cell and $0.4\,e-$/unit cell, respectively [12]. Thus for both montmorillonite and laponite the basic building blocks in pure water are platelet shaped nanoparticles of about 1 nm thickness, whereas the basic particles of fluorohectorite are stacked platelet nanoparticles with thickness of about 100 nm and thus about 100 platelets in each stack [13]. Water may intercalate into the stacked particles in fluorohectorite monolayer by monolayer, up to 3 monolayers, depending on the intercalated ion [14].

For Na–FH, the intercalation of water molecules between the individual clay platelets is governed by the temperature and the vapor partial pressure in the surrounding pore-space atmosphere. Depending on the temperature and on the ambient humidity level, it has three stable hydration states [11], whose structure is denoted as consisting of 0, 1 or 2 intercalated monolayers of water (0WL, 1WL or 2WL) between the silicate platelets. The corresponding basal spacings of the nano-sandwiches are 1.0, 1.2 and 1.5 nm for the 0WL, 1WL and 2WL intercalation states, respectively [11]. Earlier studies on Na–FH have focused on structure characterization [11], and the dependence on temperature and humidity conditions of the hydration states [15]. In this study we focus on the dynamical process of water diffusing into a Na–FH material confined in a quasi one-dimensional geometry across which a humidity gradient has been imposed. The changing hydration states are monitored by measuring the Bragg peak signatures of the different water layers as the water vapor concentration in the pore space increases. These results provide information on the shape of the intercalation state profile within the sample, and on the time dependent position of the intercalation front as it progresses through the clay material. To our knowledge, it is the first time that Wide Angle X-ray Scattering is used as a local probe to study transport at the macroscale. Previous studies of such transport processes have relied on NMR techniques [16,17]. A comparison with what was observed in those studies was one of the initial motivations of the present study.

2. Experimental methods

Synchrotron X-ray scattering measurements were carried out at the D12A-XRD1 beamline at

LNLS (the Brazilian Synchrotron Laboratory). This beamline is dedicated to hard X-ray diffraction experiments and is composed basically of a vertically focusing Rh-coated X-ray mirror, a Si(1 1 1) two-crystal monochromator with horizontally sagittal focusing, a home-made theta-2theta diffractometer built in a vacuum chamber, a 3-circle Huber diffractometer, and Tl activated NaI scintillation detectors. In the present experiments, beam cross-sections of both $3 \times 1\,\mathrm{mm}^2$ and $1 \times 1\,\mathrm{mm}^2$ were used (width × height). The photon energy was 10.4 keV with $E/\Delta E = 1170$. The sample cell was mounted on the Huber diffractometer.

The clay sample was made from synthetic fluorohectorite (Corning Inc., New York). The raw material was processed by dissolving clay powder in deionized water with subsequent stirring for several days. In order to make pure sodium fluorohectorite (Na–FH) samples, an ion exchange method was used. Na^+ in the form of NaCl was added to the clay suspension in an amount of approximately 10 times the interlayer charge [12]. Due to the added salt, the suspension flocculated, and after stirring for about two weeks, the supernatant was removed. The flocculated clay was then placed in dialysis membranes, and excess ions were removed by dialysis where the deionized water was exchanged every second day. A check on this procedure was made by adding $AgNO_3$ to detect possible Cl^- ions, which would precipitate as insoluble AgCl. The flocculated sediment was then heated for 6 h at 120 °C so as to remove its water content. The resultant powder was grinded in a mortar, which destroyed the clusters inherited from the earlier particle flocculation.

The clay sample was prepared for the synchrotron experiments by filling Na–FH powder in an X-ray glass capillary. The tube was 2 mm in diameter with a wall thickness of 0.01 mm and was open at both ends. A humidity- and temperature-controlled sample holder was custom-made for the experiments (Fig. 1). The capillary containing the clay powder was attached to the temperature-controlled copper block using heat conducting paste.

During the experiment the temperature of the sample holder was measured close to the sample

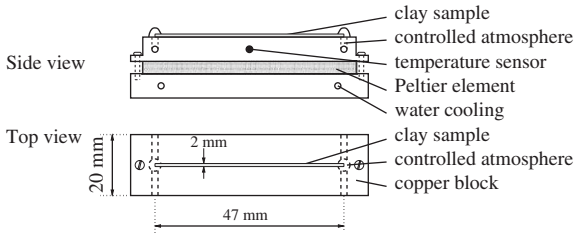

Fig. 1. Side and top view of the humidity- and temperature-controlled sample holder. A humidity gradient was imposed by exposing each end of the sample to different controlled humidity levels.

centrally in the copper block using a thermistor sensor. Temperature control of the sample was achieved by mounting the copper block on Peltier heating/cooling elements (see Fig. 1). A PID control program updated the excitation of the Peltier elements according to the measured temperature feedback signal. A variable temperature heat sink was provided for the Peltier elements by circulating water from an additional water temperature regulator through channels drilled in the lower copper block indicated in the figure. The temperature control system maintained the measured temperature, T_{sample}, constant to within 0.01 K in the relevant temperature range.

A humidity gradient was imposed across the sample by exposing the two open ends of the capillary tube to chambers with different humidities. The humidity levels were controlled by circulating air with controlled humidity through channels drilled at opposite sides of the sample holder (see Fig. 1). In the experiments presented here, one end was kept dry by filtering air through silica gel, while the other end was kept at 99% RH by circulating air above a saturated K_2SO_4-water solution.

The sample holder was mounted on an xyz-stage for precise and reproducible positioning of the sample in the beam path. The differential pressure between the opposite chambers was measured during the experiment to ensure that no pressure gradient existed that would influence the diffusion process. Relative humidity sensors were placed close to the outlet air

channels as a check on the imposed humidity gradient.

Prior to the experiment, the sample was maintained at equilibrium with all clay particles in the same intercalation state: 1WL at $T_{\text{sample}} = 24\,^{\circ}\text{C}$. Reference diffraction spectra were taken, and the temperature was subsequently lowered to 5 °C with dry air circulating at both ends of the sample. Thermal equilibrium was reached, and 30 min later the humidity gradient was imposed by circulating saturated air at one end of the sample. This moment marks the start of the diffusion/intercalation experiment, $t \equiv 0$.

The water vapor supplied at the humid side starts to penetrate the sample by diffusing through the pore space between the clay particles. As the pore space vapor concentration increases due to this diffusion, a subsequent process of water intercalation into the individual stacked platelet clay particles is triggered (at this temperature the equilibrium hydration state is 2WL for sufficiently high ambient humidity). By collecting diffraction spectra at different times and distances l from the humid side of the sample we could follow the dynamics of the intercalation front in the sample. Fig. 2 shows the scattering geometry including a cross-section of the sample, the incoming wave vector $\vec{k}$, the scattered wave $\vec{k'}$ and the scattering vector $\vec{q} = \vec{k'} - \vec{k}$. The direction of the diffusion process is along the length of the capillary cylinder illustrated in the top view in Fig. 2.

3. Results and discussion

3.1. Platelet separation and water intercalation

Fig. 3(a) illustrates one-dimensional diffraction spectras measured with the Na–FH powder in different states of hydration. The solid line shows the clay powder with one water layer intercalated taken at time $t = 0.0\,\text{h}$ ($T_{\text{sample}} = 5\,^{\circ}\text{C}$). The dashed line shows the diffraction spectrum at the same position ($l = 7.0\,\text{mm}$) taken at $t = 17.1\,\text{h}$, after a second water layer had intercalated the clay particles. Several orders of Bragg peaks for both the 1WL and 2WL hydration states are identified and labeled in the figure. We can also identify a quartz peak (labeled Q) and a peak which is due to scattering related to periodicity along a direction different from that of the stacking direction [18] (labeled "inplane"). Fig. 3(b) shows a close up view of the position of the (0 0 1) Bragg peak with one and two intercalated water layers. In our data the peaks were found at 0.51 and 0.41 Å^{-1} for the 1WL and 2WL peaks, respectively, which corresponds to platelet separations 12.4 and $15.2 \pm 0.3\,\text{Å}$. The results are in good agreement with previous measurements on similar pressed and sedimented Na–FH samples [11,15,20].

No spontaneous transition from the 1WL hydration state to the 2WL state was observed as the sample temperature was reduced from 24 °C to 5 °C before the external humidity difference was

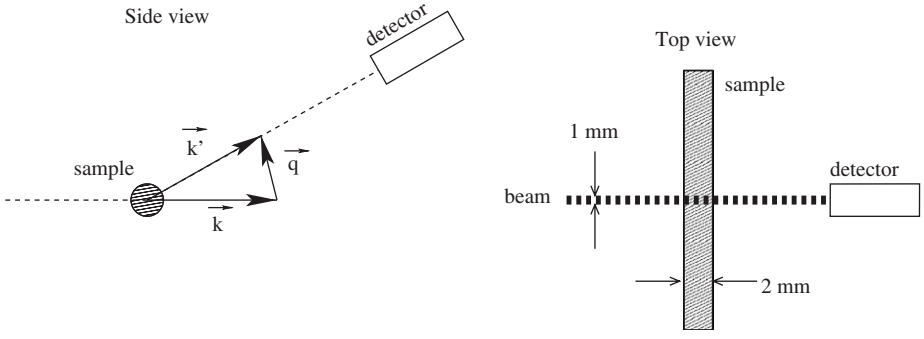

Fig. 2. Sketch of the scattering geometry, showing a cross-section (side view) of the clay powder sample, the incoming wave vector $\vec{k}$, the scattered wave vector $\vec{k'}$ and the scattering vector $\vec{q}$. The right-hand side of the figure shows a top view of the sample contained in the capillary tube, where the diffusion process occurs along the length of the tube as a result of the difference in humidity level imposed on the opposite ends of the cylinder. The horizontal width of the X-ray beam was alternated between 3 and 1 mm (see text).

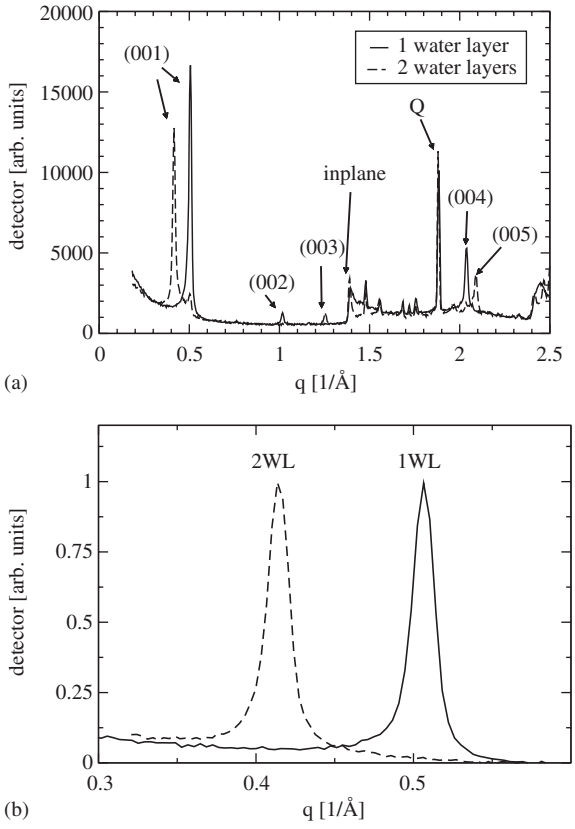

Fig. 3. (a) Diffraction spectras for the Na–FH sample with 1 and 2 intercalated water layers. The "inplane" peak is due to scattering related to periodicity along a direction different from that of the stacking direction. (b) Close up view of the normalized (0 0 1) Bragg peak for 1 and 2 intercalated water layers (WL).

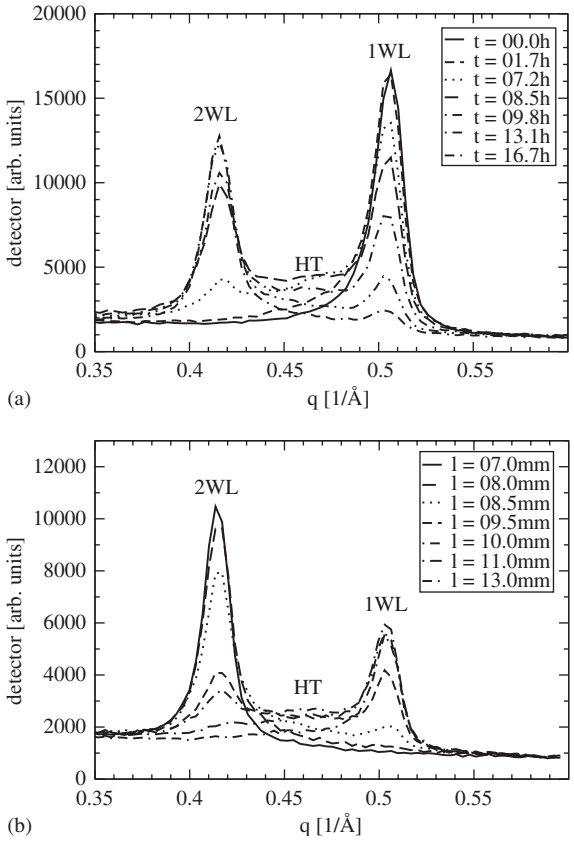

Fig. 4. Intercalation dynamics during water vapor diffusion in the Na–FH powder confined in the capillary tube. (a) Time evolution for the (0 0 1) peaks at position 7 mm from the wet side of sample (beam width = 3 mm). (b) Position scan for the (0 0 1) peak near the wet side of the sample. The series were obtained at a "fixed" time when water had diffused well into the sample, at about 20 h from the start of the experiment (beam width = 1 mm). The broad area between the two Bragg peaks labeled "HT" is the signature of grains with "Hendricks–Teller" mixed-intercalation states [19,21].

imposed. (Comparison of reference scan with scan taken at $t = 0.0$ h). This indicates that the water vapor concentration initially in the pore space is not high enough to ensure immediate transition to the 2WL state. This water has to enter from the boundaries of the sample.

3.2. Dynamics of the intercalation front

By recording diffraction spectra at different positions and at different times we are able to monitor the evolution of the different hydration states of the clay particles as water diffuses into the sample. Fig. 4 shows the evolution of the (0 0 1) Bragg peak during water diffusion. Fig. 4(a) shows the (0 0 1) peak as a function of time measured close to the humid side of the sample at $l = 7.0$ mm. Fig. 4(b) shows the diffraction scans measured at different distances l from the humid side of the sample at a fixed time $t \sim 19$ h after the start of the experiment.

If we look closer at the time evolution in Fig. 4(a), we see that it follows a scheme consistent with transient Hendricks–Teller mixed-intercalation states during the hydration transition [19]. We start the experiment with a pure 1WL hydration

state, i.e., all particles in the scattering volume are in the pure 1WL hydration state. After some time (~1.5 h in this case), the shape of the Bragg peak changes, it becomes asymmetric. The shoulder appearing on the left-hand side of the peak is the sign that Hendricks–Teller states of mixed intercalation [21] with a small proportion of 2 water layers-spacing in the nano-stacks have appeared. We interpret this as a signature of increasing humidity in the scattering volume as the diffusion front enters the mesoporosity around the clay scatterers. As time passes, the asymmetry of the (0 0 1) 1WL Bragg peak becomes more pronounced, and a broad intensity distribution develops in-between the positions for the 1WL and 2WL peaks. This means that a large number of clay particles in the scattering volume contain a significant proportion of 2WL spacings. After ~7 h, the (0 0 1) Bragg peak for the 2WL intercalation state has developed, i.e., some of the clay particles in the scattering volume have reached a pure 2WL hydration state. The broad distribution in-between the pure 1WL and 2WL peaks, characteristic of a coexistence of various mixed-intercalation states, remains until all scatterers are in the 2WL hydration state (the 1WL peak has then completely disappeared). At this stage (~17 h) we can say that the intercalation front has passed the scattering volume.

If we look at the spatial data in Fig. 4(b), we observe a similar pattern of transition between intercalation states, now at a fixed time where the length of the sample is scanned. In the position closest to the humid side ($l = 7.0$ mm) all particles in the scattering volume are in the 2WL hydration state. Moving away from the humid side we first observe a less symmetric 2WL peak indicating traces of random intercalation states, at $l = 8.0 \pm 0.5$ mm the 1WL peak appears in the scattering volume, and it becomes more intense as we move away from the humid side of the sample. At $l = 11.0 \pm 0.5$ mm the 2WL peak was no longer in the scattering volume.

Based on the peak intensities of the two (0 0 1) peaks shown in Fig. 4 we could measure the relative (0 0 1) peak intensities for the two intercalation states as function of time and space. We calculated the relative intensity of the (0 0 1) Bragg peak by subtracting the background and normalizing with the measured peak intensities when no random intercalation was present. Fig. 5 shows the relative peak intensities for the 1WL and 2WL (0 0 1) Bragg peak as function of time from the start of the experiment (a), and as function of distance l from the humid end of the sample (b).

The time evolution for one position plotted in Figs. 4(a) and 5(a) provides some information on the speed at which the intercalation front advances through the clay sample. In this case the width of the beam is 3 mm, and the center of the scattering volume is 7.0 mm from the high humidity side of the sample. The intercalation front is here defined as the boundary of the region where pure 2WL

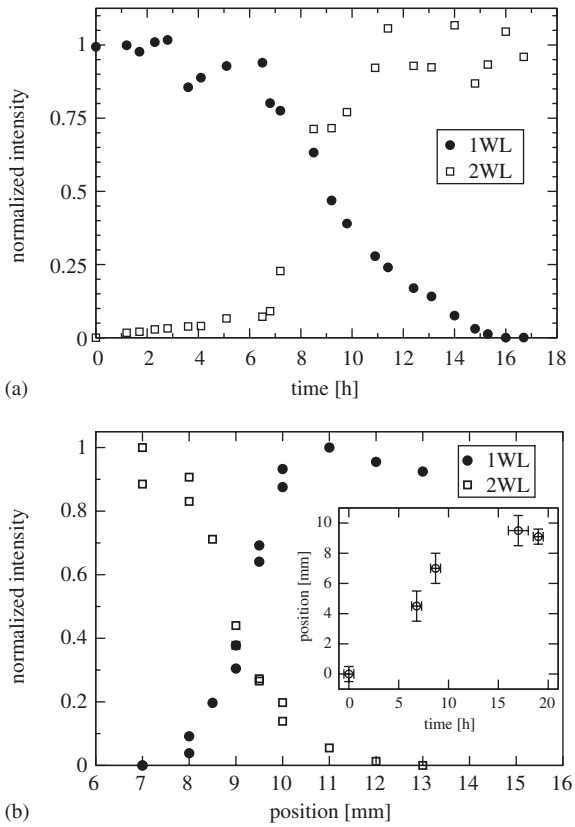

Fig. 5. Normalized 1 and 2WL peak intensities during the hydration transition in the Na–FH sample: (a) as function of time at $l = 7$ mm from the wet side of the sample; (b) as a function of distance l from the wet end of the sample at $t \approx 19$ h from the start of the experiment. Inset: Position of the intercalation front plotted as a function of time.

hydration states exist and its position is measured by monitoring the appearance of a distinct 2WL peak in the diffraction spectra. The intercalation front is observed to reach the scattering volume at $t = 6.8 \pm 0.5$ h, it progresses through, and leaves the scattering volume at $t = 17 \pm 1$ h. The intercalation front, head and tail included, has thus used an estimated ~10 h to move through the 3 mm scattering volume at this particular position ($l = 7.0$ mm).

Fig. 5(b) shows the normalized intensities of the 1WL and 2WL Bragg peaks as a function of distance from the high humidity side of the sample measured approximately 19 h after the start of the experiment. The (horizontal) width of the beam was in this case reduced to 1 mm in order to localize the front with higher resolution. The figure reveals a relatively sharp intercalation front, where the transition from the 1WL hydration state to the 2WL hydration state occurs within ~3 mm of the plot (between 8 and 11 mm). Considering that this apparent width results from a convolution of the 1 mm beam with the front profile, we conclude that the actual width of the intercalation front is smaller than 2 mm.

From the transition profiles in Fig. 5(b) we can locate the position of the center of the intercalation front at 9.1 ± 0.5 mm at time $t = 19.0 \pm 0.5$ h. Additional position/time data points are given by the estimated times for when the front entered and left the scattering volume positioned at 7 mm as discussed earlier (see e.g. Fig. 5(a)). The corresponding positions are given by adding half the front width to the edges of the scattering volume (assuming the front width remains ~2 mm during the experiment). A last data point can be obtained from 5(a) by placing the mid-point of the transition occurring at 8.7 ± 0.5 h in the center of the scattering volume ($l = 7.0 \pm 0.5$ mm). The inset in Fig. 5(b) shows these intercalation front positions plotted as a function of time, and although considerable uncertainty is associated with these data points, the figure indicates that the speed of the intercalation front decreases with time as it penetrates further into the sample.

The diffusion of water vapor in the pore space between the clay particles is expected to result in a concentration profile that gradually becomes flatter with time, such that after some time it appears stretched out between the boundaries of the sample. This is suggested both by our observation of traces of mixed-intercalation states over 5 h ahead of the intercalation front, and by other studies on comparable systems [16,17]. The expected low gradient in the vapor concentration is in contrast to the observed "sharpness" of the intercalation front after ~19 h, which suggests that the platelet intercalation front does not follow the diffusion gradient of vapor in the pore space. At this point the intercalation front is confined within 2 mm of the sample, while the diffusion profile necessarily stretches from the edge of the sample and beyond the edge of the intercalation front at ~11 mm.

There can be several mechanisms that give rise to such an abrupt transition between hydration states as a function of position within the clay sample. One possible scenario is that the intercalation process depends sensitively on the vapor partial pressure, such that a relatively small increase in the vapor concentration at some point would produce a large increase in the nucleation rate of new platelet intercalations. Thereby only a small number of intercalation events would take place until the vapor concentration in the surrounding pore space atmosphere reaches what appears as a critical value. The intercalation front would in this case advance at the speed of this concentration level which is governed by the vapor diffusion in the porous medium and availability of water. Our observation of an intercalation front speed that decreases with time is as such consistent with a diffusion related process characterized by a length/time relationship of $l \propto t^{1/2}$. Such a square root law is expected for a displacement described by a standard diffusion equation in a geometry where the sample has an infinite length. For initial times, where the diffusion front is far away from the dry sample end, it can be considered as a good approximation for a standard diffusion process along a finite sample.

For the diffusion/intercalation process as a whole, we propose that water diffuses through the pore space in the clay powder at a rate governed by the effective diffusion constant of

water vapor in air confined within the porous material. The diffusion front is followed by a much sharper intercalation front where a second monolayer of water molecules penetrates the stacked platelet structure of the Na–FH particles. The diffusive transport of water vapor in the pore space is modified by the intercalation process since the clay particles act as a sink for the supplied water during intercalation. Water intercalation causes the clay to swell, and this is also expected to influence the diffusive transport since it results in a reduction of the pore space volume available for diffusion.

The exact nature of the intercalation process, specifically how the rate of new intercalation events depends on the combined effects of temperature and vapor partial pressure, remains to be investigated further. Also, a subject for further studies is to determine quantitatively the relationship between the vapor transport in the porous network and the intercalation process. In other words, to define a characteristic law that describes the macroscopic spatial diffusion/intercalation process as outlined in the previous paragraph.

4. Conclusion

The spatial dynamics of water intercalation in dry Na–Fluorohectorite clay was studied using synchrotron X-ray diffraction. Na–FH powder contained in a capillary tube was temperature-controlled and exposed to humid and dry atmospheres on opposite ends. The intercalation of water between the clay platelets as water diffused though the sample was monitored by measuring the known Bragg peaks of the 1 and 2 intercalated water layer states as functions of space and time. In these experiments we were able to localize and follow the intercalation front and demonstrate that the front was less than 2 mm wide after penetrating ~9 mm into the sample ~19 h after the start of the experiment. One possible explanation for the observed abrupt transition between hydration states is that the intercalation process depends sensitively on the vapor partial pressure in the pore space. We also see the signature of random water intercalation in the intercalation front, which is manifested as a broad Hendricks–Teller peak between the known Bragg peaks in the diffraction spectrum.

Future studies should focus on prolonged measurements of both the intercalation front and the vapor diffusion profile within the clay material as a function of time at different positions within the sample. Improved spatial resolution could be achieved through the use of a synchrotron microfocus system. A more detailed understanding of the intercalation process could be gained from scattering experiments on small samples exposed to well controlled and adjustable vapor concentrations.

Acknowledgements

We gratefully acknowledge technical support from the LNLS staff while performing the scattering experiments, as well as K.D. Knudsen for helpful discussions. This research is supported by the RCN (The Research Council of Norway) through the Synchrotron Program, Project number 138368/V30, through the RCN NANOMAT program, project numbers 158541 and 163558/S10, through the RCN SUP (Strategic University Program) number 115185/420, and also through the RCN projects 148865/V30 and 152426/V30.

References

[1] B. Velde, Introduction to Clay Minerals, Chapman & Hall, London, 1992.
[2] R.E. Hummel, Understanding Materials Science, Springer, New York, 1998.
[3] H. van Olphen, An Introduction to Clay Colloid Chemistry, Interscience, New York, 1977.
[4] S. Solin, Annu. Rev. Mater. Sci. 27 (1997) 89.
[5] C. Oriakhi, Chem. Britain 34 (11) (1998) 59.
[6] J.O. Fossum, Soft Condensed Matter: Configurations, Dynamics and Functionality, Kluwer Academic, Amsterdam, 2000.
[7] J. Israelachvili, Intermolecular and Surface Forces, second ed., Academic, London, 1992.
[8] N.T. Skipper, A.K. Soper, J.D.C. McConnell, K. Refson, Chem. Phys. Lett. 166 (2) (1990) 141.
[9] N.T. Skipper, A.K. Soper, J.D.C. McConnell, J. Chem. Phys. 94 (8) (1991) 5751.

[10] N.T. Skipper, K. Refson, J.D.C. McConnell, J. Chem. Phys. 94 (11) (1991) 7434.
[11] G.J. da Silva, J.O. Fossum, E. DiMasi, K.J. Måløy, S.B. Lutnæs, Phys. Rev. E 66 (1) (2002) 011303.
[12] P.D. Karivatna, T.J. Pinnavaia, P.A. Schroeder, J. Phys. Chem. Solids 57 (12) (1996) 1897.
[13] E. DiMasi, J.O. Fossum, T. Gog, C. Venkataraman, Phys. Rev. E 64 (6) (2001) 061704.
[14] J.O. Fossum, E. Gudding, D.D.M. Fonseca, Y. Méheust, E. DiMasi, T. Gog, C. Venkataraman, Energy 30 (6) (2005) 873.
[15] G. da Silva, J. Fossum, E. DiMasi, K. Måløy, Phys. Rev. B 67 (2003) 094114.
[16] P. Hughes, P. McDonald, M. Halse, B. Leone, E. Smith, Phys. Rev. B 51 (17) (1995) 11332.
[17] P. Hughes, P. McDonald, E. Smith, J. Magn. Reson. Ser. A 121 (2) (1996) 147.
[18] Y. Méheust, J.O. Fossum, K.D. Knudsen, K.J. Måløy, G. Helgesen, Mesostructural changes in a clay intercalation compound during hydration transition, 2005, preprint to be published.
[19] Y. Méheust, J.O. Fossum, G.J. da Silva, K.D. Knudsen, K.J. Måløy, G. Helgesen, Hendricks–Teller analysis of the intercalation transition in a fluorohectorite clay, 2005, preprint to be published.
[20] K. Knudsen, J. Fossum, G. Helgesen, M. Haakestad, Phys. B 352 (2004) 247.
[21] S. Hendricks, E. Teller, J. Chem. Phys. 10 (3) (1942) 147.

Paper 7 (Appendix)

J. O. FOSSUM, Y. MÉHEUST, K. P. S. PARMAR, K. D. KNUDSEN, K. J. MÅLØY AND D. M. FONSECA

Intercalation-enhanced electric polarization and chain formation of nano-layered particles

Europhysics Letters **74**, 438–444 (2006)

EUROPHYSICS LETTERS 1 May 2006

Europhys. Lett., **74** (3), pp. 438–444 (2006)
DOI: 10.1209/epl/i2005-10541-0

Intercalation-enhanced electric polarization and chain formation of nano-layered particles

J. O. Fossum[1], Y. Méheust[1], K. P. S. Parmar[1], K. D. Knudsen[2], K. J. Måløy[3] and D. M. Fonseca[1]

[1] *Department of Physics, NTNU - Hoegskoleringen 5, NO-7491 Trondheim, Norway*
[2] *Physics Department, IFE - P.O. Box 40, NO-2027 Kjeller, Norway*
[3] *Physics Department, UiO - Postboks 1048 Blindern, NO-0316 Oslo, Norway*

received 21 December 2005; accepted in final form 28 February 2006
published online 22 March 2006

PACS. 61.10.Eq – X-ray scattering (including small-angle scattering).
PACS. 82.70.Dd – Colloids.
PACS. 83.80.Gv – Electro- and magnetorheological fluids.

Abstract. – Microscopy observations show that suspensions of synthetic and natural nano-layered smectite clay particles submitted to a strong external electric field undergo a fast and extended structuring. This structuring results from the interaction between induced electric dipoles, and is only possible for particles with suitable polarization properties. Smectite clay colloids are observed to be particularly suitable, in contrast to similar suspensions of a non-swelling clay. Synchrotron X-ray scattering experiments provide the orientation distributions for the particles. These distributions are understood in terms of competing i) homogenizing entropy and ii) interaction between the particles and the local electric field; they show that clay particles polarize along their silica sheet. Furthermore, a change in the platelet separation inside nano-layered particles occurs under application of the electric field, indicating that intercalated ions and water molecules play a role in their electric polarization. The resulting induced dipole is structurally attached to the particle, and this causes particles to reorient and interact, resulting in the observed macroscopic structuring. The macroscopic properties of these electro-rheological smectite suspensions may be tuned by controlling the nature and quantity of the intercalated species, at the nanoscale.

In this letter we study colloidal suspensions of electrically polarizable particles in insulating fluids. When such suspensions are subjected to an external electric field, usually of the order of 1 kV/mm, the particles become polarized, and subsequent dipolar interactions are responsible for aggregating a series of interlinked particles that form chains and columns parallel to the applied field. This structuring occurs within seconds, and disappears almost instantly when the field is removed [1–5]. It coincides with a drastic change in rheological properties (viscosity, yield stress, shear modulus, etc.) of the suspensions [6], which is why they are sometimes called electrorheological fluids (ERFs). This makes the mechanical behavior readily controllable by using an external electric field [1–7]. Particle size has a quite diverse impact on the behavior of ERFs [8]. The nature of the insulating fluid and of the colloidal particles determines the electrorheological behavior of the suspensions. The mechanism is not fully understood yet, but

it is mainly triggered by the so-called interfacial polarization, and requires electric anisotropy of the particles [9]. Consequently, particle shape [10] and surface properties [11] can also be critically important, as dielectric properties largely depend on them.

Clays as traditional material have played an important role throughout human history. Their common modern uses include nano-composites, rheology modification, catalysis, paper filling, oil well-drilling and -stability, etc. [12]. The basic structural unit of so-called 2 : 1 clays is a 1 nm-thick platelet consisting of two tetrahedral silica sheets sandwiching one octahedral silica sheet. Smectites are 2 : 1 clays for which platelets carry a moderate negative surface charge on their plane surfaces. This charge is sufficiently large so that individual platelets are able to stack by sharing cations, and moderate enough so as to allow further intercalation of water molecules into the resulting "decks of cards"-like smectite particles. Natural smectite clay particles dispersed in salt solutions have been studied for decades [12], and recently there has been a growing activity in the study of complex physical phenomena in synthetic smectites [13]. Much effort has gone into relating the lamellar microstructure of smectite clay-salt water suspensions to their collective interaction and to resulting macroscopic physical properties, such as phase behavior and rheological properties [13–21]. Nematic liquid crystalline-like ordering in smectite systems has been characterized by the observation of birefringent domains with defect textures [14, 16, 18, 19] or by Small-Angle X-Ray Scattering [16, 18].

Wide Angle X-Ray Scattering (WAXS) studies of the well-characterized synthetic smectite clay fluorohectorite, in water suspensions [17], show that fluorohectorite particles contain about 80 1 nm thick platelets. Due to their large structural surface charge ($1.2\,e^-$/unit cell [22]), fluorohectorite stacks remain intact when suspended in water, in contrast to those of laponite ($0.4\,e^-$/unit cell) or of the natural clay montmorillonite. The natural smectite illite ($0.9\,e^-$/unit cell [23]) on the other hand, behaves much like fluorohectorite in this respect [24]. For fluorohectorite, the number of mono-layers of water that can be intercalated into the stacks, depending on temperature and relative humidity, has been mapped for hydration and dehydration by means of synchrotron X-ray scattering techniques [25]. However, the spatial configuration for the intercalated water molecules, with respect to the silica sheets and to the intercalated cations, is not precisely known yet. We show in this letter that the strong electro-rheological behavior exhibited by suspensions of smectite clay particles in silicon oil can be attributed to the intercalated species.

We studied four types of smectite suspensions in oil: Firstly, three suspensions based on fluorohectorite (see [17] for its origin and chemical formula), and secondly, a mixed natural quick clay from the Trondheim region in Norway. The three types of fluorohectorite samples differ by the nature of the exchangeable cation, which is either mono- (Na^+), di- (Ni^{2+}) or tri-valent (Fe^{3+}). These synthetic samples are polydisperse with wide distributions of sizes (diameter up to a few micrometers, stack thicknesses around 100 nm) and aspect ratios. The quick clay is far less well characterized than the synthetic clays, although from preliminary X-ray diffraction analysis we know that this mixed natural clay contains considerable amounts of illite and other natural smectite particles, in addition to the non-smectite clay kaolinite. The samples were initially prepared at ambient temperature by adding 1.5% by weight of clay particles to the silicon oil Rotitherm M150 (viscosity 100cSt at 25 °C) , and subsequently removing the heavier particles ($\gtrsim 10\,\mu$m) by sedimentation, which modified only marginally the suspensions' particle density.

When placed between copper electrodes between which a sufficiently strong electric field is applied, the four types of samples exhibit the dipolar chain formation characteristic of ERFs (see fig. 1). The sample cell used for these observations consisted of two parallel and identical 1/2 mm thick copper electrodes separated by a gap of 2 mm and glued onto a transparent quartz glass microscope slide. The gap between the electrodes was closed at its ends by

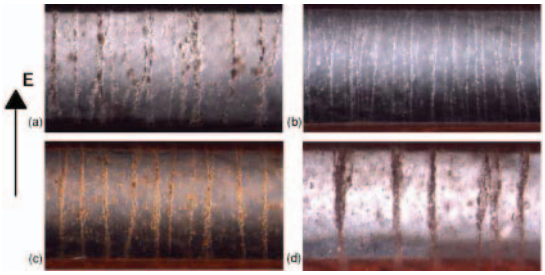

Fig. 1 – Microscope images of electrorheological chain formation in oil suspensions of smectite clays. (a) Na-fluorohectorite. (b) Ni-fluorohectorite. (c) Fe-fluorohectorite. (d) Natural quick clay.

a non-conducting plastic material. The top part of the cell was open, and the sample cell was mounted horizontally, with the microscope slide flat down. A small volume (< 1 ml) of the prepared sample was added and studied at ambient temperatures. The sample was illuminated from below, and observed from above in a stereomicroscope. An electric field $E \sim 500$ V/mm was applied between the copper electrodes, and the changes in the sample were recorded by means of a digital camera connected to a PC. The process resulted in all clay particles being part of the electrorheological chain bundles after 10 to 20 s, and no motion being visible within the sample in less than 1 min. The critical electric field necessary to trigger the electrorheological behavior was found to be $E_c \simeq 400$ V/mm.

The procedure was then repeated using a suspension of kaolinite, a 1 : 1 natural clay which, in contrast to smectite clays, does not spontaneously intercalate cations and water molecules in between its silica sheets. Kaolinite particles in their natural state have been reported in the literature to exhibit a weak electrorheological behavior when suspended in a silicon oil [26]. Microscopy observations of kaolinite suspensions with the same density as the smectite suspensions exhibited electrorheology, but only for $E \gtrsim 2$ kV/mm. They formed with characteristic time 10 to 100 times larger than that of the smectite suspensions. Furthermore, the bundle structure formed by the kaolinite suspensions appeared much less ordered than those observed with the smectites.

Relative orientations of the smectite particles inside the electrorheological chains were determined using synchrotron X-ray scattering experiments: chain and column formations were observed by means of a video camera, while simultaneously recording X-rays scattered

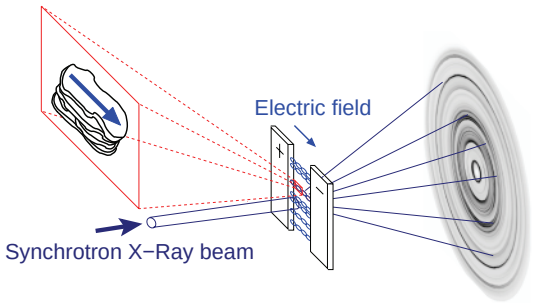

Fig. 2 – Sketch of the X-Ray scattering experiments. Corresponding diffractograms are shown in figs. 3(b) and (c). The magnified area shows a single nano-layered clay particle inside a dipolar chain; the arrow indicates the direction of the dipole moment induced by the external electric field.

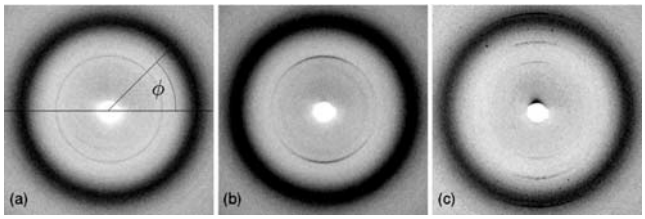

Fig. 3 – Central regions of two-dimensional WAXS images of the electrorheological samples. (a) Suspension of Na-fluorohectorite at $E \sim 0$. (b) Suspension of Na-fluorohectorite for $E \sim 500\,\mathrm{V/mm} > E_c$. (c) Natural quick clay for $E \sim 500\,\mathrm{V/mm} > E_c$.

by the clay crystallites. These experiments were performed at the Swiss-Norwegian Beamlines (SNBL) at ESRF (Grenoble, France), using the WAXS setup with a 2D mar345 detector at beamline BM01A. The sample cells used for these experiments differ from those described above in that the electrodes were placed vertically, the cells being closed at the bottom and with their top open, which allowed to partly fill the cell with sample from above. A sketch of the experiment is shown in fig. 2.

Figure 3 shows three different two-dimensional diffractograms. Figure 3(a) is obtained from a suspension of Na-fluorohectorite prior to the application of an electric field. Each lamellar clay particle may be regarded as a single crystallite, and the particles are randomly oriented inside the sample, so the image is isotropic. The broad outermost ring is due to scattering from the silicon oil (characteristic length $d \sim 6.9$–$7.9\,\text{Å}$), whereas the narrow symmetric ring at lower scattering angles is the (001) Bragg peak from the lamellar clay stacks with 1 water layer intercalated ($d \sim 12.3\,\text{Å}$). In the presence of an electric field (fig. 3(b)), in contrast, the (001) Bragg peak has become anisotropic due to particle orientation in the field. In addition, the number of water layers intercalated was determined directly from the positions of the Bragg peaks in reciprocal space (as in [27]). Figure 3(c) shows the diffractogram of a suspension of natural quick clay, for $E > E_c$. Three anisotropic scattering rings are visible: the 1st order of illite ($d \sim 10.1\,\text{Å}$), and the 1st ($d \sim 14.28\,\text{Å}$) and 2nd order of an another smectite clay. The whole diffractogram (not shown here) also reveals the 3rd-order ring of illite, and the 3rd- and 4th-order rings of the other smectite clay. All the visible diffraction rings correspond to diffraction by smectite clays and are anisotropic. Figure 4(a) shows how the intensity of circular scattering rings such as those presented in fig. 3 evolve as a function of the azimuthal angle, between 0 and 360°. In the case of fluorohectorite, we have considered the ring at a radial position corresponding to the first-order Bragg peak for the clay stack [27], which is characteristic of 1 mono-layer of intercalated water at ambient temperatures ($d \sim 12.4\,\text{Å}$ for the Na-fluorohectorite). For the natural sample, we have considered the lowest-order Bragg peak of illite (see fig. 3(c)). The scattered intensity at a given azimuthal angle is proportional to the number of particles that meet the Bragg condition for that angle, so the shapes of the scattered intensities in fig. 4(a) provide the orientation distributions of clay particle orientations inside the chains and columnar structures. For $E \sim 0$, the intensities are independent of ϕ (except for the experimental noise). For $E > E_c$, the azimuthal positions of the maxima along the plots in fig. 4(a) demonstrate that the preferred orientation of the clay particles is with the lamellar stacking plane parallel to the direction of the electric field. Since the collective dipolar interactions between particles align their dipole moments with the electric field, the preferred direction of polarization for each stacked particle could also be inferred, as indicated in the insert of fig. 2: it is parallel to the silica sheets.

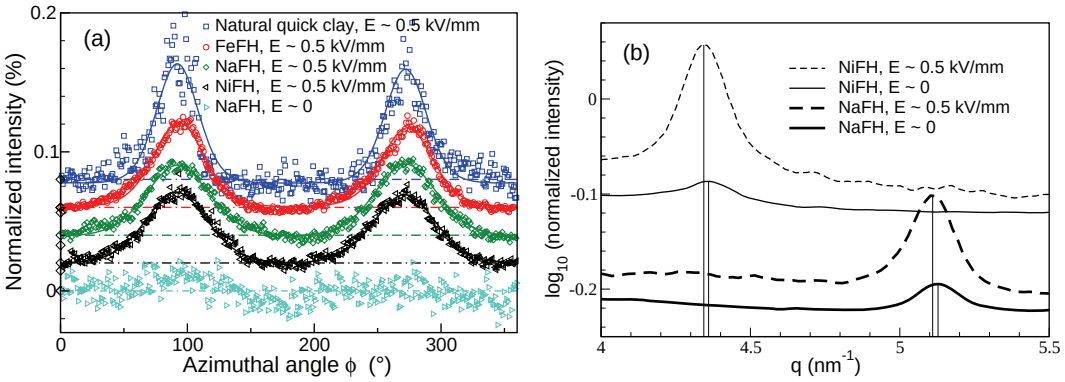

Fig. 4 – (a) Dependence of the intensity of circular scattering rings on the azimuthal angle ϕ: data and corresponding theoretical fits. (b) Scattering lines along the q direction for the Na- and Ni-fluorohectorite samples in the 1WL hydration state (corresponding, respectively, to $d = 2\pi/q = 12.26\,\text{Å}$ and $d = 14.41\,\text{Å}$ for $E \sim 0$): a systematic increase of the platelet separation inside the clay particles occurs under application of the electric field, and results in a shift of the corresponding diffraction peak. In (a) and (b), the plots have been imposed a different vertical offset, for clarity.

Colloids that make "good" electrorheological particles are known to possess two important properties, which allow them to not only polarize, but also to rotate under the effect of the electric field: i) their interfacial polarizability is important, and ii) they are electrically anisotropic [9, 28]. In the case of our platelet-shaped nano-layered smectite clay particles, particle polarization occurs along their silica sheet. A fine monitoring of the scattering line along q shows that the application of the electric field results in a subtle increase in the characteristic separation between adjacent platelets inside clay particles (see fig. 4(b)), of about 0.05 Å. This is consistent with polarization occurring mainly by movement of charges along the quasi-2D inter-layer space, perpendicular to the stacking direction, for example by movement of ions out of preferred sites on inter-layer surfaces. We believe that the intercalated cations and possibly water molecules dominate the interfacial polarization process for smectite particles, which explains the low critical field and fast response observed for the smectite suspensions as compared to the kaolinite suspensions.

Considering that the induced dipole is structurally forced to remain in the plane of the silica sheets, we can explain why the particles rotate under application of the field, and we can further describe the distribution of particle orientations around the mean orientation in terms of a competition between i) the homogenizing entropy and ii) the aligning effect of the strong external electric field. Indeed, the Gibbs energy of the colloid population can be written as the sum of an entropic term and of the interaction energy of the clay particles with a local mean electric field aligned with the external field. These two terms are dependent on the functional form of the orientation distribution probability (ODP) function, f, of the particles. Minimizing the Gibbs energy with respect to that functional form yields the orientation distribution at equilibrium. This calculation is presented in detail in a separate manuscript [29]; it follows the line of the well-known theory developed by Maier and Saupe to describe a different geometry, namely nematic ordering [30, 31]. In our system, the interaction energy is different from that of Maier and Saupe, but the final functional form obtained for f is identical: $f(\alpha) \propto \exp[m \cos^2 \alpha]$, where the angle α denotes the deviation from the mean orientation, while the physical parameters characteristic of the system are contained in the expression of the parameter m [29]. Obviously, the expression for m is different in our system from what it is

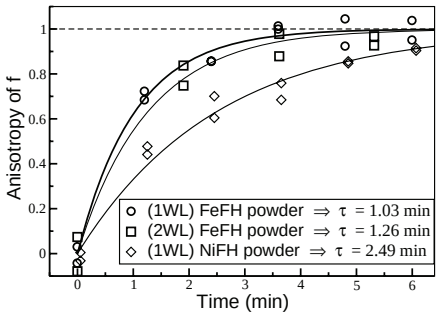

Fig. 5 – Anisotropy of the ODP function as a function of time during the buildup of the electrorheological structure. The anisotropy is computed as the amplitude of the oscillations in fig. 4(a), normalized by its asymptotic value at large times. The characteristic time τ is obtained by fitting an exponential profile to the data.

in the Maier-Saupe theory. For each type of clay in fig. 4, we have fitted the proper profiles to the data in order to infer the Maier-Saupe ODP function f of the particles within the bundles (see [32] for a detailled description of the method). The RMS values for the half width of f are: $25.1 \pm 0.3°$ for Na-fluorohectorite, $24.7 \pm 0.4°$ for Ni-fluorohectorite, $20 \pm 0.7°$ for Fe-fluorohectorite, and $17.2 \pm 0.06°$ for the natural quick clay, which corresponds to values of the corresponding order parameter, $S = \langle 3 \sin^2 \alpha - 2 \rangle_f$ [29], of 0.53, 0.54, 0.68 (Ni-, Na-, Fe-fluorohectorite, respectively) and 0.76 (natural clay) [29]. This difference in order parameter magnitude may be related to differences in particle size and polydispersity.

What exactly occurs in the between-platelets space under the application of the electric field remains unclear. We have monitored the transient buildup of the orientation distributions (as represented in fig. 4(a)) following the sudden switch-on of the electric field above E_c. Figure 5 shows the amplitude of the azimuthal profiles (such as those shown in fig. 4(a)) as a function of time; the plots have been rescaled so that the amplitude at infinite time be equal to 1. Characteristic time scales τ were obtained from fits in the form $1 - \exp[-t/\tau]$; the time scales obtained are of the same order as or a bit larger than the durations after which no particle movement is visible in the microscope. As shown by fig. 5, those dynamical experiments did resolve clear differences in characteristic time scales for chain ordering depending on the type of intercalated ion; for example, a factor of 2 (faster dynamics) was observed in the buildup velocity for Ni-, as compared to Fe-, fluorohectorite samples. In contrast, when preparing fluorohectorite samples in different hydration states, we were not able to resolve a dependency of the transient dynamics on the number of intercalated water layers, although we cannot exclude the possibility of such effects existing within our experimental uncertainty. Yet, our present data clearly indicates that the role of ions in the polarization process dominates that of water molecules. Understanding the mechanisms underlying the particle polarization shall require experiments utilizing other experimental techniques. An EXAFS study of the vicinity of the intercalated nickel cations during particle polarization, which can show how their spatial configuration inside the interlayer space is modified by the electric field, is planned. Note that for these suspensions, one may be able to control the characteristic time for dipolar chain formation on the macro-scale by manipulating, on the nano-scale, the nature of the intercalated ions as well as the number of intercalated water layers. Among foreseeable applications are the ones common to electrorheological fluids [33]. Another potential application is a method for separating smectite from non-smectite components, in natural clays.

* * *

We gratefully acknowledge assistance from the staff of the Swiss-Norwegian Beam Lines at ESRF. J. JØNLAND generously provided us with the natural clay. This work was supported by the Research Council of Norway (RCN) through the NANOMAT Program: RCN project numbers 152426/431, 154059/420 and 148865/432, as well as 138368/V30 and SUP154059/420.

REFERENCES

[1] GAST A. P. and ZUKOSKI C. F., *Adv. Colloid Interface Sci.*, **30** (1989) 153.
[2] HILL J. C. and VAN STEENKISTE T. H., *J. Appl. Phys.*, **70** (1991) 1207.
[3] HALSEY T. C., *Science*, **258** (1992) 761.
[4] HALSEY T. C. and MARTIN J. E., *Sci. Am.*, **269** (1993) 58.
[5] WEN W. D., ZHENG W. and TU K. N., *J. Appl. Phys.*, **85** (1999) 530.
[6] WEN W., HUANG X., YANG S., LU K. and SHENG P., *Nature Mater.*, **2** (2003) 727.
[7] SPRECHER A. F., CARLSON J. D. and CONRAD H., *Mater. Sci. Eng.*, **95** (1987) 187.
[8] TAN Z.-J., ZOU X.-W., ZHANG W.-B. and JIN Z.-Z., *Phys. Rev. E*, **59** (1999) 3177.
[9] HAO T., KAWAI A. and IKAZAKI F., *Langmuir*, **14** (1998) 1256.
[10] QI Y. and WEN W., *J. Phys. D*, **35** (2002) 2231.
[11] DÜRRSCHMIDT T. and HOFFMANN H., *Colloid Surf. A*, **156** (1999) 257.
[12] VELDE B., *Introduction to Clay Minerals* (Chapman and Hall, London) 1992.
[13] FOSSUM J. O., *Physica A*, **270** (1999) 1.
[14] MOURCHID A., LECOLIER E., VAN DAMME H. and LEVITZ P., *Langmuir*, **14** (1998) 4718.
[15] BONN D., KELLAY H., TANAKA H., WEGDAM G. and MEUNIER J., *Langmuir*, **15** (1999) 7534.
[16] GABRIEL J.-C. P. *et al.*, *Nature*, **413** (2001) 504.
[17] DIMASI E., FOSSUM J. O., GOG T. and VENKATARAMAN C., *Phys. Rev. E*, **64** (2001) 061704.
[18] LEMAIRE B. J., PANINE P., GABRIEL J.-C. P. and DAVIDSON P., *Europhys. Lett.*, **59** (2002) 55.
[19] FOSSUM J. O., GUDDING E., FONSECA D. M., MÉHEUST Y., DIMASI E., GOG T. and VENTAKARAMAN C., *Energy*, **30** (2005) 873.
[20] COUSSOT P., NGUYEN Q. D., HUYNH H. T. and BONN D., *Phys. Rev. Lett.*, **88** (2002) 175501.
[21] BONN D., TANASE S., ABOU B., TANAKA H. and MEUNIER J., *Phys. Rev. Lett.*, **89** (2002) 015701.
[22] KAVIRATNA P. D., PINNAVAIA T. J. and SCHROEDER P. A., *J. Phys. Chem. Solids*, **57** (1996) 1897.
[23] MOORE D. M. and REYNOLDS R. C. jr, *X-Ray Diffraction and the Identification and Analysis of Clay Minerals*, 2nd edition (Oxford University Press, Oxford) 1997, p. 150.
[24] BRINDLEY G. W. and BROWN G., *Crystal Structure of Clay Minerals and Their X-ray Identification* (Mineralogical Society, London) 1980.
[25] DA SILVA G. J., FOSSUM J. O., DIMASI E. and MÅLØY K. J., *Phys. Rev. B*, **67** (2003) 094114.
[26] WANG B. X. and ZHAO X. P., *J. Mater. Chem.*, **12** (2002) 1865.
[27] DA SILVA G. J., FOSSUM J. O., DIMASI E., MÅLØY K. J. and LUTNÆS S. B., *Phys. Rev. E*, **66** (2002) 011303.
[28] HAO T., *Adv. Colloid Interface Sci.*, **97** (2002) 1.
[29] MÉHEUST Y., PARMAR K. P. S., FOSSUM J. O., KNUDSEN K. D., MÅLØY K. J. and FONSECA D. M., *Orientational distribution of nano-layered clay particles inside electrorheological chains —a Waxs study* (2006), preprint.
[30] MAIER W. and SAUPE A., *Z. Naturforsch. A*, **13** (1958) 564.
[31] MAIER W. and SAUPE A., *Z. Naturforsch. A*, **14** (1959) 882.
[32] MÉHEUST Y., KNUDSEN K. and FOSSUM J. O., *Inferring orientation distributions in anisotropic powders of nano-layered crystallites from a single 2D WAXS image* (2005), preprint submitted to *J. Appl. Cryst.*
[33] GANDHI M. V. and THOMPSON B. S., *Smart Materials and Structures* (Kluwer Academic Publishers, Dordrecht) 1992.